OPTICAL MEASUREMENT TECHNIQUES FOR HIGH-SPEED, LOW-DENSITY FLOWS IN A DETONATION DRIVEN SHOCK TUBE

by

Catriona Margaret Lindsay White

A Thesis

Submitted to the Faculty of Purdue University

In Partial Fulfillment of the Requirements for the degree of

Master of Science in Aeronautics and Astronautics

School of Aeronautics and Astronautics

West Lafayette, Indiana

December 2021

THE PURDUE UNIVERSITY GRADUATE SCHOOL
STATEMENT OF COMMITTEE APPROVAL

Dr. Timothée Pourpoint, Chair
School of Aeronautics and Astronautics

Dr. Robert Lucht
School of Mechanical

Dr. Robert Orth
Consulting Chemistry Expert

Approved by:
Dr. Gregory Blaisdell

For my parents and my brother who supported me throughout my education, and to my friends Tyler, Robb, Asa, and Kyle who helped me along the way

ACKNOWLEDGMENTS

I would like to thank my advisor, Professor Timothée Pourpoint, for all of his assistance and direction throughout the course of my graduate education and graduate research career. I had plenty to learn when I started my master's degree and he very much helped me stay organized and on track with every interesting project that I ended up working with. I would also like to express my gratitude to my other committee members, Dr. Robert Lucht and Dr. Robert Orth, for their help and guidance. Dr. Orth in particular helped me understand the chemistry principles behind my work and was always willing to answer my many questions about spectroscopy, which I am very thankful for. I would additionally like to thank Michael Orth, who initiated this project and did much of the early planning and design work. Early work on this project was sponsored by Dr. Daniel Guildenbecher and Sandia National Laboratories, as well as Dr. Daniel Dorney and Dr. David Dawicke at NASA, who provided funding and insightful comments throughout this project. Thank you to all of my colleagues at Zucrow labs for their friendship and encouragement. In particular I would like to mention Cole Nielson, who aided in the last test campaign. Best of luck to him working with the system. I would also like to thank Rob McGuire for machining a usable system for testing and corrected every issue that came with the engineering drawings associated with this project. Finally, I would like to thank Jason Gabl, who's experience and patience ensured that this project was successfully built and tested. Without Jason this project would not have had nearly as many successful tests.

TABLE OF CONTENTS

LIST OF TABLES

LIST OF FIGURES

NOMENCLATURE

BOS	=	Background Oriented Schlieren
D	=	Tube diameter, inch
d_{PT}	=	Distance between two Kulite pressure transducers
h	=	Schlieren event thickness, inch
HDPE	=	High Density Polyethylene
$G(\lambda)$	=	Gladstone-Dale constant
L	=	Tube length, inch
M	=	Optical magnification
MR	=	Mixture Ratio
MW_{H2}	=	Molecular weight of H2, 2.02 u
MW_{ox}	=	Molecular weight of O2, 32.00 u
n	=	Refractivity index, no unit
n_0	=	Refraction index of undisturbed flow
P_{ox}	=	Pressure of oxygen gas in the shock tube
P_{H2}	=	Pressure of hydrogen gas in the shock tube
ρ	=	Density, lb_m/ft^3
ρ_1	=	Air density, lb_m/ft^3
ρ_2	=	Density of combustion products immediately after leaving shock tube, lb_m/ft^3
ρ_3	=	Density of combustion products following shock wave, lb_m/ft^3
t_{PT1}	=	Time measurement at the first Kulite pressure transducer
t_{PT2}	=	Time measurement at the second Kulite pressure transducer
$U_{variable}$	=	Uncertainty on the subscript variable of interest
V	=	Wave speed in the shock tube
Z_d	=	Distance between background and schlieren event, inch

ABSTRACT

Hypersonic flow conditions, such as temperature, pressure, and flow velocity, are challenging to measure on account of the extreme conditions experienced by a craft moving above Mach 5. At Mach 5, the temperature in stratospheric air behind a normal shock wave exceeds temperatures of 1,300 K, and as the craft speed increases, so does the temperature. At these temperatures and conditions, traditional measurement techniques such as thermocouples and pressure transducers either alter the flow path, affecting the measurement, or they do not survive the external conditions. As such, there is interest in investigating alternative ways to measure flow properties. This thesis focuses on the implementation of several optical measurement techniques designed to determine the flow temperature, density gradient, and flow velocity in a detonation driven shock tube. A detonation driven shock tube was chosen for the project as it reliably creates high-speed, low-density, gas flows that are reminiscent of hypersonic conditions.

The first optical measurement technique implemented was background oriented schlieren, a measurement technique that quantitatively provides density gradient data. Experimental data obtained at pressures up to 3,000 psia resulted in density gradients at the exit of the detonation tube in good agreement with the literature.

The detonation tube was also fitted with two fiber optic ports to gather chemiluminescence thermometry data. Both a Stellarnet Black-Comet spectrometer and a Sydor Ross 2000 streak camera were used to capture spectroscopic data at these ports, in order to determine the detonation speed and the rotational temperature of the intermediate OH* combustion products. The Stellarnet spectrometer did not have a fast enough data capture rate to gather reliable data. While the streak camera captured data quickly, we had difficulty gathering enough light from the combustion event and the gathered data was very noisy. The streak camera did however capture the time duration of the full combustion event, so if the fiber connector ports are improved this data taking method could be used in the future to gather rotational temperature data. Both measurement techniques provided some unintrusive measurements of high-speed flows, and improvements to the data taking system could provide much needed information on hypersonic flow conditions.

1. INTRODUCTION

We need to understand high speed flow characteristics to develop aerospace propulsion systems. Almost all spacecrafts, aircrafts, and rockets use chemical propulsion, which generates thrust through a chemical reaction by combining an oxidizer and a fuel and igniting the mixture. Combustion events generate hot gaseous exhaust products, which upon expanding create thrust and propel the system forward to achieve flight. Exhaust gases exit propulsion systems at high temperatures and high velocities, which need to be considered when designing any propulsion system.

Similarly harsh flow conditions can exist outside of the combustion chamber of a propulsion system. Hypersonic aircraft can reach speeds nearing Mach 10 – ten times the speed of sound – while re-entry spacecraft can be moving at speeds nearing Mach 25. At Mach 5, the temperature of stratospheric air behind a normal shock wave exceeds 1,300 K. Temperatures at the leading ends of air and spacecraft moving at these speeds increase even further at higher Mach numbers. At this temperature, the air ionizes and turns into plasma surrounding the vehicle. Because of these extreme conditions, the external temperature and gas velocity need to be known to make a robust vehicle design so the craft can function as expected and the components encouraging these flows do not fail.

The purpose of this thesis is to explore novel measurement techniques to determine the temperature and velocity of high speed, high temperature gas flows. These characteristics determine the materials the craft can be made from, the ideal speed the craft should travel at, and for reentry vehicles, the ideal angle of entry in order to best make use of the air braking to slow the craft down. Understanding these parameters is paramount in air and spacecraft design, and there is interest across the entire aerospace industry to employ the best analysis methods.

There are several existing methods that are often used to measure the velocity and temperatures of high-speed, low-density gas flows, such as those produced by detonation events. The primary method that is used to measure the temperature of a detonation event is to place a thin thermocouple probe directly into the flow path. Thermocouples provide the temperature of the gas in a flow when the gases contact the tip of the thermocouple probe. However, placing probes directly into the flow path to measure the temperature disrupts the flow path further down. Flow disruptions can cause issues with measurements from any thermocouples downstream in the

system, and the intrusive nature of a thermocouple complicates measurements of realistic flow path characteristics. Additionally, any tests using a thermocouple are limited by the time resolution of the thermal mass of the thermocouple probe. While this does not pose a problem for steady state systems, the high-temperature, high-speed systems of interest in this thesis exceed these limits, making it very difficult to gather accurate data using a thermocouple. Finally, as thermocouples are inserted directly into the flow path, they have to endure the issues associated with the propellants, which can be problematic at very high temperatures or if the propellants of interest are highly corrosive. Because of all these issues, non-intrusive techniques to collect temperature data are of great interest.

Similarly, velocity measurements of high-speed flows are often completed by monitoring the pressure wave with two pressure transducers that are spaced a known distance apart. Pressure transducers produce accurate results; however, the results are often limited by the data recording rate of the pressure transducers. In addition, the method can have high uncertainty as it is nearly impossible to pinpoint exactly when the pressure wave passes through the system. Due to the uncertainty, pressure transducers with low recording rates will almost never give detailed velocity reports. Pressure transducers with high recording rates can give a better estimate of the flow speed, but these types of pressure transducers are expensive and often fragile, which means that these transducers must be replaced in between each test in harsh testing environments. An objective of this thesis is to investigate the use of chemiluminescence thermometry in order to record the temperatures and velocities of flows immediately before, during, and after detonation events.

High-speed gas phase flows were created repeatably and reliably through use of a detonation driven shock tube. Detonation driven shock tubes have long been used to mimic blast simulations for laboratory studies as they are relatively simple in design. The detonation tube used in the present study uses oxygen gas and hydrogen gas in a high-pressure tube. Once mixed, the detonation gases are ignited using a simple car spark plug. The design proved reliable in creating flows of interest, and easily adaptable in order to contain fiber optic ports for chemiluminescence data measurements.

Previous work done at Purdue University has shown that it is possible to measure the rotational temperature of the intermediate combustion products by recording their spontaneous emission spectra. A streak camera captures the emission spectra of various intermediate combustion products over short time durations. The emission spectra are related to the relative

spatial temperature profiles of the combustion products to calculate the rotational temperature. Ultimately, by knowing the rotational temperature and the combustion products created in the detonation event, the equilibrium temperature can be calculated without placing a thermocouple directly into the flow path.

The secondary goal of the present study was the measure the velocity of the combustion event based on the streak camera data. As the streak camera captures the emission spectra relative to time, and the angle of the view for the fiber optic cable is known, the velocity of the combustion even could be calculated as the distance the products travel over the time recorded by the streak camera.

Another measurement technique briefly investigated during the early project phases was background oriented schlieren imaging. Background oriented schlieren uses a high-speed camera to record the changes of density in the flow path by comparing the gases against a dot pattern background. The camera system was fully integrated for the low-pressure test campaign and was phased out for higher pressures due to some concern over the integrity of the dot pattern background. The dot pattern used in this testing was printed on paper and attached to a plexiglass sheet with duct tape. The plexiglass is bolted down. At high pressures, the dot pattern paper would rip during the detonation event, changing the background and making it impossible to compare the flow conditions to the original background. Without generating usable data, we chose not to continue pursing data collection using background oriented schlieren.

In the following chapters, we will review the fundamentals of the background oriented schlieren density measurement technique, followed by the essentials of optical emission spectroscopy and the inner workings of a streak camera, and finally the detonation tube and optical connection port design. We will then review the three test campaigns supporting this thesis: a low-pressure test campaign, a preliminary high pressure test campaign, and a second high pressure test campaign. The low-pressure test campaign collected density data with background oriented schlieren. The initial high pressure test campaign collected velocity data with two high speed Kulite pressure transducers. The final high-pressure test campaign integrated the streak camera into the full system to gather intermediate combustion product data. All three test campaigns will be discussed in this thesis, along with lessons learned and further applications.

2. LITERATURE REVIEW

In order to implement the measurement techniques of interest, we completed a literature review of background oriented schlieren, optical emission spectroscopy, and streak cameras. Background oriented schlieren involves a complicated post processing code that requires good understanding of the theory behind the system in order to calculate accurate density gradients. Optical emission spectroscopy captures the intensities of various intermediate combustion products at known wavelengths to determine how prominent the products of interest are in a system. Streak cameras, coupled with optical emission spectroscopy systems, capture optical data over a known time duration to further understand the system and the prominence of the intermediate combustion products of interest. All of these techniques and the associated theories will be reviewed here.

2.1 Background Oriented Schlieren

Background oriented schlieren (BOS) is a technique used to quantify density fields in hot gases. BOS is a measurement technique similar to traditional 'knife edge' schlieren imaging, which has been used for more than a century to capture images of density gradients within fluid flows. For traditional schlieren, collimated light is focused through a lens and onto a knife-edge. The knife-edge is placed at the focal point with the intention of blocking part of the light from reaching the point of interest. A camera is aligned with the point of view in order to record variations in the densities of the fluids. When fluids of varying densities enter the field of view, the image distorts, and due to the knife edge blocking half of the light, parts of the image get lighter as the density of the gases of interest are higher than the surrounding gases, or darker if the densities are lower. Schlieren imaging highlights the density field and gives good insight to the flow behaviors.

Background oriented schlieren uses far fewer optics, making the system much easier to assemble. BOS also provides qualitative and quantitative measurements of the density gradients, while traditional schlieren imaging only provides qualitative information. Because of these advantages, there has been a growing interest in using background oriented schlieren over the past two decades, although due to the relatively complicated post-processing required, BOS is not a commonly used technique.

The principle behind background oriented schlieren is simple: when a camera looks through hot gases that have different densities compared to the cold surrounding gases, the air behind the gases distorts. The distortion can be analyzed. Humans can even see this phenomenon when looking at a sidewalk on a hot day, when one might observe wavy heat lines rising from the sidewalk. 'Heat haze' is visible when the gases near the hot sidewalk heat up, lowering the density and causing the gas to rise, ultimately creating the familiar wavy pattern in the surrounding cooler air. The goal of BOS is to take a picture of the 'heat haze' in controlled situations, in order to determine how the density of the gases of interest differ from the surrounding air.

Meier (1999) and Richard et al. (2000) showed that BOS data can be captured using a camera, a background dot pattern, and a light source. The setup captures pictures or videos of the distortions on the dot pattern, which are a direct result in changes in density in the gases between the camera and the background. A simplified image of a common BOS system is shown in Figure 2.1.

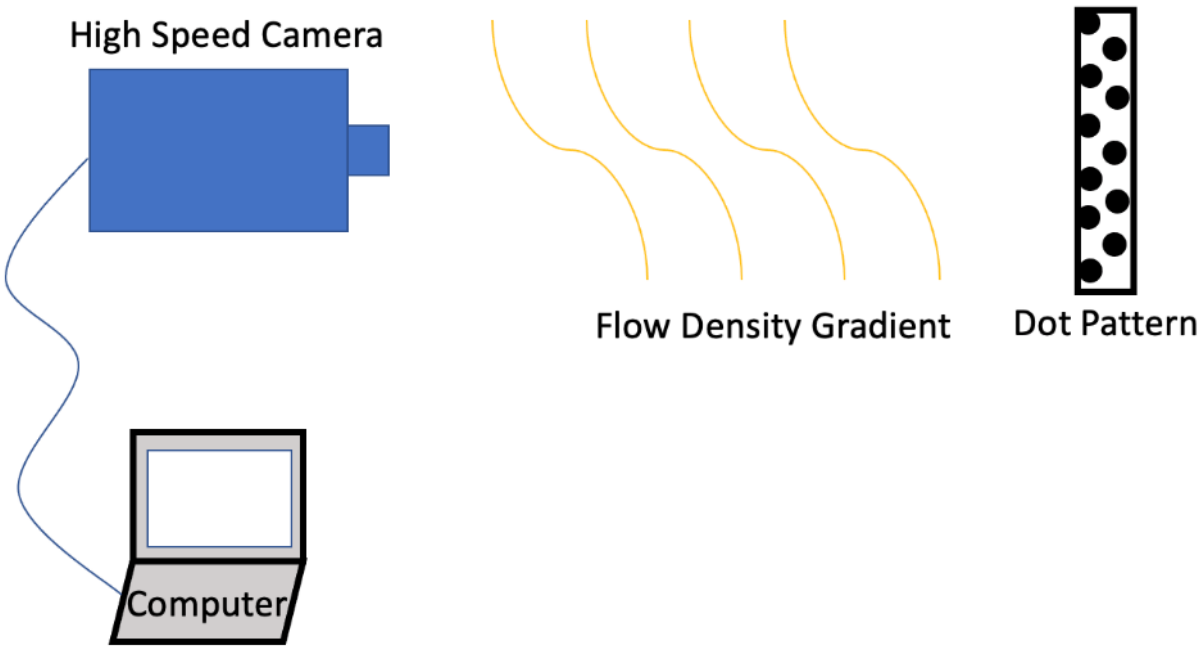

Figure 2.1: Simple Background Oriented Schlieren Setup

The difficulty in applying the BOS technique is in the photograph analysis. In general, post-processing requires significant computing power. While traditional schlieren gives qualitative results almost immediately, BOS requires a full image processing code to record the variation between the background and test dot pattern. I developed an in-house MATLAB code for BOS analysis, although similar codes exist in python and other programming languages. My code takes in two images: one of the undisturbed background dot patterns, and one of the dot patterns during a high-speed detonation event. The code records the change in the background by converting the images into matrices and cross-correlating the resulting matrices. The code records the image change between the original image and the high-density image. From there, the image change is quantified using the Gladstone-Dale relation shown in Equation 1. The Gladstone-Dale relation, along with the full math associated with a quantitative background oriented schlieren codes, are presented in Sommersel et al., 2008.

$$G(\lambda) = \frac{n-1}{\rho} \tag{1}$$

The constant $G(\lambda)$ is the Gladstone-Dale constant, which is determined by the frequency of light used in taking the images and the gaseous media the image is taken through. The refraction index, n, is determined by the fluid medium between the background and the camera. Equation 2 is used to calculate the refraction index. Finally, ρ, is the density gradient of the gas, which is the final variable of interest. The main purpose of the MATLAB code is to solve for n with the purpose of calculating the density gradient.

$$\frac{d^2n}{dx^2} + \frac{d^2n}{dy^2} = \frac{n_0}{M * Z_d * h} * \left(\frac{d\Delta x}{dx} + \frac{d\Delta y}{dy}\right) \tag{2}$$

The majority of the terms are constants. n_0 is the refraction index of the undisturbed flow – which was the refraction index of air before the tests. M is the optical magnification, which was calculated based on which camera was used during testing. Finally, both Z_d and h are distances that are determined by the experimental setup. Z_d represent the distance between the background and the flow of interest, while h is the thickness of the flow. The Δx and Δy terms as unknowns,

so the purpose of the post-processing code is to determine how much the flow distorts the dot pattern in the x and y direction in order to solve the right-hand side of Equation 2.

An example of an expected BOS displacement result, represented by the color bar in Figure 2.2, was taken by Utkarsh Pandey during some early air column testing. For Figure 2.2, an air column impacted a stable spike. It was suspected that the air column was not impacting the cone at the dead center, resulting in an uneven gradient on each side of the cone. Figure 2.2 only shows the calculated distortion of each cell against the dot background. Which while that value is not the actual density, the distortion is a required variable to solve for the density, and the total displacement between the schlieren event and the dot background indicates the total density trend.

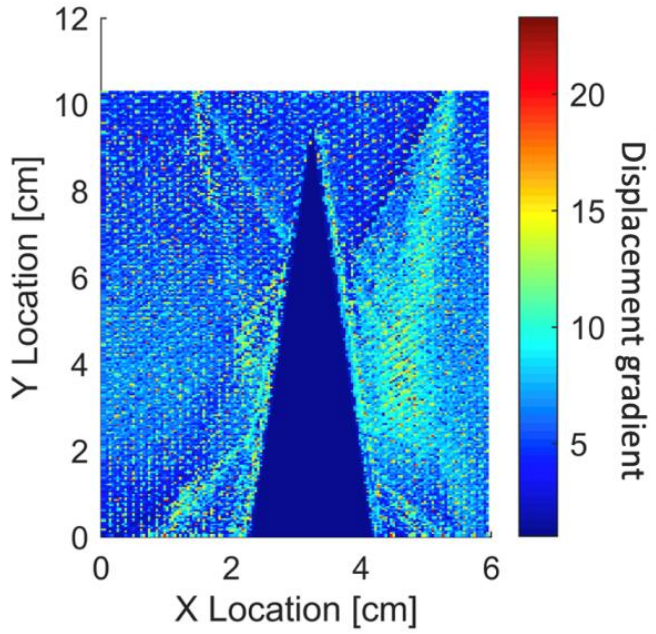

Figure 2.2: A standard Background Oriented Schlieren image

Figure 2.2 primarily provided the density gradient in the steady-state air around the cone. We wanted to apply the same principle to an unsteady detonation event. The background oriented schlieren code that was used to generate Figure 2.2 was also used throughout the remainder of the test campaign. Most of the background oriented schlieren data collected during our experiment was taken during the early, low pressure testing campaign. The results will be discussed in detail later in this document.

2.2 Optical Emission Spectroscopy

We used optical emission spectroscopy (OES) to measure the chemiluminescence of the excited state radicals that exist in both flames and detonation events. OES is a path-average, non-intrusive measurement technique. To gather OES data, a streak camera is coupled with a combination ultraviolet and visible light (UV/Vis) spectrometer in a configuration that captures the intensities of the optical emission spectra that OES uses. This thesis will first review OES as a measurement technique, and what specific spectroscopic wavelengths were required for the setup, followed by a description of how a streak camera works to illustrate how the system can be used for optical emission spectroscopy and chemiluminescence thermometry.

2.2.1 Optical Emission Spectroscopy

Optical emission spectroscopy measures the excited state of radicals that are produced at high temperature and during combustion events. OES does this by recording the wavelengths of the photons that are emitted by the molecules within the combustion event of interest. Photons are produced when an atom moves from a higher energy, excited state to a low energy state, which emits the light and specific wavelengths that a spectrometer captures. Specific molecules and radicals – such as O_2, OH*, etc. – produce characteristic wavelengths. The characteristic wavelengths can be matched to their corresponding elements – such as boron, sodium, potassium, etc. – in order to determine which elements are present, or to determine if certain intermediate combustion products are present.

As the detonation tube uses gaseous hydrogen and oxygen as propellants, we were looking for the spectroscopic peaks of OH*. OH is one of the most prominent intermediate combustion products of the hydrogen-oxygen reaction. The combustion product is often in literature denoted as OH* to indicate that the radicals are in an excited state. The presence of OH* indicates that burned products exist in the analysis region, and based on the intensities, can be used to extract the rotation temperature of the excited state of the molecule.

Traditionally, rotational temperature does not directly relate to translational temperature, because the presence of excited state radicals is dependent on both the flame composition and on the translational temperature. In general, excited state radicals can be produced in two ways, as explained by Fiala and Sattelmayer (2013): by an exothermic chemical reaction, or by thermal

excitation. As explained by Orth et al. (2018), additional issues with OES can be caused by the vibrational temperature not being in equilibrium with either the translational or rotational temperatures at higher electron states, and interfering species being recorded during the measurement. While these issues can lead to uncertainties in the measurements, they can be controlled by designing experiments to only include species of interest, as a means to minimize contamination of the intermediate combustion products. By limiting the contaminant products, the rotational bands of interest can be identified with greater certainty, while minimizing the interference effects caused by unexpected combustion products during the time-averaging of a spectral plot.

2.2.2 Fundamentals of Streak Cameras

As described by the Hammamatsu streak camera manual [15], a streak camera is used to measure the intensity, time, and position of a system of interest over extremely short time periods. A streak camera does this by collecting high speed optical data, or light, with high temporal resolution and analyzing the data it received internally. When a streak camera is coupled with a spectrometer, it can instead measure intensity, time, and wavelength, which is what optical emission spectroscopy requires. A typical setup to describe how a streak camera turns light into intensity, time, and wavelength data is shown in Figure 2.3.

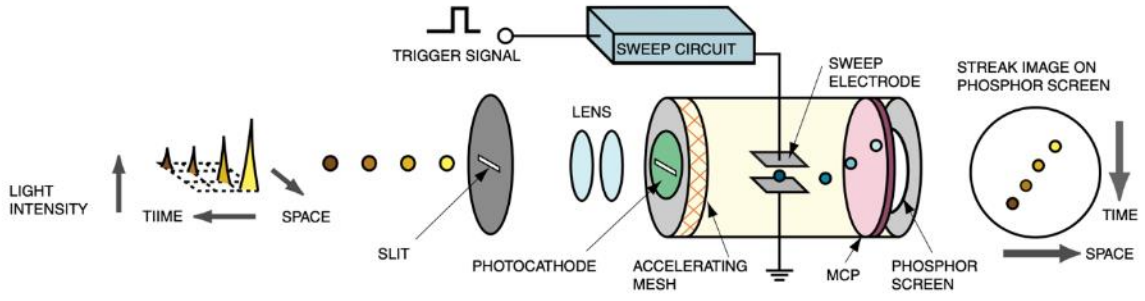

Figure 2.3: Breakdown of the Inner Workings of a Common Streak Camera (Hamamatsu 2008)

First, light enters the system through a small slit. Immediately after the light enters the slit, it is converted into photoelectrons by the photocathode that resides in the streak tube. The number of electrons produced during this process is proportional to the intensity of the light that entered

the slit. The electrons are then accelerated, and the trigger signal is sent to the sweep circuit so that high voltage is applied to the sweep electrodes. The purpose of the sweep circuit is to deflect the electrons that arrive at slightly different times to slightly different angles. Deflection is only done in the vertical direction, which allows the streak camera to track the arrival time of the light electrons and create the time axis. The electrons then enter the micro-channel plate (MCP), which greatly accelerates the electrons, so they bombard the phosphor screen at high speeds. The phosphor screen then converts the electrons back into light, which is finally recorded by a CCD camera.

The phosphor image produced when the electrons hit the phosphor plate is designed in such a way that the earliest electrons to arrive are located at the top of the final image, while the final electrons to arrive are located at the bottom of the image, which is the time axis on the final image. Similarly, the horizontal axis in the final phosphor image relates to the location (or the wavelength if the streak camera is coupled with a spectrometer) that the electrons corresponded to when the electrons hit the phosphor screen. Finally, the streak camera outputs a two-dimensional image comparing the time a light particle arrived to the light particle's location (or the light's wavelength in the experimental setup). As the system also tracks the intensity of the light, the final output is a three-dimensional plot with time on the vertical axis, wavelength on the horizontal axis, and the intensity or 'brightness' at that location of the time and wavelength axis. An example of streak camera data taken during an ignition test using nitrogen tetroxide and monomethyl hydrazine. The image of a successful MMH and NTO impinging jet test, taken by Ariel Black and presented in her thesis at Purdue University in 2017, along with the corresponding streak camera read out is given in Figure 2.4. In Figure 2.4, the spectrometer (coupled with the streak camera), took data in the location of the red box of the apparatus image.

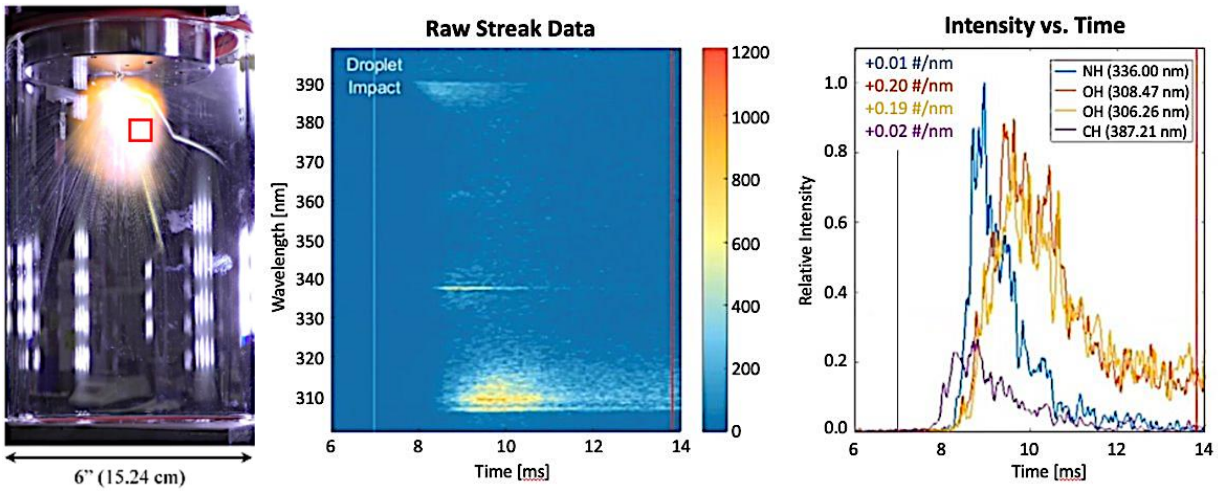

Figure 2.4: Example Streak Camera Data for an Instantaneous Impinging Jet Test

The above image tracks several different intermediate combustion products. The raw streak camera image is shown in the middle of Figure 2.4, and each of the horizontal bright yellow lines corresponds to a different intermediate combustion product at the corresponding wavelength. From there, the intensities of those combustion products can be compared as a function of time. Based on the data on Figure 2.4, there is a significant amount of OH*, which has rotational bands at 306 nanometers, and 308 nanometers. At 336 nanometers, there is a bright but short-lived NH* emission, and finally there is a very dim CH* emission at 387 nanometers.

3. METHODS

We designed a detonation driven shock tube to investigate the applicability of a range of diagnostic techniques to low-density, high-speed, gas-phase flows. The detonation driven shock tube has tunable test chamber conditions and can be run at various mixture ratios, MR. A key outcome of the design effort was to create a system capable of producing reliable and repeatable detonation events. First the methods section will go over shock tube design, followed by the plumbing and instrumentation diagram, and finally will detail the basic operation procedures used during the test campaigns.

3.1 Shock Tube Design

In order to gather the chemiluminescence thermometry data of interest, we needed a repeatable and reliable system to create detonation events. The system also needed to have an attachment space for a fiber optic probe so that it could relay the detonation data to the streak camera and spectrometer. We decided that the best way to meet these criteria was to design and build a detonation driven shock tube. Detonation driven shock tubes generate low-density, high-speed, gas phase flows through relatively simple methods: by filling a closed tube with an oxidizer and a fuel and igniting that mixture. The mixture combusts and creates a shock wave, which bursts a burst disk at the opposite end of the detonation tube from the ignition point. The hot combustion gases exit the shock tube at a high velocity. Due to the simplicity of the system, both the chamber pressures and mixture ratios could be easily altered in order to compare the effects of these parameters on the results of interest.

Detonation driven shock tubes have been widely used to model blast situations. In order to operate a detonation driven shock tube, the tube is filled with a gaseous oxidizer and a gaseous fuel. The sizing of a shock tube is important depending on which oxidizer and fuel are of interest. For large hydrocarbon fuels a larger volume is needed to assure proper mixing between the fuel and oxidizer, and in order to provide sufficient room for the larger sized cells of the detonation wave to pass by. As the goal of this project was to look at simple intermediate combustion products, we designed the detonation tube for use with gaseous oxygen and gaseous hydrogen in order to try and capture spectroscopic data on the OH* molecule.

Although we only tested hydrogen during this test campaign, the detonation tube is also sized appropriately for use with smaller carbon fuels such as ethylene and acetylene to monitor the CH* molecule. Oxygen and hydrogen reactions are ideal for chemiluminescence thermometry because oxygen and hydrogen combustion produce a high flame temperature. The combustion process and final flame temperatures of oxygen and hydrogen reactions are also well studied and understood, so we could validate any findings with the well-known and established trends.

In order to get accurate measurements of only the combustion products, the shock tube needs to be drawn down to vacuum pressure, typically around 1 psia, before any oxygen or hydrogen enter the system. Drawing the shock tube down to vacuum limits the amount of nitrogen or air contamination in the system and allows for a more accurate estimation of mixture ratio. The mixture ratio is set by pressure filling in both oxygen and hydrogen to the desired pressures, and by knowing the molecular weights of the propellants. The calculation for this process is shown in Equation 3. The fuel and oxidizer enter the shock tube opposite each other in order to force mixing and have more complete combustion. In Equation 3, P_{ox} is the oxygen fill pressure, P_{H2} is the hydrogen fill pressure, MW_{ox} is the molecular weight of O_2, and MW_{H2} is the molecular weight of H_2.

$$MR = \frac{P_{ox} * MW_{ox}}{P_{H2} * MW_{H2}} \tag{3}$$

The shock tube itself is made of a 1.5-inch diameter stainless-steel pipe with a 0.6-inch diameter exit. Thick walls are necessary to withstand high-pressure combustion events. As an oxygen-hydrogen reaction can produce pressure spikes beyond 10,000 psi with only 300 psi of filling pressure, having a thick-walled system was required in order to ensure that the pressure wave successfully proceeded all the way downstream without causing any damage.

The longest section of the shock tube is 16.25 inches in length and 0.6 inches in diameter. It contains optical ports at 10.25 inches, HF-PT-01 in Figure 3.1and 3.2, and 14.25 inches, HF-PT-02 in Figure 3.1 and 3.2, down the shock tube, relative to the ignition point. At the end of the shock tube is a ConFlat (CF) vacuum flange, which a burst disk is affixed to. The burst disks are designed to fail at high pressures in order to release the pressure waves immediately after a detonation, while still holding back the desired chamber pressure and vacuum pressure. The full shock tube length allows for the pressure within the shock tube to build as the high temperature combustion products

travel down the tube and allows for the shock wave to fully develop before it ruptures the burst disk, in order to get accurate emission spectra measurements.

The burst disk is crushed between two CF flanges. For low pressure cases, the plastic burst disk is crushed between the CF flange on the main shock tube and a second CF flange that is not connected to anything else. For high pressure cases, a smaller, secondary extension tube is used. The extension tube is required because the burst disk we use for higher pressure cases is made of metal and produces a higher risk of creating dangerous shrapnel that needs to be directed out of the test cell. The extension tube has a CF flange that connects directly to the main shock tube on one end, one additional optical port down the length of the extension tube, and an opening to the air at the exit. With the extension tube, the total length of the shock tube increases to 23.25 inches. The optical port on the extension tube is 17.25 inches from the ignition point. While the CF flanges are traditionally used to hold vacuum pressure, they were hydrostatically tested up to 4,000 psia, which was enough to hold our required pressures during testing.

Initially the detonation tube was tested at low driving pressures to determine whether the system was functional, and to test the effectiveness of the pressure transducers and background oriented schlieren system. Figure 3.1 below shows the low-pressure detonation tube system, the relative size of all the parts. Figure 3.1 also shows the relative location of the BOS background and camera used in the data analysis process. The low-pressure system does not use the extension tube because we were not worried about shrapnel.

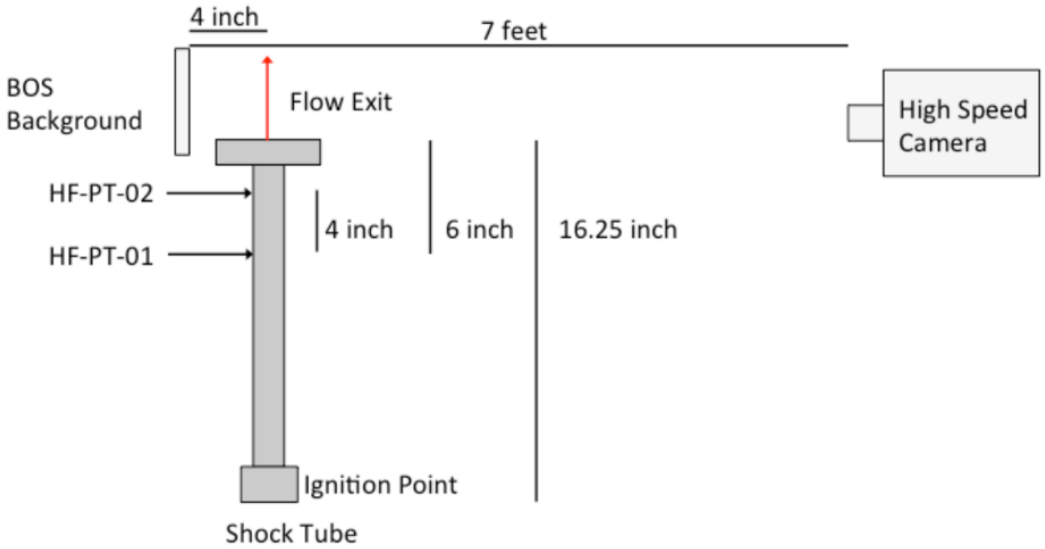

Figure 3.1: Low pressure shock tube integrated with the background oriented schlieren setup

Secondary testing with the streak camera was conducted at high pressures. High pressure tests required the extension tube to fully direct any burst disk shrapnel outside of the test cell. While there were never any personnel in the test cell during detonation testing, the extension tube fully directed any parts of the burst disk that dethatched during testing out of the cell to minimize the risk to equipment. Figure 3.2 shows the full high-pressure test system.

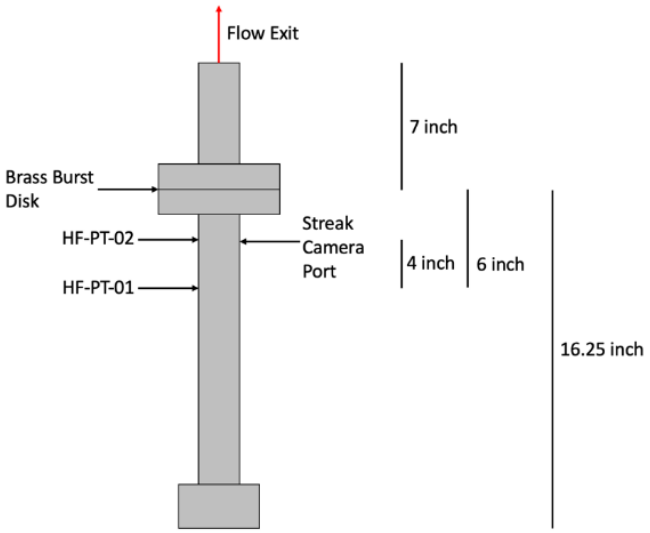

Figure 3.2: High pressure shock tube configuration integrated with streak camera

Plastic burst disks made of moisture resistant HDPE film, were used for early aspects of the test campaign, and had a maximum burst pressure of 120 psia. That meant that any tests using the HDPE film burst disks could not have a chamber pressure exceeding 120 psia before the burst disks would fail. We calculated the burst pressure by slowly filling the detonation tube with nitrogen until the HDPE burst disk ruptured. To accommodate for the burst pressure, we only used the plastic burst disk for chamber pressures less than 100 psia to stay well below the burst pressure. The metal burst disks had a much higher static burst pressure of approximately 3,000 psia. These burst disks were designed and tested by Tranter, Brezinsky, and Fulle in 2001 for similar high pressure shock tube experiments [4]. The burst disks are made of 0.032-inch-thick, soft brass, and had two centered, perpendicular score marks that were 0.010 inches deep. Tranter et al. recommended scoring the burst disks to that depth to minimize the shrapnel the burst disks produced. With the scoring, the burst disks have an estimated burst pressure of 3,000 psia. The high burst pressure allows for the brass burst disk to hold up to 500 psia of chamber pressure and

not rupture until the detonation wave hits the disk. Figure 3.3 shows the burst disks side by side. The HDPE film burst disks needed to be secured to the CF flanges with bolts as they were prone to slipping out of the flange during assembly. The brass burst disks clamped did not have the same issue and were held between the copper gasket and the knife edge without issue.

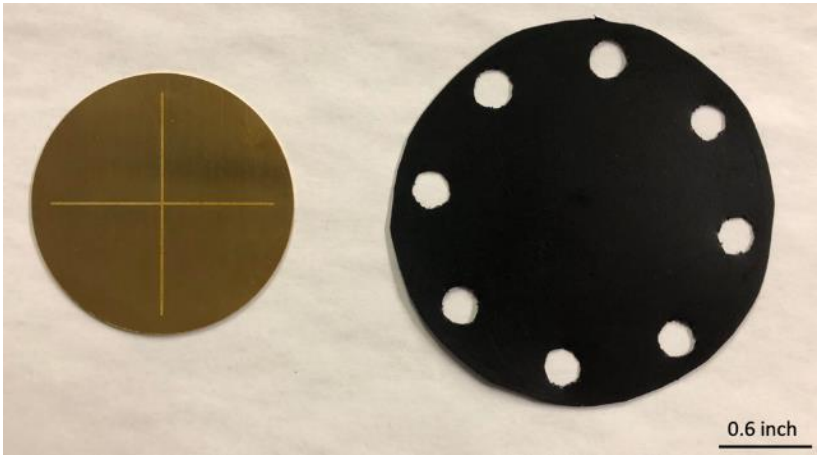

Figure 3.3: Plastic and metallic burst disks used for the low- and high-pressure shock tube tests respectively

Both burst disks were held in place between two CF flanges, illustrated in Figure 3.4. CF flanges contain a knife-edge in the middle of the flange, which cuts into the copper gaskets sold with these flanges. Both the metal and plastic burst disks were aligned with the copper gasket in order to functionally seal the shock tube using the burst disks. The main shock tube was hydrostatically checked and was found to hold up to 4,000 psia leak pressure. As the maximum expected chamber pressure of these tests was 500 psia, the 4,000-psi leak rate was deemed acceptable for testing purposes.

Figure 3.4: Knife-edge CF flanges used for sealing pressure in the shock tube

In order to determine when the shock wave passes the optical ports, there are two high frequency Kulite HEM-375-20000A pressure transducers 4 inches apart on the detonation tube. The Kulite pressure transducers were placed across from the optical ports on the shock tube. These pressure transducers can capture up to two million pressure data points per second and were used to record the relative speed and maximum detonation pressures reached during each shock tube test. Once the timing of the detonation waves relative to the chamber pressure and mixture ratios was known, the chemiluminescence thermometry data collection methods could be implemented.

The optical probes used in this study were designed so that a fiber optic cable could be connected to the shock tube system. By developing special connecting ports that convert a $3/8^{th}$ inch high-pressure company (HiP) line to a fiber optic cable, the streak camera can capture optical data within the shock tube while the main fiber optic cables are still protected. The probe contains a fiber optic cable on one end, which ran the length of the probe, to a connector that sees the detonation gases. The probe is protected by a thick metallized sapphire window, brazed to the stainless-steel shell that houses the probe. The stainless-steel housing was machined to connect to the same high-pressure fittings that the rest of the detonation tube uses. Figure 3.5 shows these probes. Additionally, there are two ports on the shock tube to capture the properties of the detonation at multiple locations.

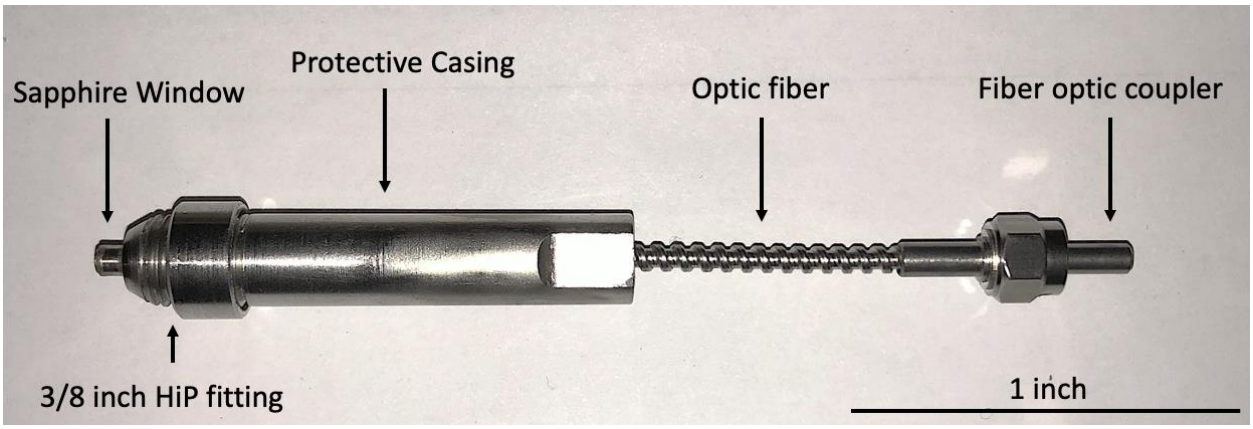

Figure 3.5: Fiber optic to HiP fitting probe

The fiber optic probe was designed to be robust due to the conditions it was expected to see. As such, the fiber probe connected the interior optical fiber directly up to the sapphire window without a lens that would have been more fragile. We determined during design that while the lack of a lens would reduce the amount of light that passed from the probe to the spectrometer, the light loss should be acceptable. A full schematic of the machined fiber is included in figure 3.6.

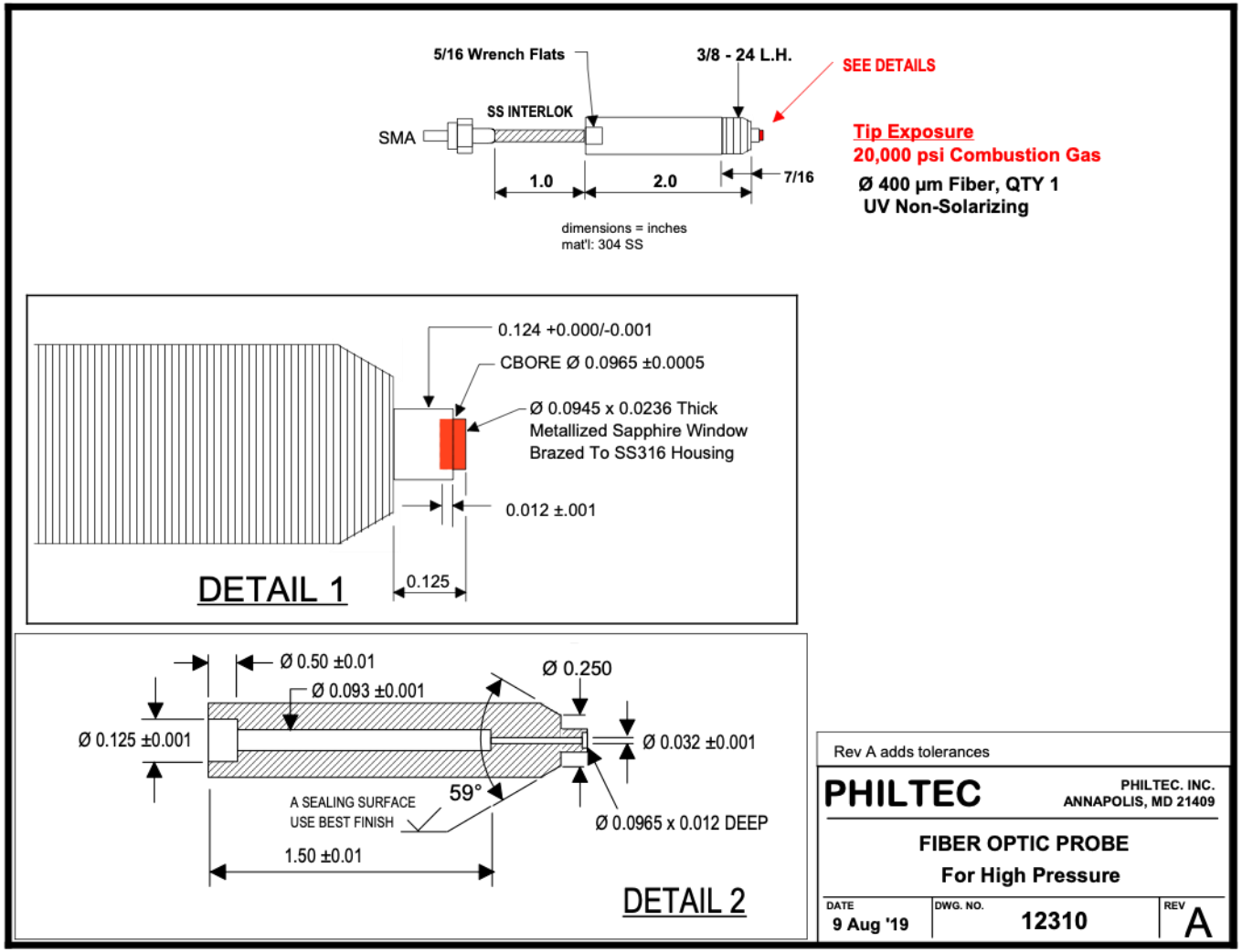

Figure 3.6: Detailed schematic of fiber optic probe to HiP fitting

Early testing used a StellarNet Black-Comet SR spectrometer to collect emission spectra data on the detonation waves. The Black-Comet spectrometer, shown in Figure 3.7, records up to 128 consecutive spectra over integration times between 1 millisecond and 30 milliseconds. Additionally, the spectrometer captures emissions between 220-1100 nanometer wavelengths. While the detonation wave itself occurs on the microsecond scale, the Black-Comet can be used to capture one or two data points during each test. The Black-Comet spectrometer was also used to show that the shock tube design was suitable to record emission spectra data on the OH* intermediate combustion product at the 308-nanometer wavelength.

Figure 3.7: Black comet spectrometer used for early optical emission spectra data collection

Once the system was validated the Sydor model ROSS 2000 streak camera was connected to the shock tube system. The ROSS 2000 has a sweep speed ranging from 30 milliseconds to 300 nanoseconds and can provide a time resolution as low as 7.4 picoseconds, and a spectral resolution up to 0.1 nanometers depending on the grating used and the slit setting of the spectrometer. The ROSS 2000 streak camera is coupled with a spectrometer in order to gather spectral data on OH*. Figure 3.8 shows both the spectrometer and the Sydor streak camera.

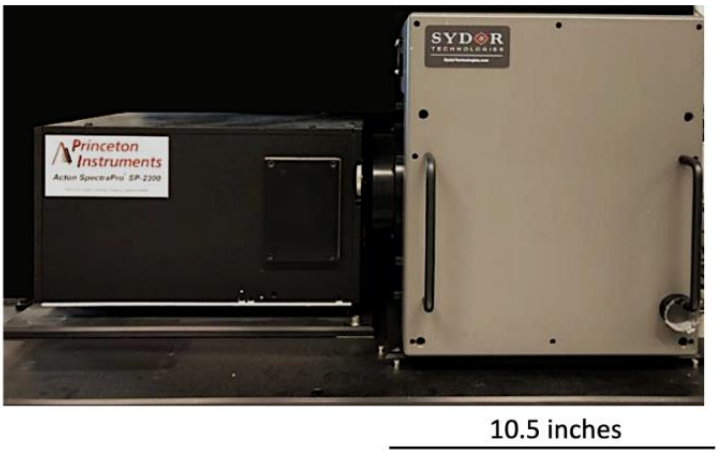

Figure 3.8: Spectrometer and Sydor streak camera used for high-speed optical emission spectra data gathering

3.2 Plumbing and Instrumentation

The shock tube feed system is comprised of two regulators, two manual valves, seven pneumatic valves, five check valves, and a vacuum venturi. These are summarized in the plumbing and instrumentation diagram shown in Figure 3.9. The oxidizer side of the system is bottle fed by a tank mounted manual pressure regulating valve connected to the oxygen bottle. The fuel side of the system is fed by the bulk hydrogen system at Zucrow labs. Both the fuel and oxidizer buffer tanks have a manual shut off valve between the feed systems and the buffer tanks, in order to fully isolate the system from the propellants when it is not in use. The buffer tanks on both sides are connected to a Westlock falcon solenoid valve, which is used to isolate both buffer tanks from the rest of the experiment once the oxidizer and the fuel mix. Beyond the valve, all of the tubes and fittings were made by the high-pressure company (HiP) so that all of the tubes and fittings downstream of the solenoid valve were rated to 20,000 psi. While it was highly unlikely that any of the lines would see a pressure spike that high, the high-pressure lines were used as a precaution, so the system was secure in case there was a problem during one of the test campaigns. Finally, before reaching the shock tube, both the oxidizer and fuel sides have a HiP soft seat check valve, which is also rated to 20,000 psi, to minimize the risk of backflow between the mixed propellants. Additionally, both sides of the system are hooked up to a purge line, which also contains a Westlock falcon solenoid valve and HIP check valve. The nitrogen purge lines are connected to the Zucrow labs bulk nitrogen supply, in order to ensure that the entire system can be purged if necessary. An overhead view of part of this system is also presented in Figure 3.10.

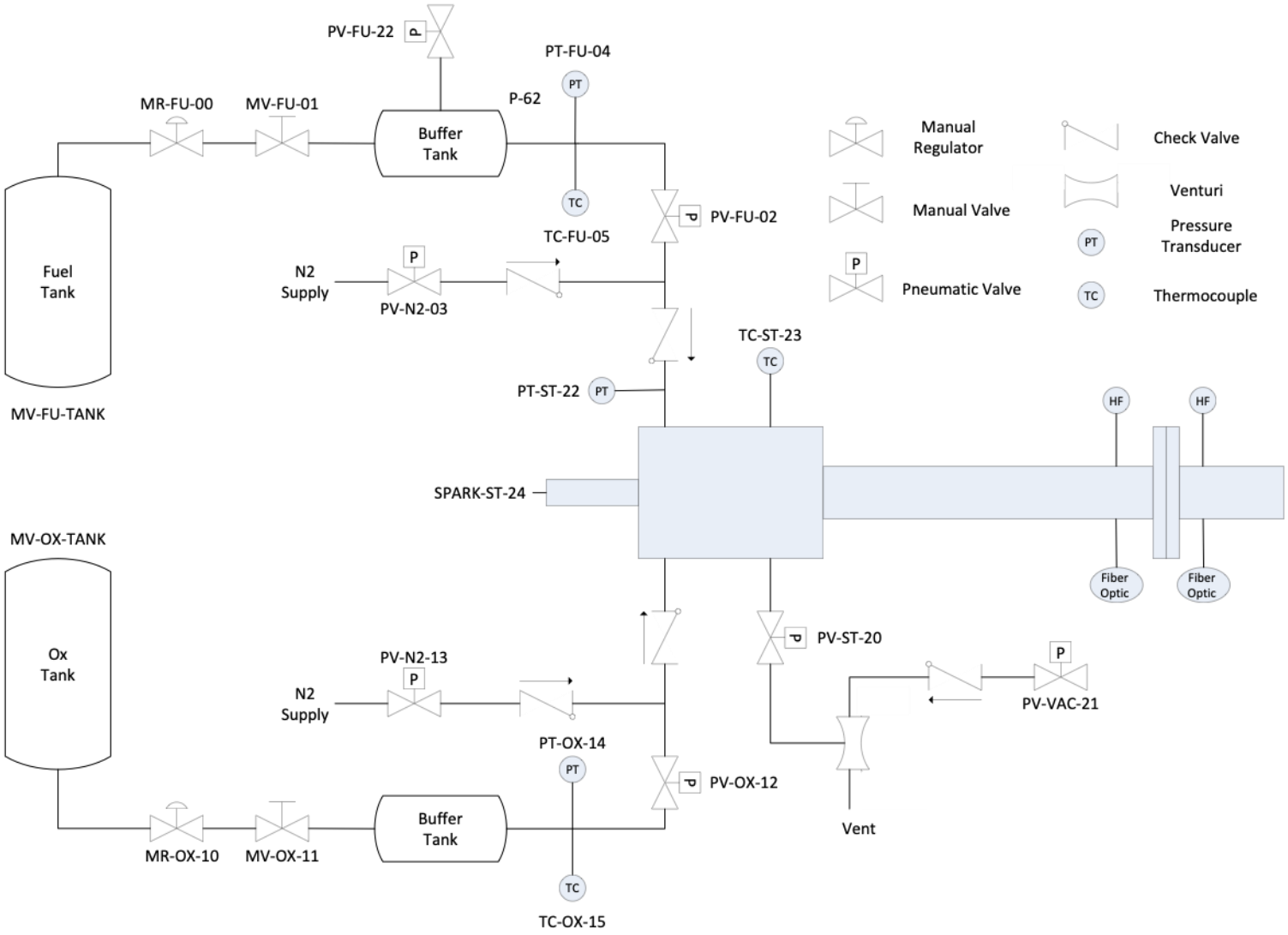

Figure 3.9: Plumbing and instrumentation diagram of the main shock tube

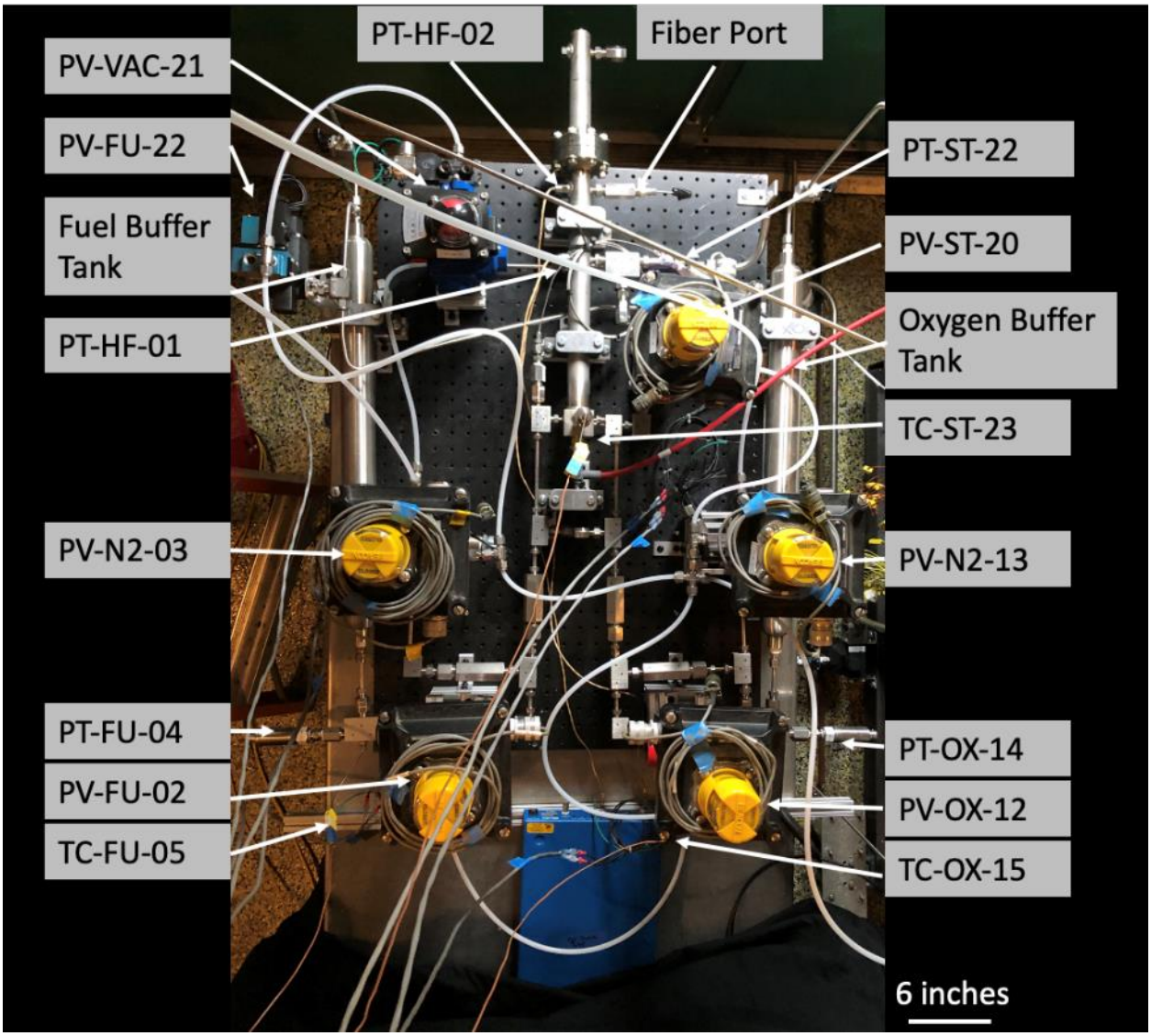

Figure 3.10: Overhead view of the plumbing and instrumentation leading to the main shock tube

The fuel side of the system has an additional solenoid valve connected to the buffer tank. The valve PT-FU-22 draws the fuel buffer tank down to 1 psia before filling the fuel buffer tank with the fuel to limit nitrogen contamination. The oxygen buffer tank does not have a similar valve as the oxygen buffer tank is drawn down to vacuum through the shock tube. The fuel side valve limits cross contamination between the oxidizer and the fuel before testing by giving both buffer tanks separate purge paths.

At the exit of the shock tube there is one final Westlock falcon solenoid valve, which connects directly to a vacuum venturi. As with the buffer tanks, the internal shock tube pressure is drawn down to 1 psia before filling the system in order to limit contamination. Additionally, the

venturi allows for a full system purge in the event that there is an issue during a test campaign where the mixed combustion gases do not ignite, or if they do ignite and fail to burst the burst disk. The vacuum venturi is driven by an A-CHEM valve, which is connected to the Zucrow labs bulk nitrogen system. As this part of the system will never see shock tube pressure, it did not use HiP tubes but rather used Swagelok fittings on a ¼ inch stainless steel tube.

There are three Druck UNIK 5000 pressure transducers attached to the system. Each of these transducers is rated to 2,000 psia, and all three transducers are used to monitor pre-detonation conditions. There is one pressure transducer on each buffer tank. As the propellants are pressure fed into the shock tube, the pressures in the buffer tanks need to be monitored in order to get an accurate estimate of the mixture ratio of each test. The third pressure is attached to the shock tube itself and is used to monitor the pre-detonation chamber pressure in the shock tube. Since the pressure transducer, only rated at 2,000 psia, cannot withstand the shockwave, it is protected by a long 1/16-inch coil of stainless steel. The coil of tube isolates the pressure transducer enough that the short-lived shock wave does not reach the pressure transducer before the pressure has fallen, but the pressure transducer can still get an accurate estimate of the chamber pressure. Two additional HEM-375-20000A Kulite pressure transducers are located at the same locations as the optical ports on the shock tube. The Kulite pressure transducers are rated to 20 ksi with a frequency response of more than 400 KHz. They are used to monitor pressure during testing – particularly the detonation wave pressure – as well as the detonation speed based on the known distance between the two pressure transducers. Finally, there are three 1/16th Omega K type thermocouples at the same locations as the UNIK 5000 pressure transducers, which measure the pre-test temperatures. These thermocouples are rated to 2200 degrees Fahrenheit, which is below the expected test temperatures that these thermocouples were expected to experience.

3.3 Operation

Several steps are required in order to run a shock tube test. First the burst disk had to be secured to the end of the shock tube, or in between the main shock tube and the extension tube. For low pressure tests with chamber pressures less than 100 psia, this involved sandwiching a HDPE burst disk between the main tube and a spare CF flange, while for high pressure tests a brass burst disk was placed in between the CF flanges on the main tube and the extension tube. The CF flanges have a torque specification of 192 inch-pounds per bolt, and these were tightened down in

a star pattern using settable torque wrench. The HDPE burst disks were clamped between a copper and a rubber gasket to prevent the plastic burst disks from tearing against the CF flange knife edge. The brass burst disks were aligned with the copper gaskets, which successfully sealed without risk of tearing the brass. The two flanges were then bolted together using eight bolts that were tightened using a star pattern in order to prepare the system for testing. An image of the full low-pressure system is shown in Figure 3.11, while Figure 3.12 shows the full high pressure test system.

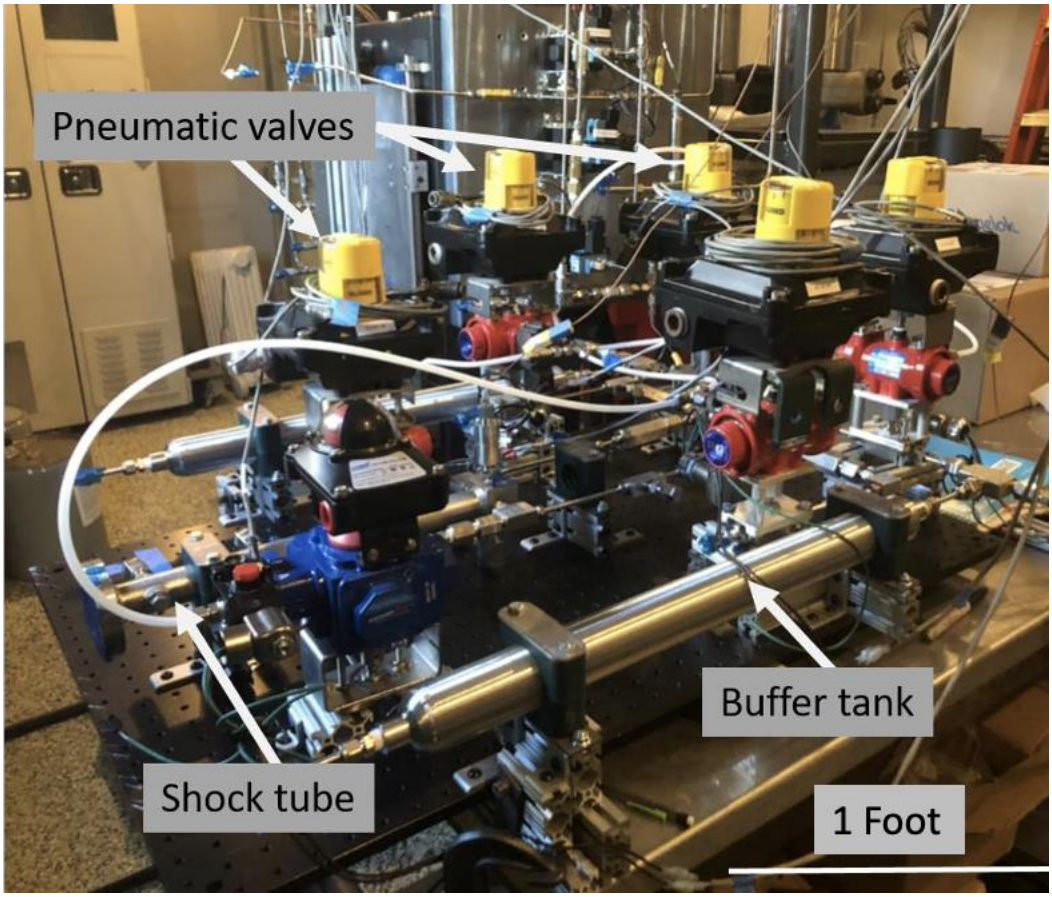

Figure 3.11: Low pressure full shock tube assembly

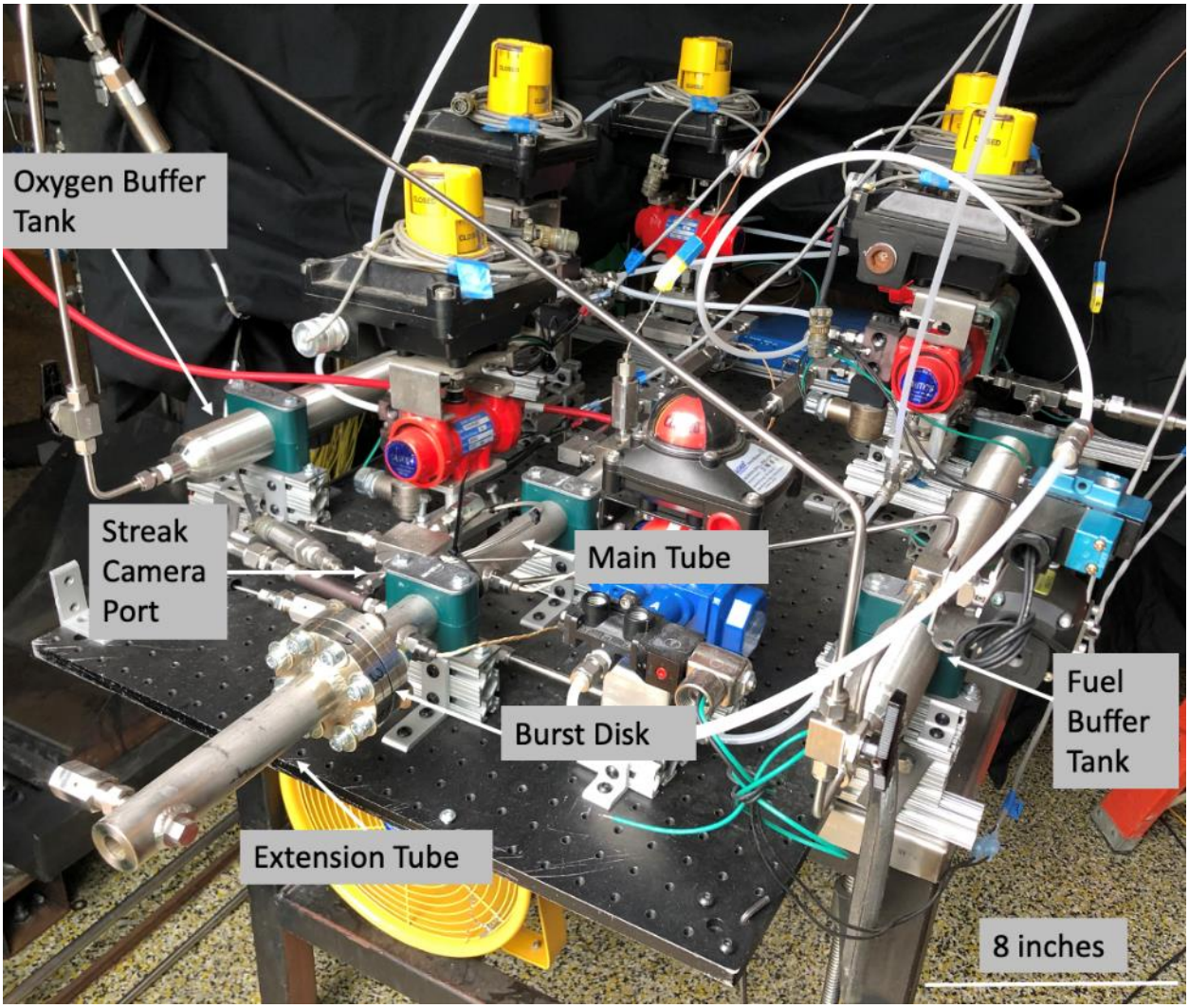

Figure 3.12: High pressure full shock tube assembly

Once the shock tube was sealed, the system was purged with nitrogen. The valves are actuated with 100 psig of nitrogen provided by the pilot regulator. The fuel side of the system is then purged with 100 psig of nitrogen by opening PV-N2-03 as indicated in Figure 3.10. PV-ST-20 is then opened, which expels the nitrogen gas and any other contaminants through the vacuum venturi. The purging process is repeated several times. Next the oxygen side of the system is purged by opening PV-N2-13 through the same procedure. During this process, the oxygen tank is drawn down to 5 psia, as that is the cracking pressure of the check valve. It will be further purged once oxygen is introduced into the system in order to ensure there is minimal nitrogen contamination. Once all of the lines are purged and all of the valves are closed, PV-FU-22 is opened to draw the fuel tank down to 1 psia.

The locations of all personnel are verified at this point so propellant loading can begin. The oxygen and fuel regulators are set to their desired pressures based on the desired mixture ratio, and the buffer tank isolation manual valves are opened so that the propellants can enter the buffer tanks for shock tube loading.

Valve PV-OX-12 is opened to fill the shock tube with oxygen. The system is then purged using the vacuum venturi three additional times. The three purges ensure that any remaining nitrogen is expelled from the shock tube and oxygen buffer tank, and allows for the shock tube to be conditioned with the gaseous oxygen before the tests begin. Finally, the shock tube is loaded to the desired oxygen pressure and the oxygen buffer tank is isolated from the shock tube.

With the shock tube full of oxygen, PV-FU-02 is opened so the fuel can also fill the shock tube. The fuel fill valve is kept open for the minimal amount of time it takes for the shock tube to reach the desired test condition before PV-FU-02 is also closed. At this point all of the desired propellant is within the shock tube, and those propellants are left to mix for 180 seconds. The 180 second mixing time was set after several initial low-pressure tests, because the oxygen and hydrogen gases need time to fully mix or the system would not ignite. After that time, the autosequence is activated. The autosequence triggers the cameras, the spectrometers, the Kulite pressure transducers, and the spark plug to record the detonation. Finally, once the shock tube has had a detonation, or if there has been no detonation, the shock tube purge valve PV-ST-20 is opened to draw out any remaining combustion products or propellants, and the entire system is fully purged with nitrogen for 30 seconds. Once the system is fully purged it can be reset for further testing.

4. RESULTS AND DISCUSSION

There were three test campaigns during this project. The first test campaign used background oriented schlieren and the Black-Comet spectrometer to measure the detonation properties of detonation waves up to 3,000 psia. The second test campaign used the Kulite pressure transducers to measure detonation peak pressure and wave speed up to 10,000 psia burst pressure. The final test campaign used the streak camera to measure detonation properties of detonation waves up to 13,000 pisa.

4.1 Low Pressure Test Campaign

The first tests done using the shock tube were conducted at low initial pressures in order to verify system functionality. Early driving pressures were limited to 50 psi to make sure the system was structurally sound and that the technical equipment would function well during the test duration. Initial tests all used HDPE film burst disks, which when tested with nitrogen were recorded to rupture at 120 psi. As such, fill pressure could be kept low in order to fill and mix without bursting the plastic burst disk.

Data collection during these early tests was limited to a single Kulite pressure transducer, a thermocouple, and a 2,000-psi Druck UNIK 5000 pressure transducer. A matrix of the first three test cases is given below in Table 4.1. The uncertainty on the chamber pressure value is determined by the Druck UNIK 5000 pressure transducer that have a full-scale accuracy of 0.25%. The mixture ratio uncertainty is a considers the uncertainties on all of the variables in Equation 3. The pressure ratings have the same full-scale accuracy $\pm$ 0.25% uncertainty as they are determined by the pressure transducers, while the molecular weights of hydrogen and oxygen were taken to three significant figures for this calculation. These measurements have a small associated uncertainties that are listed in Propagation of Uncertainty by David Harvey. The values associated with the molecular weight uncertainties however are far smaller than the uncertainties associated with the pressure transducer measurements, and as such, the uncertainty on the mixture ratio, *MR*, was primarily driven by the pressure transducer. Equation 4 gives the full uncertainty equation for the mixture ratio of this system.

Table 4.1. Early Test Campaign Chamber Conditions and Ignition Status

Test Number	Chamber Pressure [psi]	Mixture Ratio	Mixing Time [s]	Ignition?
IT_1	30.1 ± 5	17.4 ± 0.1	14	No
IT_2	40.2 ± 5	11.4 ± 0.1	60	No
IT_3	39.9 ± 5	9.4 ± 0.1	140	Yes

$$\left(\frac{U_{MR}}{MR}\right)^2 = \left(\frac{U_{Pox}}{P_{ox}}\right)^2 + \left(\frac{U_{PH2}}{P_{H2}}\right)^2 \quad (4)$$

As shown in Table 4.1, the first two tests did not ignite. We determined that the first test likely did not ignite due to the mixture ratio being far too high because of issues getting the proper mixture ratio by using partial pressures. The second test also did not ignite. We determined that the cause of this ignition failure was likely due to the fuel and oxidizers having very short mixing times. The short mixing time led to variable mixture ratios throughout the shock tube with significantly more hydrogen near the spark plug. The third test had a far longer mixing time period of 180 seconds and ignited. As such, a 180 second mixing time was applied to all future test cases. Figure 4.1 shows a typical detonation event. It can be noted that while the flame components were oxygen and hydrogen, the flame appears orange due to the carbon in the burst disk burning up after impact.

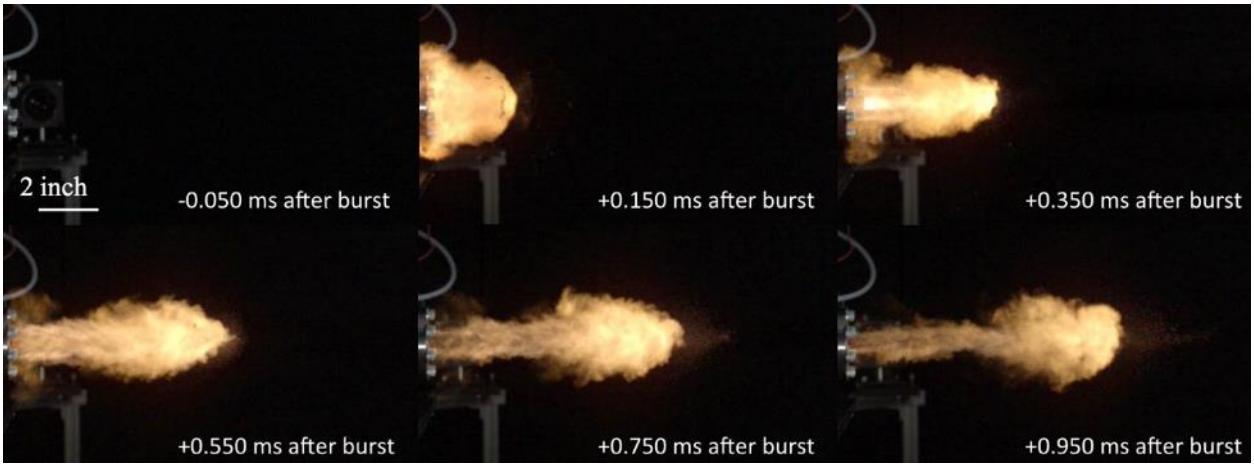

Figure 4.1: Typical low pressure shock tube detonation event

One problem that occurred during these preliminary tests was that the 2,000-psi pressure transducer that was used to measure chamber pressure and mixture ratio did not survive the first detonation. We had predicted that that specific pressure transducer was close enough to the spark plug that it would not observe the extreme shock pressures. However, after the first detonation the pressure transducer failed and never recovered due to pressure overload. In order to protect the next pressure transducer, the next pressure transducer was connected to a long, coiled 1/16th inch tube, which was then connected to the shock tube. The 1/16th inch tube dissipates the worst of the shock energy and stops any high-pressure reflections from reaching the pressure transducer, thus protecting it during all later tests. Beyond those issues, the system functioned as expected and we began testing with the low-pressure test matrix.

The instrumentation used for the low-pressure tests was more intensive than for the preliminary health checks. Two high pressure, 20,000 psi rated HEM-375-20000A Kulite pressure transducers were implemented four inches away from each other. The known distance between the two Kulite pressure transducers allowed us to measure the pressures of the shock wave along the tube and the velocity of the shock wave. The first Kulite pressure transducer, PT-HF-01, was four inches closer to the ignition point than the second Kulite pressure transducer, PT-HF-02. A common pressure trace for these experiments is shown in Figure 4.2. Based on these pressure traces, we could manually select the data point immediately after the Kulite saw a pressure rise. As these data points are time stamped, we could then determine how much time it took for the pressure wave to move the 4-inch distance between PT-HF-01. Knowing that time and distance, we could calculate the velocity with an uncertainty of one data point, because the exact moment that the high-pressure wave reached the Kulite happens sometime between the last data point with no response, and the first data point the Kulite responds. Equation 5 shows the equation used to calculate velocity. In Equation 5, V is the wave speed, d_{PT} is the distance between the pressure transducers, and t_{PT1} and t_{PT2} represents the time when the detonation wave passes by Kulites number one and two respectively.

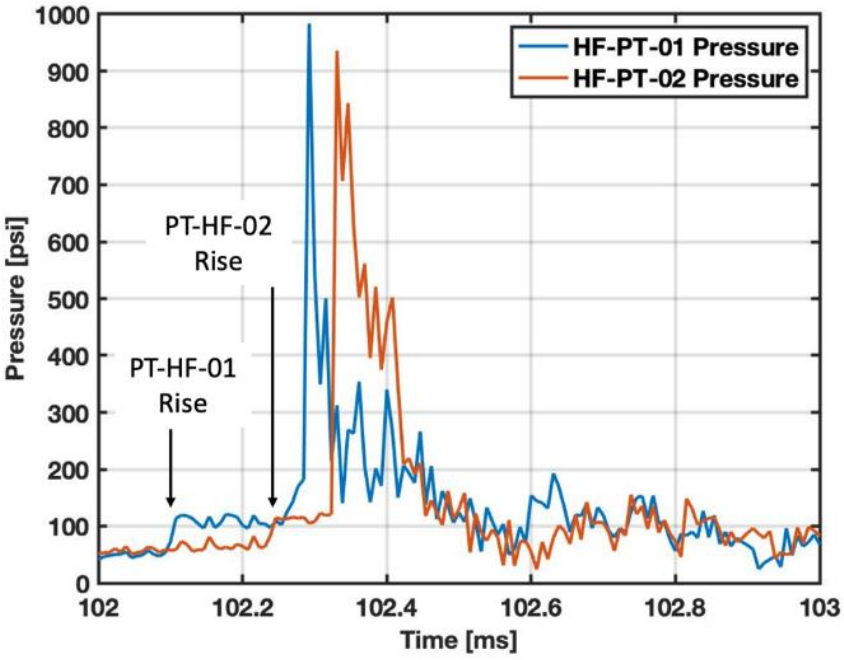

Figure 4.2: Low pressure Kulite plot showing detonation curve

$$V = \frac{d_{PT} * 0.0254 \left(\frac{m}{in}\right)}{(t_{PT2} - t_{PT1})/130{,}000 \frac{hz}{s}} \tag{5}$$

Additionally, the Stellarnet Black-Comet SR Spectrometer was connected to the end of the fiber probe that corresponded to the second Kulite. While this spectrometer has far less temporal resolution than the Sydor streak camera used in later tests, we theorized that it may provide one or two data points during and immediately after the shock wave. We were also interested in seeing if we could gather the required emission data needed for chemiluminescence thermometry.

Finally, we set up the high-speed camera and prepared the background dot-patterns for several of these low-pressure detonation tests in order to take background oriented schlieren data. BOS was implemented for the low-pressure tests to determine if the measurement technique provided accurate data. Detonation events are violent, and we did not want to risk the high-speed camera on a high-pressure test before validating BOS as a measurement technique. The test matrix for the low-pressure tests is shown below in Table 4.2. In Table 4.2, tests labelled IT_# represent initial tests that were done primarily for calibration purposes, while the tests labelled LP_#

represent the low-pressure tests that generated data used for background oriented schlieren and spectroscopy. As with Table 4.1, the uncertainty on the chamber pressure and mixture ratio are both once again based off of the Druck UNIK 5000 pressure transducer full-scale accuracy of 0.25%, with the mixture ratio once again being calculated with Equation 4. The Kulite pressure transducers have a full-scale accuracy of ± 0.5%, which influences the measurements of PT-HF-01 and PT-HF-02. The last uncertainty of interest was on the wave speed calculation, where the uncertainty of the distance between the two Kulite pressure transducers was known to be 0.005 inch, and the uncertainty in the time measurement was known to be 8 microseconds (this value correlates to one data point at 130,000 H recording rate). Equation 5 shows the wave speed uncertainty calculation.

Table 4.2: Low pressure test campaign chamber conditions, final pressures, and estimated detonation velocities

Test Number	Chamber Pressure [psi]	Mixture Ratio	Mixing Time [s]	Pressure reading PT-HF-01 [psi]	Pressure reading PT-HF-02 [psi]	Estimated detonation velocity [m/s]
IT_4	43.8 ± 5	8.8 ± 0.1	180+	No Ignition	No Ignition	No Ignition
IT_5	43.2 ± 5	9.5 ± 0.1	180+	1,565 ± 100	1,392 ± 100	2,540 ± 510
IT_6	46.2 ± 5	7.5 ± 0.1	180+	1,671 ± 100	1,581 ± 100	2,639 ± 550
IT_7	42.6 ± 5	7.8 ± 0.1	180+	699 ± 100	2,012 ± 100	1,652 ± 220
IT_8	42.4 ± 5	7.7 ± 0.1	180+	977 ± 100	930 ± 100	2,639 ± 550
IT_9	44.0 ± 5	8.0 ± 0.1	180+	752 ± 100	1,584 ± 100	3,299 ± 857
IT_10	43.8 ± 5	8.1 ± 0.1	180+	905 ± 100	1,844 ± 100	1,652 ± 220
IT_11	43.9 ± 5	8.1 ± 0.1	180+	696 ± 100	2,859 ± 100	1,101 ± 96
IT_12	44.7 ± 5	8.2 ± 0.1	180+	1,294 ± 100	1,039 ± 100	1,652 ± 220
LP_1	45.4 ± 5	8.2 ± 0.1	180+	1,324 ± 100	1,400 ± 100	3,299 ± 857
LP_2	44.6 ± 5	6.1 ± 0.1	180+	354 ± 100	1,853 ± 100	880 ± 62
LP_3	45.6 ± 5	10.2 ± 0.1	180+	1,551 ± 100	1,220 ± 100	2,204 ± 383
LP_4	80.1 ± 5	8.5 ± 0.1	180+	1,498 ± 100	1,946 ± 100	3,299 ± 857
LP_5	79.8 ± 5	6.3 ± 0.1	180+	2,682 ± 100	1,492 ± 100	3,299 ± 857
LP_6	79.8 ± 5	10.3 ± 0.1	180+	1,505 ± 100	1,553 ± 100	2,639 ± 550
LP_7	44.3 ± 5	8.0 ± 0.1	180+	476 ± 100	2,034 ± 100	3,299 ± 857

$$V = \frac{d_{PT} * 0.0254 \left(\frac{m}{in}\right)}{(t_{PT2} - t_{PT1})/2{,}000{,}000 \frac{hz}{s}} \tag{5}$$

While the pressure data is relatively reliable, the limited recording speed resulted in very high uncertainty on the velocity measurements. In general, only one or two data points would separate each test, resulting in very high uncertainty and highly variable pressure measurements. In order to gather more accurate data, we purchased a new data acquisition system that improved our recording rate from 130,000 Hz to 2,000,000 Hz. The new high recording rate DAQ was implemented for our high-pressure test campaigns.

There were several lessons learned from this test setup. Using the pressure transducers, we tracked the transformation of the shock wave from deflagration event to detonation event for the lowest driving pressure cases. We named these phenomena Type 1 and Type 2 pressure waves. For the table above, a Type 1 pressure wave occurred when both Kulite pressure transducers saw a detonation wave – notable by an immediate rise in pressure. This immediate rise in pressure, with very little pressure build up, was the main pressure trace we expected to see in the system. For a Type 2 pressure wave, the pressure transducer closest to the spark plug – PT-HF-01 – saw a slow rise in pressure that is well documented as being the pressure trace of a deflagration wave. The second transducer further downstream – PT-HF-02 – saw the standard detonation wave. A comparison between these two waves is given in Figure 4.3. For the higher chamber pressure test cases – beyond 45 psi driving pressure – both Kulite pressure transducers saw only detonation waves, which indicated to us that the detonation wave was well developed far before it reached the pressure transducers. Additionally, the shift in detonation mode greatly changed the pressure recorded between the two Kulite pressure transducers, as the detonation case produced much higher velocities than the deflagration cases, which was expected due to the wave characteristics.

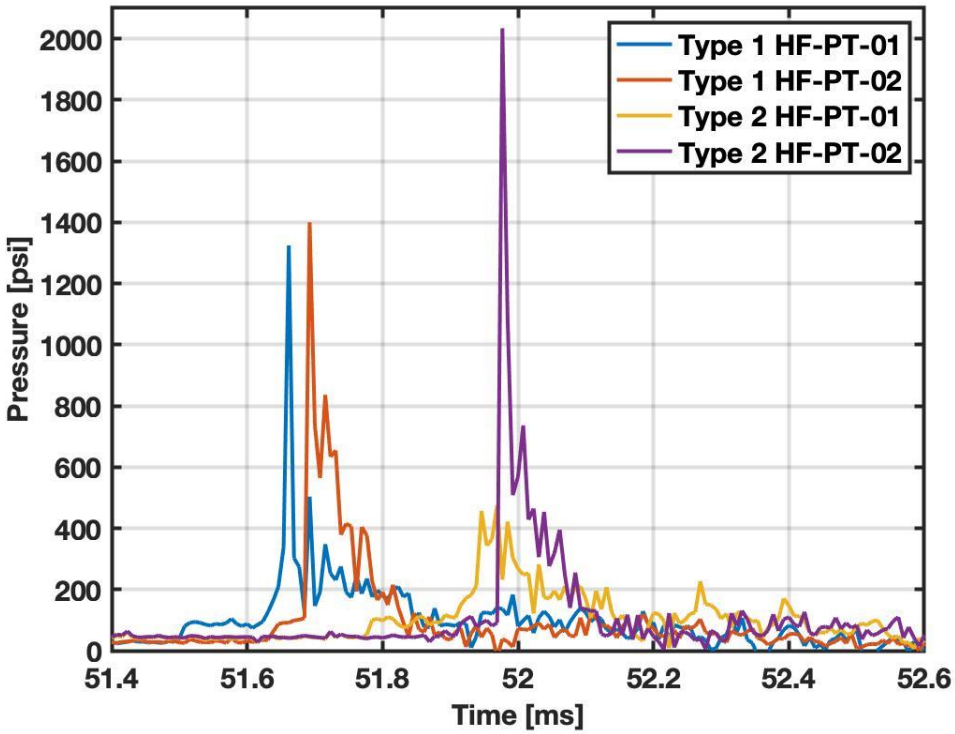

Figure 4.3: A pressure trace comparison between a common deflagration and detonation plot

From these low-pressure tests there was some interesting background oriented schlieren data. An example of the raw background oriented schlieren data gathered during this test campaign is given below in Figure 4.4. The timestamps for these raw data files are based on the data collected using the Phantom high-speed camera, and have an uncertainty of one pixel, or 8 microseconds, on the speed the camera recorded data at. These recording settings were kept constant for all test cases where BOS data was collected.

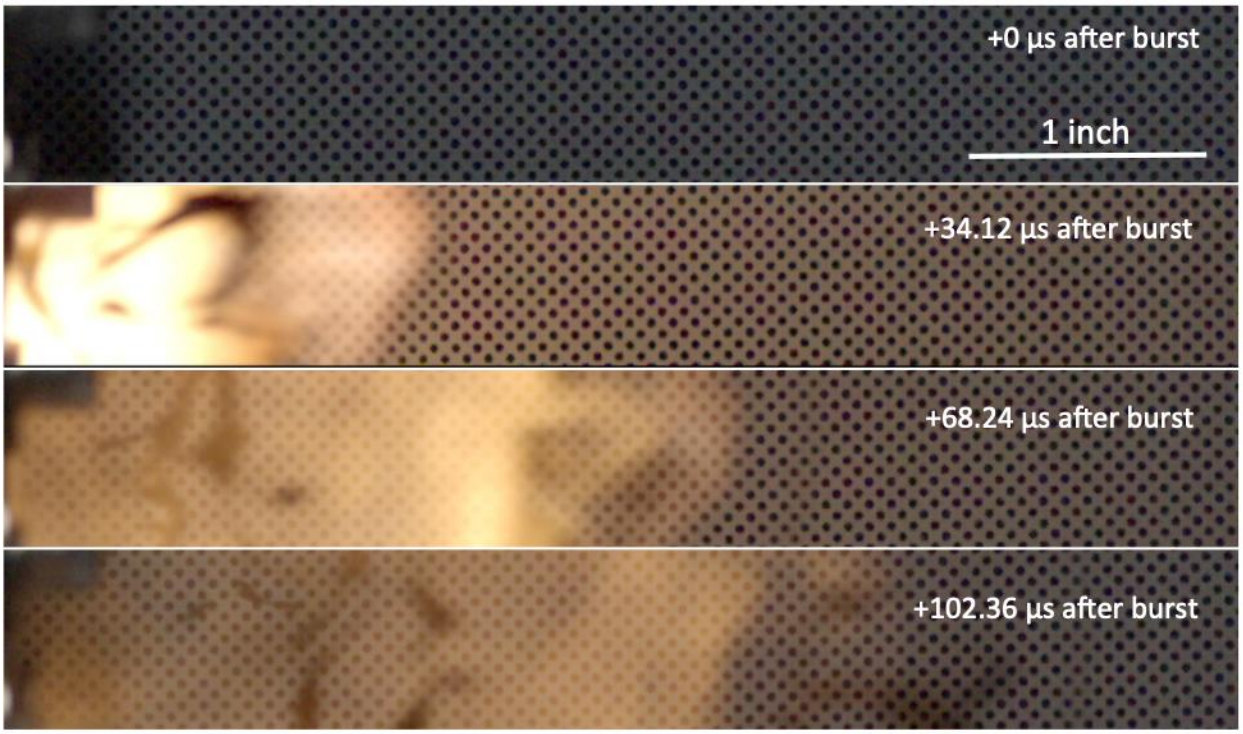

Figure 4.4: Unprocessed background oriented schlieren data with time stamps for a mixture ratio of eight and a driving pressure of 45 psia

The flames at the exit of the shock tube make it difficult to collect meaningful density data because they are bright enough to block the dotted pattern that the BOS code needs to analyze the change in density. However, the shock wave leaving the end of the detonation tube and the small layer of low-density combustion products immediately after the shock wave can be well recorded during this process. Given the raw data, we calculated the change in density relative to the original image using the BOS code discussed in Chapter 2. Figure 4.5 gives a comparison between these results in order to relate the detonation pressure density to the original density. All of the data presented in Figure 4.5 is based on the images at $68 \pm 4\ \mu s$ after the detonation wave burst the burst disk, in order to compare the results of the various mixture ratios and driving pressures at similar times. The first column in Figure 4.5 shows data for the 45-psi driving pressure test cases, while the second column shows the data for the 80 psi driving pressure cases. The first row of Figure 4.5 shows the low mixture ratio cases (O/F = 6), the middle row shows the stoichiometric mixture ratio case (O/F = 8) and the final row shows the high mixture ratio case (O/F = 10) for their respective pressures.

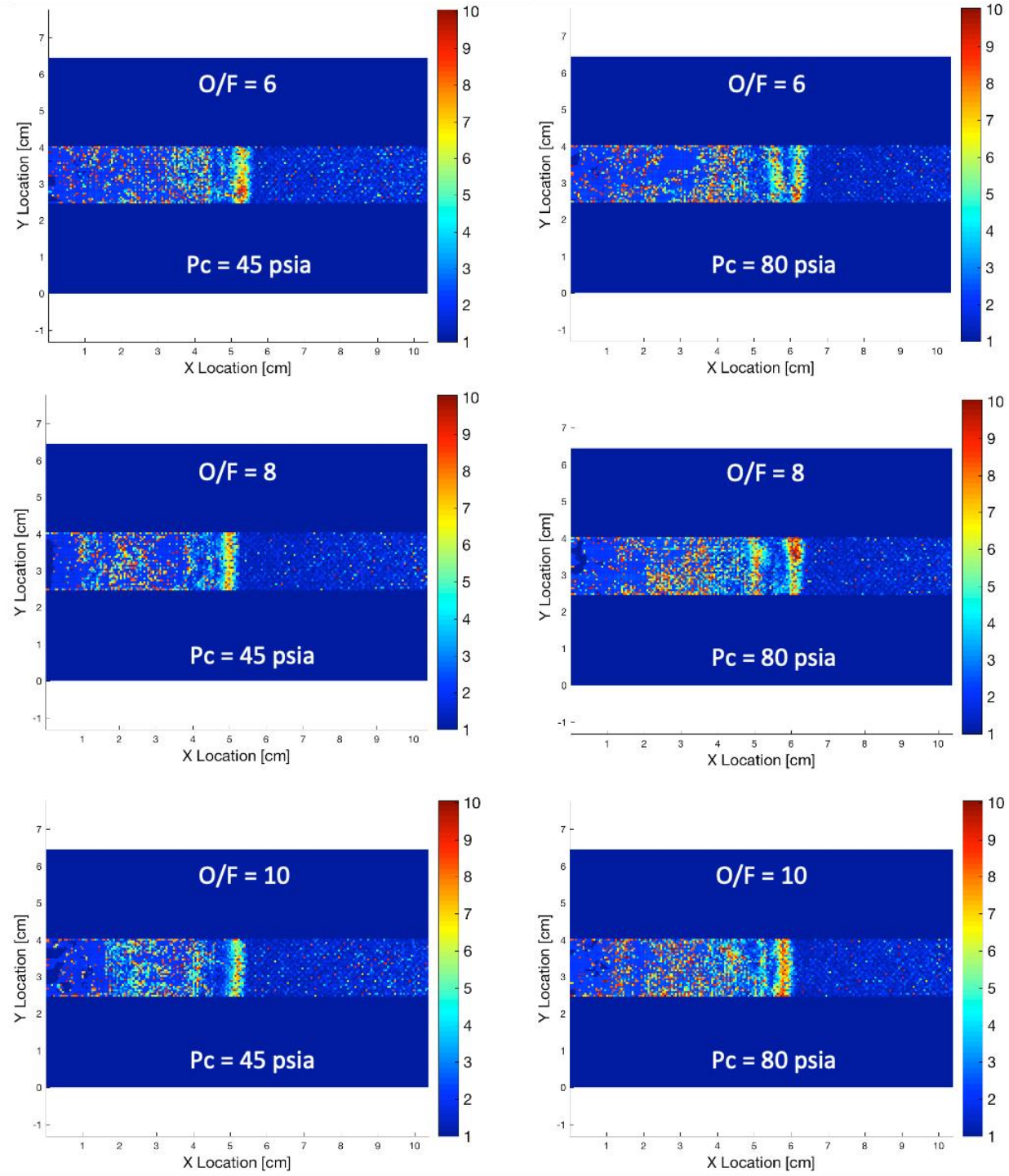

Figure 4.5: Post processed background oriented schlieren data comparing the pressure gradient for various driving pressures and mixture ratios

There were several interesting trends observed based on this data. The width of the shock wave appears to increase with an increased driving pressure. We speculated that this was due to the increase in oxygen, which is a far larger molecule than hydrogen. The detonation speed

appeared to be highest for the lowest O/F case no matter what the driving pressure is. The difference in wave speed was consistent with previous data reported by Gaydon and Hurle (1963) and with the calculated velocity based on peak pressure measurements from the two Kulite pressure transducers.

Given the analyzed data, we can derive density trends over the course of the detonation event for all conditions of interest. The post detonation density was calculated at two locations. The first location compared the density of the fast-moving gases immediately behind the detonation wave to the density of the undisturbed air. The second location compared the density of the equilibrium gases farther behind the detonation wave to the density of the undisturbed air. As this generated a lot of data due to the size of the image, we calculated an average for these values. The averages of these values are given in Table 4.3. The fourth row of Table 4.3 gives the ratio of the densities recorded immediately after the shock wave exited the detonation tube. These densities were recorded to be roughly twice that of the outside air. The fifth row of Table 4.3 gives the density ratio of the better developed gases further away from the detonation tube exit. The density of these cases generally increased to about five times that of the air density. The oxygen rich cases saw a higher post detonation density than the fuel rich cases for both analyzed test sets, which is consistent with results given by Gaydon and Hurle (1963). Higher pressure detonation events also generally saw higher final densities, which was also expected.

The uncertainty on the density gradient measurements is based on the uncertainties associated with equation 2, which most prominently was related to the air density during each test and the schlieren image width. The air density varied slightly with pressure each day, and the schlieren image thickness was assumed to be 0.6 inches wide – which was the same as the exit diameter of the shock tube – as both density gradients were analyzed within an inch of the shock tube exit. Further, imperfections in the images from the flow due to burst disk debris also contributed to a rise in the uncertainty of these measurements, as the plastic blocked parts of the image from being analyzed. Ultimately these issues lead to relatively high uncertainty on all of the density gradient measurements, making it more difficult to determine the actual density gradient at the exit of the detonation tube.

Table 4.3. Average density values calculated at the shock tube exit for the post shock for the above image

Test Number	**Pc [psia]**	$\frac{O}{F}$ **[-] [-]**	$\frac{\rho_2}{\rho_1}$ **[-]**	$\frac{\rho_3}{\rho_1}$ **[-]**
LP_1	44.6 ± 5	6.1 ± 0.1	1.9 ± 0.4	4.3 ± 0.4
LP_2	45.4 ± 5	8.2 ± 0.1	2.1 ± 0.4	4.9 ± 0.4
LP_3	44.3 ± 5	8.0 ± 0.1	2.2 ± 0.4	4.7 ± 0.4
LP_4	45.6 ± 5	10.2 ± 0.1	2.3 ± 0.4	5.1 ± 0.4
LP_5	80.1 ± 5	6.3 ± 0.1	2.2 ± 0.4	5.2 ± 0.4
LP_6	79.8 ± 5	8.5 ± 0.1	2.3 ± 0.4	5.3 ± 0.4
LP_7	79.8 ± 5	10.3 ± 0.1	2.6 ± 0.4	5.5 ± 0.4

There were several problems with the use of the background oriented schlieren method for this system. Not all of the low-pressure test cases recorded data that could be analyzed and post processed. Several times during the higher driver pressure cases the force of the shock exiting the detonation tube completely shifted the dot pattern background and the thick plastic plate it was attached to. As the entire dot pattern shifted, the dot pattern could not be correlated to the calibration image and the data was not useful. Additionally due to the power of the shock wave and contamination from the burst disk in the flame, even the usable background oriented schlieren data was remarkably noisy. The noise level was not observed during early testing with the background oriented schlieren analysis code and other test cases that were in better equilibrium than the high speed, violent shock tube testing. Finally, during testing it was often difficult to gather data within the detonation event, as the brightness of the flame washes out the dot pattern and makes it impossible to track the changes in the air density. We had no good way to dim the flames, which meant we lost significant portions of the data due to be unable to see the background. Because of those reasons we decided not to continue taking background oriented schlieren data for the high-pressure test cases, especially as there was no good way to ensure that the dot pattern would not move when exposed to the higher-pressure shock wave.

The second main method of data collection of interest was taking spectrometer data using the Black-Comet spectrometer. In order to run the spectrometer, we set the system to burst mode to gather one data point every 4 milliseconds. Four milliseconds is a much longer time frame than

the shock wave exists in the system for, but at this speed the spectrometer had the potential to capture one or two data points immediately behind the shock wave during each test. The OH* radical was only observed once using this analysis method at a mixture ratio of six and a chamber pressure of 45 psi. Figure 4.6 showed the highest intensities of OH* at 308 nanometers. It can be noted that the OH* peak is dwarfed by other spectrometer readings, making it difficult to reliably gather any data from the Black-Comet spectrometer at these conditions.

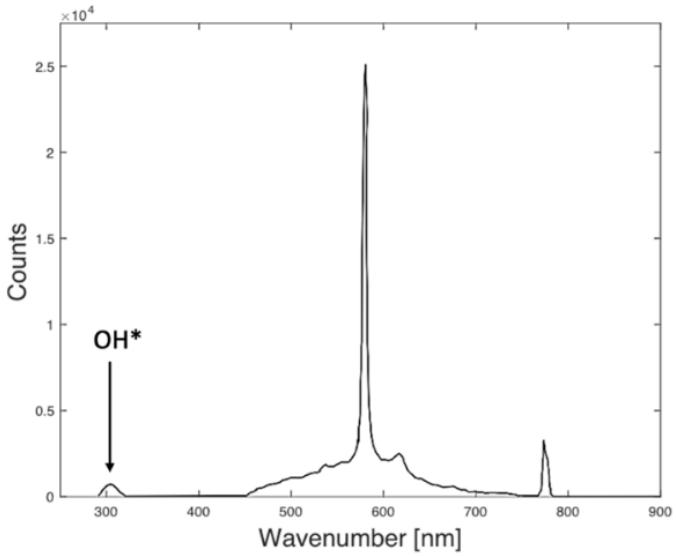

Figure 4.6: Black Comet spectrometer readout for mixture ratio of six and a chamber pressure of 45 psi

There are several different emission lines shown on the plot above. The most prominent line is the peak at 588 nanometers, which appeared in every test. The peak at this wavelength corresponds to a sodium peak. Sodium peaks appear in almost all flame spectroscopy, even for clean systems, and they are incredibly bright. Unfortunately, while the sodium peak does indicate that the spectrometer functioned during every test, it does not provide any useful information. The peak around 775 nanometers (Kurucz and Bell 1995) is most likely an oxygen peak. A similar peak was observed for the same chamber pressure at the mixture ratio of 8, as shown in Figure 4.7.

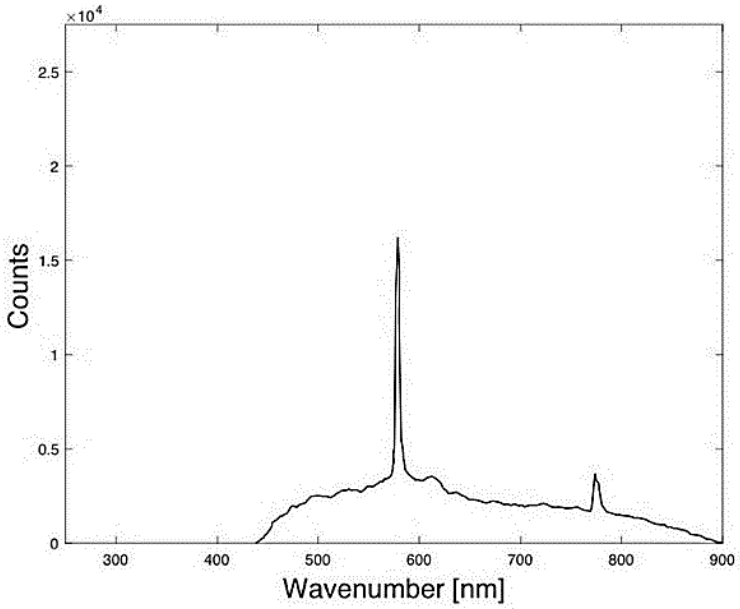

Figure 4.7: Black Comet spectrometer readout for mixture ratio of eight and a chamber pressure of 45 psi

Once again, Figure 4.7 shows a high intensity peak at 588 nanometers and a small peak at 775 nanometers. However, even the sodium line in this spectrum has a lower intensity count than for the spectrum observed in Figure 4.6, and there is no observable peak at 308 nanometers to represent OH*. All of the other tests that with the Black-Comet spectrometer saw even lower intensities for all above peaks and never showed a peak at 308 nanometers. Because of this we only attempted to apply chemiluminescence thermometry to the data associated with Figure 4.6.

However, due to the low magnitude of the OH* radical peak we were unable to get any useful temperature data. We had several theories as to why we had trouble capturing the OH* peak reliably using the spectrometer. The primary suspicion is that the Black-Comet spectrometer is simply not fast enough to capture the short-lived equilibrium products immediately behind the shock wave. We further suspected that due to this the spectrometer is not sensitive enough to record any existing OH* radicals, particularly due to the high magnitude salt line. The analysis led us to conclude that the Black-Comet SR spectrometer could not be used for chemiluminescence thermometry on a detonation wave, and that in order to implement that diagnostic technique we needed a more capable instrument.

After analyzing all of the BOS and spectrometer data, we concluded the low driving pressure test campaign. While neither the BOS or Black-Comet spectrometer provided reliable data, the

Kulite pressure transducers captured both pressure and velocity data. The background oriented schlieren data was incredibly noisy, and there was no good way to secure the dot pattern screen so that it did not move during the detonation. If the dot pattern moved, we could not post-process the background oriented schlieren data. As such we did not implement this measurement for further tests. Meanwhile, while the Black-Comet spectrometer did on two occasions record an instance of non-equilibrium OH*, the instrument itself was not fast enough to suit the system needs. However, it did give us a good idea of how to implement the streak camera in order to gather emission data on equilibrium OH*, which has far better time resolution.

4.2 Initial High Pressure Test Campaign

Following the low-pressure test campaign, we moved towards testing the system at higher driving pressures. First, we needed to switch from the plastic to the metal burst disks, which were rated up to 3,000 psi burst pressure. The burst disks were machined at the Bechtel Innovation Design Center at Purdue university, using a laser cutter to both cut out the disks and score the brass to a depth of 0.01 inches. The perpendicular score marks were meant to separate into brass petals during a detonation test, allowing the combustion gases and pressure to escape the detonation tube. In theory these petals would curl upwards – not separating from the brass and creating shrapnel, however in the event that part of the burst disk became dislodged at high pressure, a wooden backstop was set up three feet from the exit of the shock tube. We determined that three feet was enough distance to guarantee that any dislodged petals would be caught, while not severely disrupting the flow characteristics at the exit of the tube. The backstop was used often during testing, as the burst disk petals almost always fully separated and exited the detonation tube. Figure 4.8 shows the burst disk before and the most common configuration of the burst disk after testing.

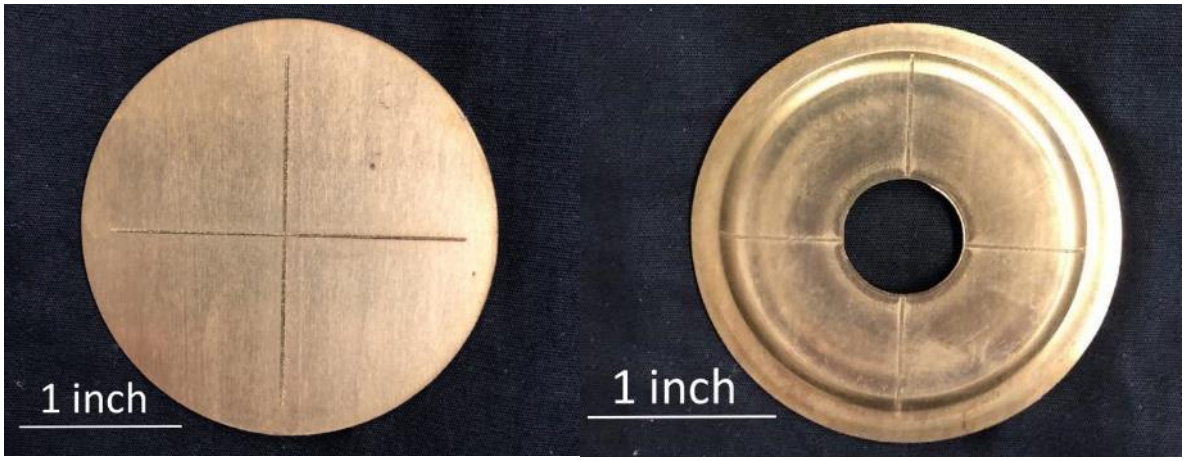

Figure 4.8: Brass burst disk before and after detonation testing during the initial high pressure test campaign

The data acquisition system (DAQ) was also updated to record at a high frequency and to better determine the detonation wave speed. The previous DAQ was limited to taking data at 130,000 Hz, whereas the new DAQ can gather data at up to 2,000,000 Hz. The improved data capture rate allowed us to gather far more accurate wave speed data by recording the time change between the pressure peaks recorded by both pressure transducers. A standard pressure trace for the high-pressure tests is shown in Figure 4.9.

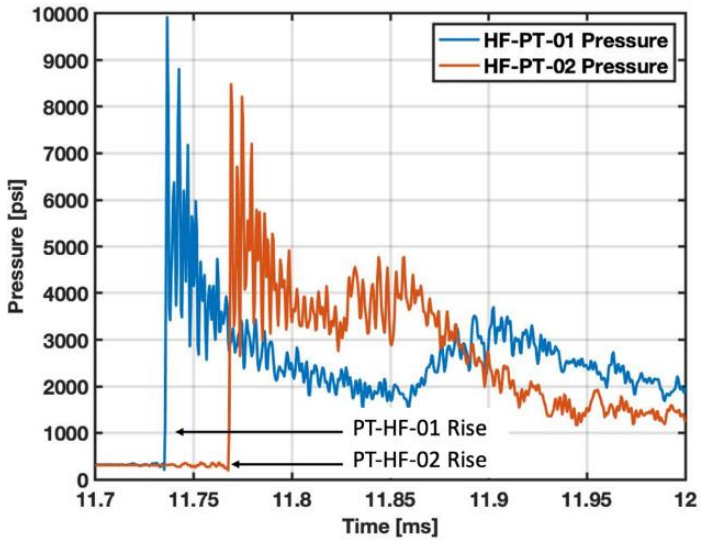

Figure 4.9: Common pressure trace recorded by the Kulite pressure transducers during a high chamber pressure test

Figure 4.9 shows a similar trend to the low-pressure test case from Figure 4.2, however none of the high-pressure tests saw the deflagration curve observed during some low-pressure tests.

All of the detonation tests saw an immediate rise in pressure as the detonation wave passed by the pressure transducers. The immediate pressure rise helped identify the moment immediately before the Kulite pressure transducer saw a pressure rise, which improved the overall wave speed uncertainty. Increasing the data capture rate allowed us to better estimate the time difference as well as get closer to the actual peak pressure value. A summary of the pressure data for the high-pressure test cases is in Table 4.4. These tests primarily focused on improving the estimated wave speed from the pressure transducer data. For the first high pressure test, we only used one pressure transducer in order to verify that that pressure transducer functioned well after the detonation. As with the low-pressure cases, the uncertainty on the chamber pressure is based on the 0.25% full scale accuracy of the Druck UNIK 5000 pressure transducer, and the uncertainty on the mixture ratio is calculated with Equation 4. The wave speed calculation, however, saw some improvement on the total uncertainty due to the increase in recording speed increasing to 2 MHz. The new uncertainty on the time step was 0.5 microseconds, or one data point, as all of the cases at high pressure were detonation waves where the first point of pressure rise was obvious, as can be observed in Figure 4.9.

Table 4.4. Internal shock pressures recorded during high-pressure test cases

Test #	**Pc [psia]**	**O/F [-]**	**HF-PT-01 [psia]**	**HF-PT-02 [psia]**	**Detonation Wave Speed [m/s]**
HP_1	291 ± 5	8.1 ± 0.1	7834 ± 100	-	-
HP_2	287 ± 5	8.0 ± 0.1	8931 ± 100	5984 ± 100	3,049 ± 46
HP_3	295 ± 5	8.0 ± 0.1	9928 ± 100	8484 ± 100	3,126 ± 49
HP_4	294 ± 5	6.1 ± 0.1	7766 ± 100	8616 ± 100	3,251 ± 54
HP_5	291 ± 5	9.9 ± 0.1	9414 ± 100	9032 ± 100	2,419 ± 29

As can be noted in Table 4.4, the wave speed was relatively easy to calculate based on the number of data points taken for each test case. The highest speed recorded was for the fuel rich test (HP_4), which matches prior literature, while the highest single pressure recorded was at stoichiometric conditions (HP_5). Previously the wave speed was more difficult to define due to

the limited number of data points available over the course of the detonation. The new hardware allowed us to track both peak locations and wave speed far better than with prior test campaigns. The wave speed was calculated by looking at the time between the peaks on both pressure transducers, and as the pressure transducers were known to be four inches apart, dividing that distance by the time between the transducers for each pressure test.

For the fuel rich test (HP_4), about 17 milliseconds after the peak of the first detonation, a second, slower moving detonation exited the shock tube. We attributed this second detonation to some excess fuel left in the tube following the initial detonation implying that there was some incomplete mixing during this test. The second peak reached a maximum pressure of 291 psi. Figure 4.10 shows the pressure trace for HF-PT-01 for this test. The second peak can also be seen in GoPro images taken during the tests, where several frames after the detonation, the camera would sometimes capture another small puff of fire. Figure 4.11 shows two of these images. The green coloring in the original flame is due to the burning of the copper in the brass burst disk.

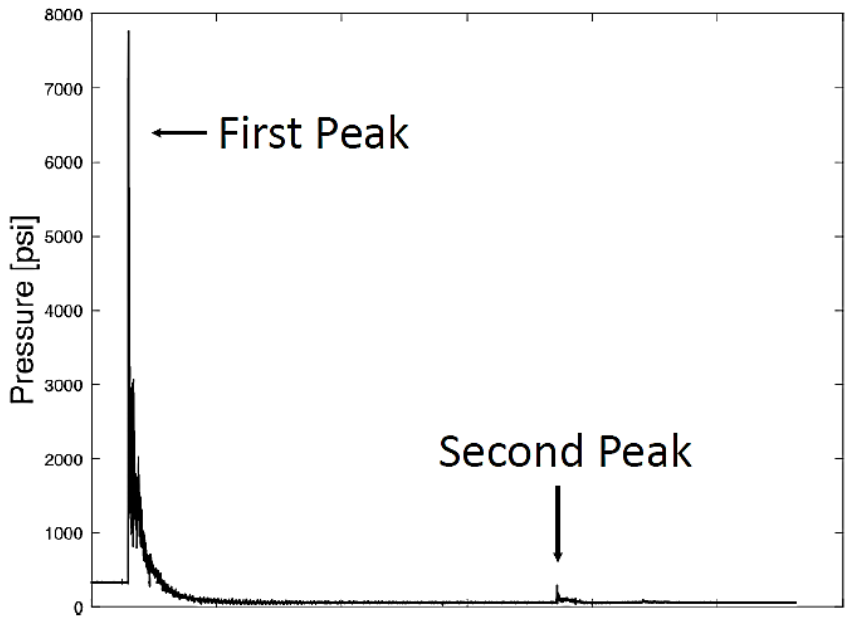

Figure 4.10: Pressure transducer results for the initial and secondary detonation during Test 4

Figure 4.11: Initial detonation tube flame and secondary smaller flame as captured by a GoPro camera during Test 4

Finally, we recorded high-speed videos of the high-pressure tests in order to estimate the wave speed after the detonation wave exited the shock tube. Figure 4.12 shows several images from test HP_5, with a chamber pressure of 291 psi and a mixture ratio of 9.9. It can be noted that the green coloration in the flame is due to the copper in the brass burst disks. The high-speed video produced an estimated wave speed of 253 m/s, which is lower than observed by the pressure transducers. We speculate that the reduction in speed is due to the burst disk pieces interfering with the flow, and due to the flow hitting the stagnant air at the exit of the shock tube. The images start 0.15 milliseconds after the burst disk bursts and the flow exits the shock tube.

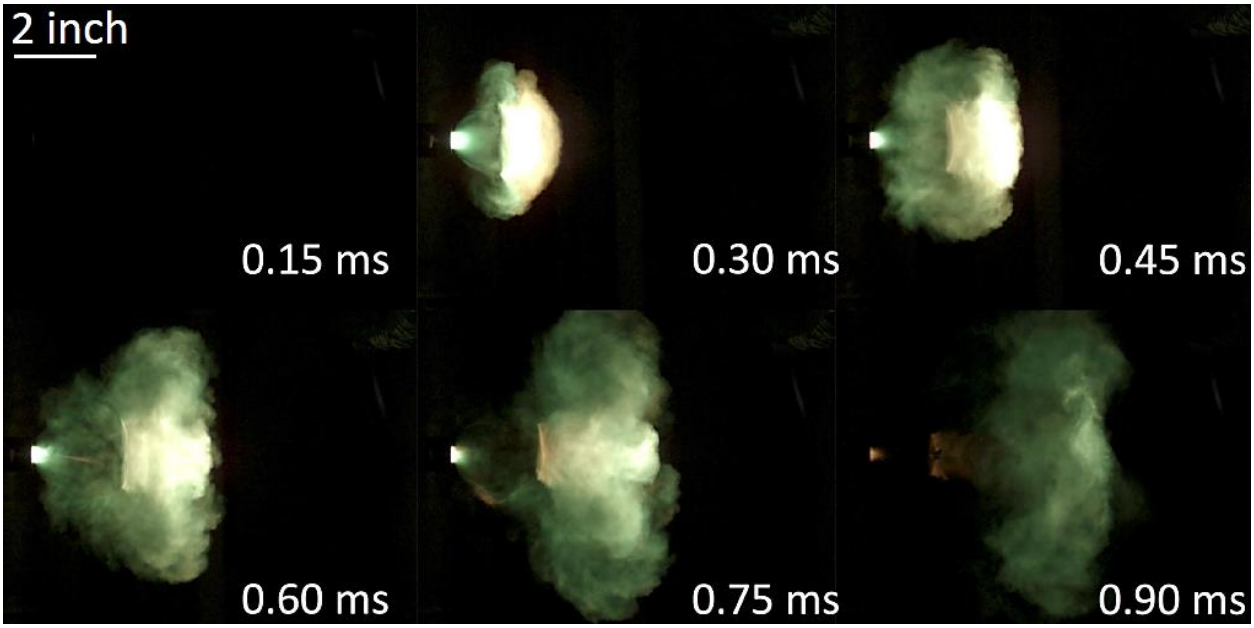

Figure 4.12: High pressure detonation flames captured with a high-speed camera during test 5

Given these results and the results from the low-pressure test campaign, we compared the results to the Chapman-Jouguet (C-J) theoretical pressures and wave speeds using the online NASA chemical equilibrium analysis (CEA) tool for a detonation using hydrogen and oxygen.

The C-J theory predicts the theoretical wave speed and pressures of a one-dimension detonation wave, although the C-J predicted pressures are not the spike pressure. In order to predict the peak pressure, Jacob French, a pyrotechnical device design engineer at NASA Johnson, compared the results of both test campaigns to the theoretical maximum results calculated with the Von Neumann pressure spike, which predicts the maximum theoretical pressure at the front of the detonation across the shock wave. We expected that the measured values should exist somewhere between the Von Neumann pressure spike values and the C-J detonation pressure, as the instrumentation is not fast enough to capture the exact peak pressure, but it is fast enough to capture values close to the actual peak. Table 4.5 shows the resulting values. For Table 4.5, the chamber pressure and mixture ratio uncertainties are based off of the 0.25% Druck UNIK 5000 pressure transducer full scale accuracy, the high frequency pressure transducer uncertainty is based off of the 0.5% Kulite full scale accuracy, and the detonation wave speed uncertainty is calculated with Equation 5 at the two MHz recording rate

Table 4.5. Comparison between calculated and theoretical data for low and preliminary high speed test campaigns

Test #	Pc [psia]	O/F [-]	HF-PT-01 [psia]	HF-PT-02 [psia]	Detonation Wave Speed [m/s]	C-J Wave Speed [m/s]	C-J Pressure [psia]	von Neumann Pressure [psia]
LP_1	45 ± 5	6.1 ± 0.1	354 ± 100	1,853 ± 100	880 ± 62	3,130	960	1,662
LP_2	45 ± 5	8.2 ± 0.1	1,324 ± 100	1,400 ± 100	3,299 ± 857	2,877	961	1,662
LP_3	44 ± 5	8.0 ± 0.1	476 ± 100	2,034 ± 100	3,299 ± 857	2,897	940	1,625
LP_4	46 ± 5	10.2 ± 0.1	1,551 ± 100	1,220 ± 100	2,204 ± 383	2,697	971	1,678
LP_5	80 ± 5	6.3 ± 0.1	2,682 ± 100	1,492 ± 100	3,299 ± 857	3,135	1,741	3,091
LP_6	80 ± 5	8.5 ± 0.1	1,498 ± 100	1,946 ± 100	3,299 ± 857	2,877	1,739	3,012
LP_7	80 ± 5	10.3 ± 0.1	1,505 ± 100	1,553 ± 100	2,639 ± 550	2,715	1,716	2,973
HP_1	291 ± 5	8.1 ± 0.1	7,834 ± 100	-	-	2,984	6,601	11,481
HP_2	287 ± 5	8.0 ± 0.1	8,931 ± 100	5,984 ± 100	3,049 ± 46	2,994	6,511	11,323
HP_3	295 ± 5	8.0 ± 0.1	9,928 ± 100	8,484 ± 100	3,126 ± 49	2,996	6,698	11,649
HP_4	294 ± 5	6.1 ± 0.1	7,766 ± 100	8,616 ± 100	3,251 ± 54	3,231	6,644	11,574
HP_5	291 ± 5	9.9 ± 0.1	9,414 ± 100	9,032 ± 100	2,419 ± 29	2,808	7,238	11,327

The high-pressure test results in particular have good agreement with the expected C-J wave speed. The primary source of uncertainty in these measurements was the pressure transducers, which is an order of magnitude less in the high-pressure cases than the low-pressure cases. As the velocity is calculated from pressure spike to pressure spike, any delays in recording or variation in when the pressure transducers saw the pressure spike could lead to variation in the measurements. The low-pressure test results saw far more variation in the wave speed calculations. While the wave speed for these tests was calculated the same way, the C-J wave speed only considers detonation cases, while there were deflagration transformation cases during several of the low-pressure tests. The variation between the detonation and deflagration cases increased the differences between the theoretical and measured pressure and velocity values.

The high-pressure tests also saw good agreement with the theoretical pressures as all of the results above lie in between the C-J pressure curve and the von Neumann peak pressure values. In general, the high-pressure tests were centered in between the C-J and von Neumann values, indicating that the data gathered did not include the shock wave peak pressure but that the data gathered occurred almost instantaneously after the shock wave. There was far more variation between the low-pressure tests and the theoretical values. Once again, we expected this to be the result of the transformation between deflagration and detonation that occurred near the pressure transducers, altering the recorded peak pressures.

After these preliminary tests and after verifying full system functionality we moved on to the secondary high pressure test campaign with the goal of fully implementing the streak camera and attempting to capture spectroscopy data for chemiluminescence thermometry.

4.3 Secondary High Pressure Test Campaign

The secondary set of high-pressure tests consisted of two main goals: fully mapping the high-pressure profile that the shock tube was capable of creating and gather streak camera data for chemiluminescence spectroscopy. The streak camera data could then be analyzed to attempt to gather rotational temperature data of the intermediate combustion products, the width of the shock wave, and the velocity of the shock wave.

We used the same pressure transducer configuration as with the previous test setup. The majority of these test cases involved changing the driver pressure to determine how the shock characteristics changed. As such we varied the driver pressures between from 200 – 400 psia.

Additionally, mixture ratios were varied from six to ten to vary the wave speed. A table of all test cases for this portion of the testing is shown in Table 4.6 below.

Table 4.6. Secondary high pressure test campaign detonation conditions

Test Number	Chamber Pressure [psia]	Mixture Ratio [-]	HF-PT-01 [psia]	HF-PT-02 [psia]	Calculated Detonation Velocity [m/s]
HP_6	309 ± 5	10.2 ± 0.1	4,851* ± 100	4,729* ± 100	2862 ± 41
HP_7	387 ± 5	7.0 ± 0.1	7,344 ± 100	12,778 ± 100	3175 ± 50
HP_8	383 ± 5	7.8 ± 0.1	6,863 ± 100	12,327 ± 100	3079 ± 47
HP_9	300 ± 5	8.0 ± 0.1	5,853 ± 100	9,554 ± 100	3033 ± 46
HP_10	250 ± 5	6.6 ± 0.1	9,813 ± 100	8,073 ± 100	3200 ± 51
HP_11	256 ± 5	7.8 ± 0.1	9,460 ± 100	7,920 ± 100	3010 ± 46
HP_12	296 ± 5	8.0 ± 0.1	10,405 ± 100	9,031 ± 100	3033 ± 46
HP_13	257 ± 5	9.6 ± 0.1	9,282 ± 100	7,681 ± 100	2862 ± 41
HP_14	250 ± 5	6.1 ± 0.1	7,501 ± 100	7,615 ± 100	3251 ± 53
HP_15	197 ± 5	8.0 ± 0.1	7,396 ± 100	5,899 ± 100	2945 ± 43
HP_16	238 ± 5	7.9 ± 0.1	9,536 ± 100	6,796 ± 100	3056 ± 47
HP_17	245 ± 5	6.2 ± 0.1	9,728 ± 100	7,895 ± 100	3225 ± 52

We noted early on that the pressure transducers read extremely low peak pressures for test HP_6. After investigating the issue, we discovered that the soldered connection between the Kulite connectors and the Kulite signal conditioners were somewhat worn down. As such, we concluded that the peak pressures captured during that test likely did not match the actual values created in the shock tube. After making new connectors, HF-PT-02 responding as expected, however the magnitude of the HF-PT-01 still recorded pressure waves at magnitudes we were uncertain about. As the same Kulite pressure transducers have been used for all of the tests reported so far, we were somewhat concerned that HF-PT-01 may have taken a reflected shock at the wrong pressure, which was causing the observed fluctuations. Because of these fluctuations, the majority of the data

analysis was based on the HF-PT-02 data. As HF-PT-01 was still responsive in time, so both pressure transducers were still used to calculate the detonation wave speed.

Given the data in Table 6, we generated two plots: one comparing the driving chamber pressure to the measured pressure spike and the pressures predicted by Chapman-Jouguet, and one plot comparing the starting mixture ratio and the measured and theoretical estimated velocity. These plots are presented in Figures 4.13 and 4.14 respectively.

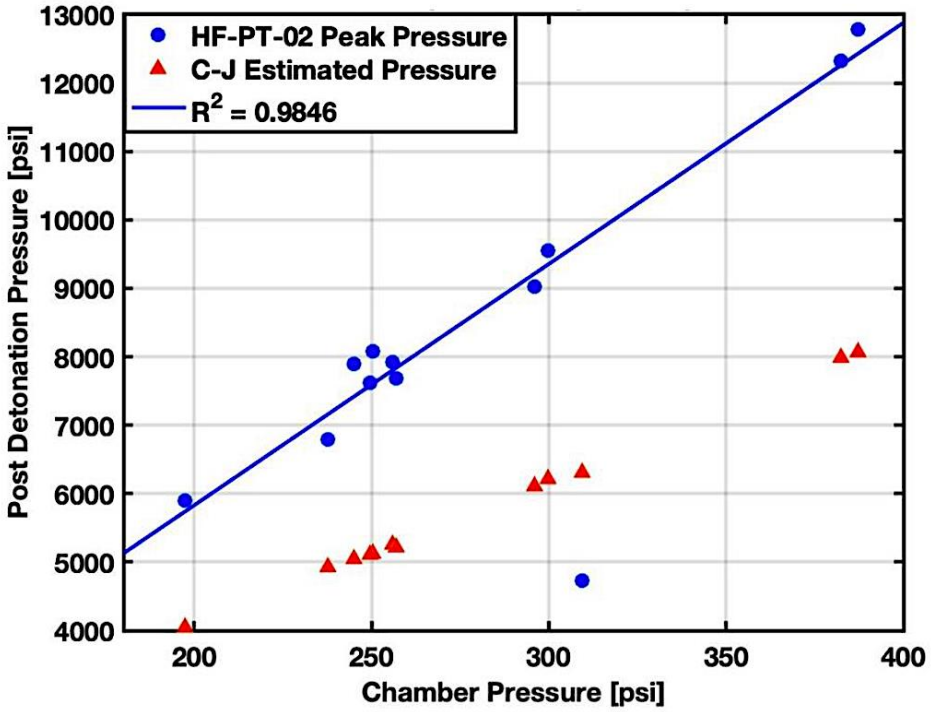

Figure 4.13: Measured detonation pressure spike plot compared to theoretical values

As shown in Figure 4.13, the pressure data recorded by HF-PT-02 is mostly linear. There are two points that strongly deviate from this trend, the first of which was that of HP_06, which, as mentioned, had issues with the pressure transducer scaling. As such, that point was not included when making the detonation model and calculating the R-squared value. Both the C-J theoretical values and the measured values were remarkably linear, with the measured peak pressures having an R-squared of 0.98. The recorded peak pressures were much higher than the C-J pressure, which once again made sense as the C-J pressure does not consider the actual spike pressure. There were some small variations in peak pressure due to the mixture ratio, however the chamber pressure of

the gases was the main indicator of the expected spike pressure. Given the linearity of the data, the expected peak pressure of any given test could be calculated using Equation 6.

$$Peak\ Pressure = 35.80 * (P_c) - 1264.2 \tag{6}$$

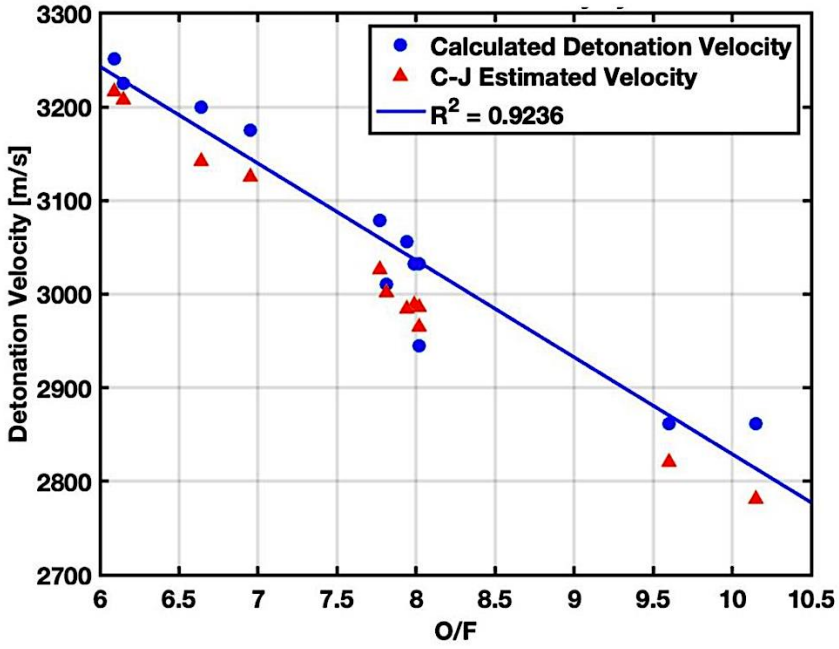

Figure 4.14: Calculated detonation velocity plot compared to theoretical values

While the peak pressure was primarily driven by the chamber pressure of the test article, the estimated wave speed was primarily influenced by the mixture ratio in the test article. Test numbers HP_8 and HP_15, which both had a mixture ratio close to 8 but were separated by almost 200 psia chamber pressure saw a difference of 134 m/s wave speed, which is significant. However, tests HP_10 and HP_11 had nearly the same chamber pressure at 250 psia, but had mixture ratios of 6.6 and 7.8 respectively and saw a 190 m/s difference in wave speed. As such, Figure 4.14 only shows the mixture ratio and detonation velocity. As the model above only considers the mixture ratio, the R-squared value is lower at 0.92, even though the data in Figure 4.14 still follows a mostly linear trend. The equation corresponding to this line is given in Equation 7.

$$Velocity = 35.8 * \left(\frac{O}{F}\right) - 1264.2 \tag{7}$$

There was good agreement with the calculated detonation velocity and the C-J estimated velocity. The majority of the calculated velocities were higher than the C-J velocities, however all of the calculated velocities were within 3% of the expected values. The high-speed pressure transducers were very useful for estimating the detonation velocities, and that even if the magnitude on the pressure transducer did not match the expected values, the responsiveness of the pressure transducers alone allowed for a good measurement of the wave speed within the detonation tube.

Additionally, during this part of the test campaign, the metal burst disks did not always rupture. When the chamber pressure of the system was above 300 psi, the burst disk always ruptured and saw all four brass petals detach and exit the tube. When the chamber pressure during a test was lower (250 psi), the burst disk always ruptured, but some of the brass petals would remain attached. During HP_15 – the lowest chamber pressure test – the burst disk deformed but did not rupture, leading to the reflective shock reverberating through the shock tube. We were concerned that a backwards moving, reflected shock wave was a risk to the hardware – most notably the spark plug and thermocouple that were not designed to take an 8,000-psi pressure wave – so all future tests had higher chamber pressures to ensure the burst disk burst. Figure 4.15 shows several of the burst disks in various configurations after detonation.

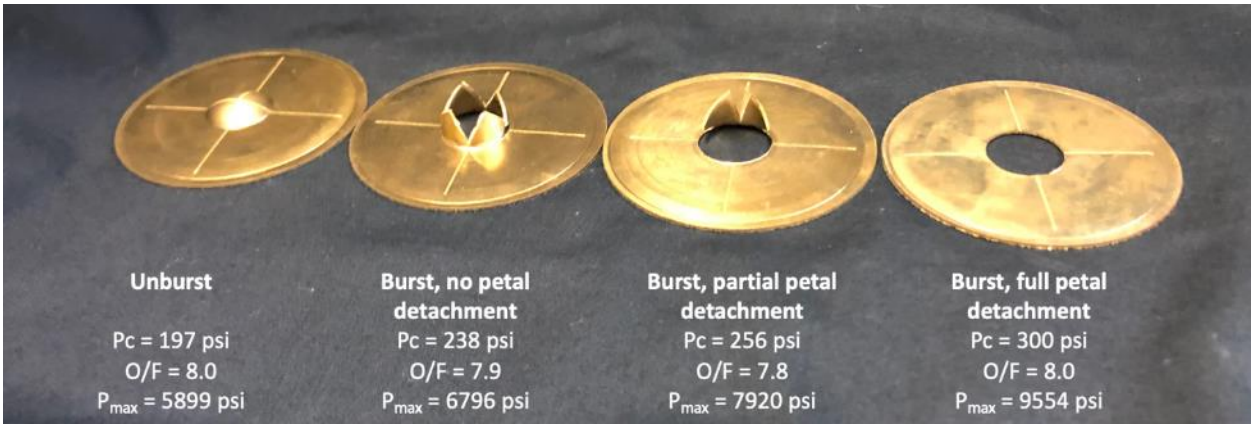

Figure 4.15: Differences in burst disk ruptures against driving chamber pressure

The final portion of the secondary high pressure test campaign involved integrating the streak camera by fiber optic cable to the optical port opposite of HF-PT-02 in order to gather spectroscopy data over brief time intervals. Initially the streak camera was set to a very low

exposure rate. While this limited the amount of light that was allowed to enter the system, the low exposure rate was used in order to protect the camera from the extremely bright shock wave. However, for the majority of the high-pressure tests during this test campaign the streak camera failed to take clear spectroscopic images due to this low exposure rate. We slowly increased the exposure rate throughout the test campaign in order to gather some usable data, however we only saw significant light lines for four tests on Table 4.6. The brightest image from high pressure test 14 is shown in Figure 4.16. For the associated image, the spectrometer had a slit size of 20 microns, a bandpass of 60 nanometers, and used a 1200 grooves/mm grating.

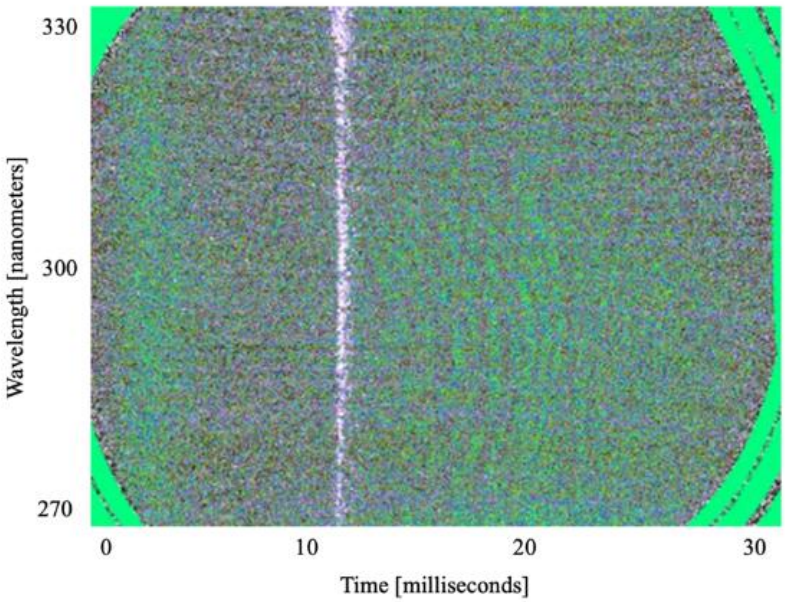

Figure 4.16: Raw Streak Camera image for HP_14

The bright white line that occurs at 11 milliseconds represents the passing of the shock wave, and the bright green coloration that immediately follows that white line is the passing of the detonation gases. Due to the high exposure rate, the data is incredibly noisy. It was very difficult to distinguish the noise from the OH* data at 308 nanometers. Figure 4.17 shows a horizontal slice taken from the data in Figure 4.16 at 308 nanometers. Any OH* after the initial rise and fall of the shock wave is indistinguishable from the noise in the system. The Sydor streak camera software has a built-in function for generating the horizontal lineout plots.

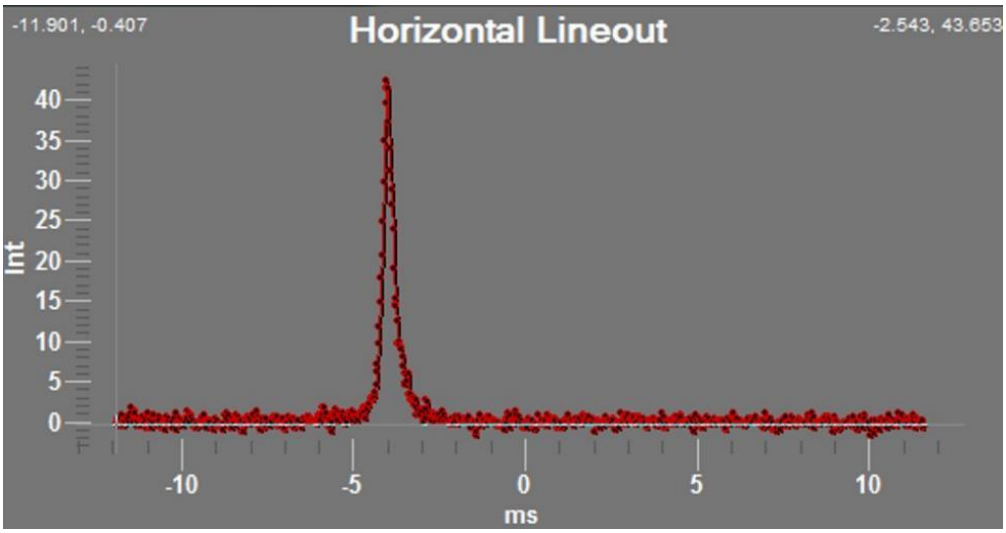

Figure 4.17: Horizontal lineout of the streak camera spectrometer intensities at 308 nanometers

The intensity of the shock wave itself is incredibly prominent, however any data on the intermediate combustion products that immediately follow the wave were not distinguishable from the noise. The x-axis shows the time duration of the streak camera recording. We used a sweep speed of 30 milliseconds, and the Sydor software plots this time duration from -15 milliseconds to +15 milliseconds. During our test campaign, we triggered the streak camera 10 milliseconds before we triggered the spark plug, so Figure 4.17 indicates that the shock tube ignited within 1 millisecond of the spark plug being triggered. This very short ignition delay was common throughout the majority of our testing.

Based on the timing data in Figure 4.17, we were able to compare the ignition delay reported by the streak camera to the ignition delay recorded by pressure transducers. The comparison between the two data sets allowed us to conclude that the streak camera recorded data when the detonation wave passed by the second pressure transducer (HF-PT-02), and that the light observed in Figure 4.16 was a direct result of the detonation wave and combustion products that followed the detonation wave passing by the optical probe. The comparison between the ignition delay from the streak camera and from the second Kulite pressure transducer is given in Table 4.7. The uncertainties on the above measurements for both the streak camera and the pressure transducer are based on the time duration of one data point. The ignition delay from the streak camera was calculated based on the first point the streak camera saw intense light based on the horizontal lineout, the internal delay, and experimental delay set during the autosequence. The

pressure transducer ignition delay was also calculated based on the autosequence delay, by comparing the spark time to the first instance of pressure rise.

Table 4.7. Ignition Delay Comparisons between the streak camera and pressure transducers

Test Number	Chamber Pressure [psia]	Mixture Ratio [-]	Ignition Delay from Streak Camera [ms]	Ignition Delay from PTs [ms]
HP_11	256 ± 5	7.8 ± 0.1	1.155 ± 0.05	1.1415 ± 0.0005
HP_12	296 ± 5	8.0 ± 0.1	1.006 ± 0.05	1.0697 ± 0.0005
HP_13	257 ± 5	9.6 ± 0.1	0.756 ± 0.05	0.8421 ± 0.0005
HP_14	250 ± 5	6.1 ± 0.1	1.903 ± 0.05	1.9346 ± 0.0005

The ignition delay between the streak camera and the pressure transducers generally agreed, indicating that the streak camera data record time corresponds to the pressure transducer data record time. For every test except HP_11 the streak camera recorded light slightly before the tangential second pressure transducer – HF-PT-02. As the timing does vary slightly, this indicated to us that there likely is some light scattering within the detonation tube that the streak camera recorded prior to the shock wave passing by the optical probe. The amount of light scattering also was likely aggravated by the high exposure time, as HP_11 (which had the lowest relative exposure) is the only test where the streak camera saw light after the pressure transducer.

Ultimately, we could not use this data to calculate the rotational temperature immediately following the shock wave. We attempted to calculate the rotational temperature within the shock wave, which is much easier to distinguish from the noise, however as can be observed in Figure 4.16, the shock wave comes up as a line across all of the measured wavelengths and any data from this image was not guaranteed to be OH*. As such, this data also could not be used for chemiluminescence thermometry.

We investigated why the exposure for the streak camera needed to be extremely high in order to get any data. The streak camera gathers light data through two optical fibers. While a single optical fiber would have been preferred, we used two to minimize potential damages to the fiber closest to the detonation tube. Coupling optical fibers can often lead to light losses, which could have caused data gathering issues. In order to investigate this, we took a small calibration

lamp and connected it to every possible point along the optical fibers, and determined how much of the light went through the cables to the streak camera.

Between the streak camera and the first optical fiber, we recovered an estimated 95% of the light from the calibration lamp. After coupling the first optical fiber to the more durable optical fiber, the light recovery was still about 90%. However, when the calibration lamp was connected to the fiber optic port that connected directly to the shock tube, we only saw a light recovery of 20-30%, which was an extremely high loss rate and was the cause of the exposure issues. There was no way to improve the light recovery after this point. Even after carefully cleaning the probe, we still had to greatly increase the exposure on the streak camera to capture Figure 4.16 above. We considered some other options to increase the streak camera signal, such as changing the streak camera grating and increasing the slit width on the spectrometer, however we ran out of time before we could implement these changes. We suspect that the sapphire window within the probe could not withstand the number of detonations that we used it for. Additionally, we prioritized robustness over light recovery, so new probes with a lens between the fiber and the sapphire window could provide more useful data. Either way, the probes on hand during this experiment had too much light loss to reliably gather data for gather chemiluminescence thermometry data to calculate the rotational temperature for this system.

The data from Figure 4.16 did however allow us to attempt to calculate the velocity of the shock wave. As the streak camera gathers data along the time axis, we could calculate the time duration that the streak camera recorded the shock wave for by comparing the number of pixels in the width of the white line at 308 nanometers in Figure 4.16 to the number of pixels in the entire image. Based on the machining specifications we knew the area and angle of view that the fiber optic probe records. From this, we have a distance and a time and can determine what velocity from the raw streak image. Equation 8 shows how we calculate the time duration of the detonation event from Figure 4.16, while Equation gives the full velocity calculation.

$$Time\ Duration = \frac{Shock\ Pixel\ Width\ (pixels)}{Image\ Pixel\ Width\ (pixels)} * 30\ ms \tag{8}$$

$$Velocity = \frac{Optical\ Probe\ Field\ of\ View\ (m)}{Time\ duration\ of\ the\ shock\ wave\ (ms)} \quad (9)$$

One early difficulty in Equation 9 was determining the field of view of the optical probe. While the probe comes in to the system in a fiber optic cable with a diameter of 0.032 inch, the optical probe expands this field of view to 0.125 inch – the interior diameter of a 3/16th inch HiP fitting – before the system sees the detonation gases. As such, the 0.125-inch final diameter was converted to meters for Equation 9 above, because that is the field of view the probe sees. The adaptor from fiber optic probe to the HiP fitting added an additional 1.5 inches of length to the fiber optic system, which furthers the optical probe from the shock wave and increased the uncertainty of these measurements. A summary of the data calculated using Equation 9 for HP_11, HP_12, HP_13, and HP_14 is given in Table 4.7.

However, it soon became apparent that we were not actually calculating the velocity of the shock wave. Based only on the thickness of the shock wave and the field of view, we calculated velocities that were far less than we expected. Instead, we were calculating the duration of the combustion event, on a microsecond time scale. Table 4.8 gives the combustion duration times and the estimated velocity from the streak camera data

Table 4.8. Velocity estimates from streak camera images compared to measured and theoretical velocities

Test Number	Chamber Pressure [psia]	Mixture Ratio [-]	Velocity from Streak Camera [m/s]	Velocity from PTs [m/s]	C-J Velocity [m/s]	Combustion Duration [μs]
HP_11	256 ± 5	7.8 ± 0.1	131 ± 44	3,010 ± 46	3,001	572 ± 22
HP_12	296 ± 5	8.0 ± 0.1	111 ± 36	3,033 ± 46	2,988	616 ± 22
HP_13	257 ± 5	9.6 ± 0.1	902 ± 29	2,862 ± 41	2,820	726 ± 22
HP_14	250 ± 5	6.1 ± 0.1	160 ± 54	3,251 ± 53	3,216	528 ± 22

As mentioned, the velocities from the streak camera appear far lower than we expected, and even with the proportionally high error bars we still do not see alignment with the pressure transducer measured values. The high error bars are due to the uncertainty in the pixel

measurement along the original image – the ± one pixel difference greatly affects the velocity due to the proportionally thin shock wave relative to the full image. Taking an image over a faster sweep speed could improve our uncertainty, however if the value does not align with what we expect the velocity measurement will not be very useful. Comparing the combustion duration to the ignition delay in Table 4.7 however, further indicates that the streak camera recorded data at the same time that the tangential pressure transducer recorded the detonation wave.

In general, the combustion duration follows the expected pattern, with the shortest combustion duration occurring at the lowest mixture ratio. The combustion duration also aligns with the high-pressure trace in Figure 4.9, which after oscillating saw 90% pressure decay in 700 microseconds. Knowing the decay from the pressure transducers, we can say that the streak camera can capture OH* immediately after the detonation until the detonation pressure has fallen to around 1,000 psia. As with the velocity calculations, the uncertainty on the streak camera measurements was ± one pixel, which equals 22 microseconds for the 30-millisecond sweep speed. If we were to go to a faster sweep speed, such as 10-millisecond, we would likely improve our uncertainty and potentially even capture some clear OH* data that we could use for chemiluminescence thermometry. The shock tube also reliably ignited the fuel and oxidizer gases within 5-milliseconds during all of the above tests, so a faster sweep speed could potentially gather more detailed data. However, we were not able to capture this data due to the timeline of the project and the limited amount of light that got from the shock tube to the streak camera. For any future projects using these systems, clearer fiber optic probes will be required, although the system itself appears to produce the desired data.

5. CONCLUSIONS

Hypersonic and re-entry vehicles experience extreme temperatures and pressures as they travel at extremely high velocities. It is important to understand the conditions any air or spacecraft will experience in order to properly design any propulsion or structural systems. However, at hypersonic speeds most probes and measuring devices will not survive the conditions of interest.

In this work, we primarily looked at non-invasive measurement techniques to capture the temperatures, velocities, and density gradients of high-speed, low-density flows. In order to model these specific flow conditions, we built a detonation driven shock tube, as the system is reliable, repeatable, and simple. In order to create the flows of interest, oxygen and hydrogen gases were combined within a 20,000-psi rated, stainless steel tube. The mixture was then ignited, and the gas quickly travelled down the length of the tube, bursting a burst disk and exiting out into the open air. Chemiluminescence thermometry and a streak camera were used in the shock tube to measure the rotational temperatures and wave speed velocities of detonation waves, while background oriented schlieren was used at the exit of the shock tube to measure density gradients of the detonation products. Additionally, two high pressure Kulite pressure transducers were placed at known locations along the shock tube to capture shock pressure data and velocity during each test.

The initial test matrix focused on investigating low chamber pressures within the shock tube in order to verify system functionality and test out several of the measurement techniques. The lowest chamber pressure tested – 45 psia – was somewhat problematic as the detonation wave often had not fully formed before it passed the first pressure transducer. The shift from deflagration to detonation led the recorded detonation wave velocity being shorter than theory would suggest. In order to improve the results, we raised the chamber pressure to 80 psia for the rest of the test matrix. The system functioned as expected however, and for the detonation cases we saw good agreement between the Kulite measured data and the theoretical pressures and wave speeds suggested by Chapman-Jouguet from the NASA CEA program.

We applied background oriented schlieren data taking to these early tests. While we saw some expected results – obvious changes in the density gradients behind the low and high mixture ratio cases and various chamber pressure cases – we ultimately determined that we could not continue using this technique. Background oriented schlieren needs a stable background, in our case a dot pattern, for the post processing to work. The dot pattern we used worked well for low

chamber pressure test cases, however the piece of paper we used to secure the dot pattern often came unattached at the higher chamber pressure test cases. Additionally, we could not always gather reliable data due to the brightness of the flame at the exit of the shock tube. The bright flame would wash out the background dot pattern during our experiments. Because the brightness we had no reference to calculate the density gradients with, and ultimately, we could not use BOS to measure the density gradients of the higher-pressure cases the way the system was arranged. Future testing using this system would need a good way to dim the brightness of the flame, or make it easier to see the background during testing.

Additionally, we took spectroscopy data for chemiluminescence thermometry during the low-pressure test campaign using a Stellarnet Black-Comet spectrometer. The Black-Comet spectrometer was much smaller than the streak camera and saw a broader range of wavelengths. However, the Black Comet only took one data point every 4 milliseconds at the fastest setting, so it only captured data at the OH* wavelength once out of six tests, and even during that test the OH* did not appear at high enough intensities to reliably calculate the rotational temperature. As such, all later test cases that gathered spectroscopy data used the streak camera.

After the low-pressure test campaign finished, we moved to higher driving pressures. The purpose of the initial high-pressure portion of the testing campaign was to verify system functionality and test the full capabilities of the Kulite pressure transducers. Between the low-pressure test campaign and the high-pressure test campaign the data acquisition system was upgraded so that the pressure transducers could capture data at 2,000,000 Hz during testing, as opposed to the 130,000 Hz that the system was previously capped at. The higher data recording rate improved the uncertainty on our peak pressure and velocity measurements and helped us better understand the system. The majority of the test cases had a chamber pressure of 300 psia and ranged in mixture ratio from six to ten. During the initial high chamber pressure portion of the test campaign the pressure transducers calculated wave speeds within 3% of the theoretical Chapman-Jouguet wave speed, and reliably read peak pressures in the system in between the theoretical Von Neumann spike pressure and the Chapman-Jouguet pressure, which is known to not be the peak pressure, as was expected. The velocity of the detonation wave was calculated by dividing the distance between both pressure transducers by the difference in time each transducer reacted, and the overall process was simple to automate for quick calculation of the system. With this

information, we concluded that the two Kulite pressure transducers a known distance apart could reliably be used to calculate both the wave speed and peak pressures of the system.

Finally, we connected the streak camera to the system for the secondary high pressure test campaign. The high-pressure test campaign considered chamber pressures between 200 – 400 psia and mixture ratios ranging from six to ten psi. During this portion of testing, we were able to reliably predict the shock peak pressure during our tests based on our fill pressure, and the wave speed during our tests based on the mixture ratio using the same Kulite pressure transducers as in the earlier test campaign.

We had some difficulty integrating the streak camera into the system. The high-pressure fiber optic probes that connected the streak camera to the shock tube were not able to transmit most of the light from the detonation wave to the streak camera. Because of limited amount of light the streak camera received, we only observed the shock wave with the streak camera when the light gain on the streak camera was incredibly high and nearly saturated. The high gain on the streak camera resulted in a significant amount of noise within the system that made it difficult to determine what peaks were a result of OH*, and as such we were not able to use chemiluminescence thermometry on the data we gathered to get temperature.

We also used the streak camera to attempt to calculate the shock wave velocity, but instead were only able to measure the entire ignition event duration, from the shock wave passing the streak camera to the expulsion of the majority of the hot, bright gases. The expulsion process took less than one millisecond, so we had difficulty gathering useful information from the very short duration spike due to the sweep speed time of 30 milliseconds. We did not have time to increase the sweep speed in order to get more detailed data of the combustion event due to time constraints on the project and the light loss through the fiber optic probe. However, if new probes are created with far lower light losses, the data generated in the detonation tube would be very useful for chemiluminescence thermometry.

In this thesis we examined several optical measurement techniques to measure the temperature, density gradient, and velocity of hypersonic flows. While background oriented schlieren provide density gradient data for low velocity flows, a more robust background would be required to test the system at the higher speed flows of interest. While the Black Comet spectrometer provided some intermediate combustion product data, detonations of this speed required a system with a higher temporal resolution. Finally, while the streak camera provided the

higher temporal resolution required for our analyses, the system did not function as well as expected due to high light losses on the fiber optic connection probes. New probes that specialized in low light losses would be needed to reliably calculate the rotational temperature from the streak camera data using chemiluminescence thermometry.

While none of the experimental optical measurement techniques functioned exactly as expected during these test campaigns, we still learned how to apply these systems to gather some data, and are aware of what needs to change to make the systems more effective for future uses. Additionally, two Kulite pressure transducers at a known distance apart provided excellent pressure and velocity information for the system, while requiring very little data processing to get the required information. While these systems are more fragile than preferred for these types of high-speed, low-density flows, they can still provide reliable information about the flow conditions of interest for design purposes.

Future work on projects similar to this one should focus on increasing the light the system provides to the streak camera. One way to do this would be to have multiple probes connecting the streak camera to the test apparatus. This would reduce the light required as the detonation wave and intermediate combustion products following the detonation wave would capture three instances of the detonation at known times, which could be compared to better understand the detonation properties. Additionally, if there are multiple probes and one has high light losses, the other probes may still recover additional light to provide useful data.

Additionally, we could also integrate other temperature measurement techniques into the same system created for this project. With the metal burst disks, we observe some copper emission in the flame coloration at the exit of the shock tube. Boron gives a visible emission at both 518 and 547 nm, both of which peaks have a high streak response. Spalding et al. [18] and Ao et al. [19] showed that the intensity of the ratio of the 518 and 547 nm boron peaks varied for temperatures between 2000 K and 2600 K. We could integrate a similar system at the exit of the shock tube by coating the burst disk with a monolayer of boron and recording streak camera data at the exterior of the system. This could be a secondary way to gather temperature data on the system.

Further modifications can also include making changes to the spectrometer setup by using a zero-order grating. This would let additional light into the system and could increase our data recovery. Additionally, using a flashbulb, the zero-order grating, and an interference filter could

help calibrate the streak camera response so we have a better idea of the data we are gathering. All of these methods could be applied to gather chemiluminescence thermometry data to calculate the temperature of these types of detonation events, allowing us to have a better idea of high temperature, high speed flow events.

APPENDIX A: TEST PROCEDURES

Purdue University - Zucrow Laboratories

ZL1 Test Cell

Shock Tube Test Procedures

Approval Block	Signature	Date
Originator		
Facility		
Responsible Professor		

Table of Contents

ACRONYMS

TC	Test Conductor: In charge of all aspects of the test. Directs test operations through use of the test procedures.
TOP	Test Operator: Performs all test stand related activities associated with loading propellants and pressurant gases. Receives instructions from the Test
DSO	Data System Operator: Responsible for the installation and operability of all instrumentation and controls consistent with the requirements for each test.
SAF	Site Safety: Responsible for insuring all test site safety equipment is in place and functioning properly. Is responsible for keeping the site clear of unauthorized personnel during test operations.

Step No.	Action By	Operation	Test A	Test B	Test C
		SECTION 1: PREPARE TEST CELL			
1.000	TOP	Remove glassware from test cell			
1.001	TOP	Remove any mass detonables from test cell			

1.002	TOP	Verify clear blast path				
1.003	TOP	Verify DAQ box closed				
1.004	TOP	Verify additional cabnets closed				
1.005	TOP	Turn on Kulite Amplifier				
1.006	DSO	Turn on chassis				
1.007	DSO	Remote to DAQ				
1.008	DSO	Reset chassis in max				
1.009	DSO	Run H2Lab_108A_Main.vi				
1.01	DSO	Load Control, DAQ, Autosequence config files (ST_XXXXX)				
1.011	DSO	Start acquiring data				
1.012	DSO	Open front panel (ShockTube_v2.vi)				
1.013	DSO	Turn DAQ control and instrumentation power on				
1.014	DSO	Verify all channels reading properly (perform disconnect checks only if the experiment was not the last one in use)				
		SECTION 2: MAIN N2 PANEL				
2.000	DSO	Turn 108a light to red				
2.001	DSO	Turn control room light to amber				
2.002	TOP	Verify ALL regs on N2 panel closed				
2.003	TOP	Check valve position				
2.004	TOP	Open MV-N2-00				
2.005	TOP	Load step down regulator to buffer tank, MR-N2-02 to 500 psig				
2.006	TOP	Load Pilot regulator, MR-N2-04 to 100 psig				
		SECTION 3: VALVE CHECKS				
3.000	DSO	VERIFY no pressure reported on ox pressure transducer, PT-OX-14				
3.001	DSO	VERIFY no pressure reported on fuel pressure transducer, PT-FU-04				
3.002	DSO	VERIFY no pressure reported on shock tube pressure transducer, PT-ST-22				
3.003	DSO	**Cycle** H2 panel vent, PV-H2-59				
3.004	DSO	**Cycle** H2 fill ISO, PV-H2-67				
3.005	DSO	**Cycle** H2 feed purge, PV-N2-68				
3.006	DSO	**OPEN** GOX vent, PV-GOX-83				
3.007	DSO	**Cycle** GOX main ISO, PV-GOX-44				
3.008	DSO	**CLOSE** GOX vent, PV-GOX-83				
3.009	DSO	**Cycle** GOX feed purge, PV-N2-49				
3.010	DSO	**Cycle** GOX fill ISO, PV-GOX-48				
3.011	DSO	VERIFY the ox run valve, PV-OX-12 actuates, final state closed				
3.012	DSO	VERIFY the ox purge valve, PV-N2-13 actuates, final state closed				
3.013	DSO	VERIFY the fuel run valve, PV-FU-02 actuates, final state closed				
3.014	DSO	VERIFY the fuel purge valve, PV-N2-03 actuates, final state closed				
3.015	DSO	VERIFY shock tube purge valve, PV-ST-20 actuates **(with PV-ST-20 OPEN, acquire zeroing data on PT-ST-22)**, final state closed				

3.016	DSO	VERIFY shock tube vacuum valve, PV-VAC-21 actuates, final state closed				
3.017	DSO	VERIFY fuel buffer purge valve, PV-FU-22 actuates, final state closed				
3.018	DSO	Toggle spark and listen for relay in spark control box				
3.019	TOP	Load fuel purge/ejector drive regulator, MR-N2-05 to 100 psig (this is for 80 psig flowing pressure @ venturi)				
3.020	TOP	Load ox purge regulator, MR-N2-03 to 110 psig				
3.021	TOP	Load H2 feed purge, MR-N2-85 to minimum pressure				
3.022	TOP	Load GOX feed purge, MR-N2-80 to minimum pressure (~200 psi)				
		SECTION 4: PRE-TEST CHECKLIST				
4.000	TOP	Open and secure outside doors				
4.001	TOP	Remove blue tape from shock tube firing end				
4.002	TOP	Secure burst disk - 192 in-lbs				
4.003	TOP	Veryify catch bucket secure				
4.004	TOP	Hang outdoor warning chains				
4.005	TOP	Verify outside doors secure				
4.006	DSO	Start test cell ventilation snorkels				
4.007	TOP	Verify fuel run valve, MV-FU-01, Open				
4.008	TOP	Verify ox run valve, MV-OX-11, Open				
4.009	TOP	Exit test cell				
		SECTION 5: TEST PREPARATION				
5.000	DSO	Start LOGGING (RECORDING) DATA on VI				
5.001	DSO	OPEN PV-VAC-21				
5.002	DSO	OPEN PV-ST-20				
5.003	DSO	OPEN PV-FU-02				
5.004	DSO	Close PV-ST-20				
5.005	DSO	Open PV-N2-03				
5.006	DSO	Close PV-N2-03				
5.007	DSO	Open PV-ST-20				
5.008	DSO	Repeat steps (5.004 - 5.007) in yellow 3** times				
5.009	DSO	Close PV-FU-02				
5.010	DSO	Open PV-OX-12				
5.011	DSO	Close PV-OX-12				
5.012	DSO	Close PV-ST-20				
5.013	DSO	Open PV-FU-22				
5.014	DSO	Close PV-FU-22				
5.015	DSO	Close PV-VAC-21				
5.016	TOP	Enter cell, **TAKING CAMERAS**				
5.017	TOP	Turn on test cell fans				
		OXYGEN				
5.018	DSO	**OPEN** GOx Iso Valve PV-GOX-44				

5.019	DSO	Verify GOx main regulator ER-GOX-45 **UNLOADED**				
5.020	TOP	Verify GOx igniter regulator MR-GOX-50 **UNLOADED**				
5.021	TOP	**SLOWLY OPEN** GOx bottle from outside				
		Hydrogen				
5.022	TOP	Verify H2 igniter regulator MR-H2-60 **UNLOADED**				
5.023	TOP	Verify H2 main regulator MR-H2-64 **UNLOADED**				
5.024	TOP	Verify H2 iso valve MV-H2-58 **CLOSED**				
5.025	TOP	Leave 108a				
5.026	TOP	Close Door				
5.027	TOP	Put up chain				
5.028	TOP	Setup and turn **ON** fume arm over hydrogen panel				
5.029	TOP	Verify H2 lab iso regulator MR-H2-00 **UNLOADED**				
5.030	DSO	Turn 110a light to RED				
5.031	TOP	**OPEN** H2 supply				
5.032	DSO	Verify H2 supply pressure PT-H2-84 value				
5.033	TOP	**OPEN** H2 iso valve MV-H2-58				
5.034	TOP	**LOAD** H2 supply regulator MR-H2-00 to 500 psia				
5.035	TOP	Come back to Control Room				
5.036	TOP	Load H2 reg, MR-H2-64 to desired test condition: _____ + 5 psi cracking pressure				
5.037	TOP	START RECORDING ON ANY IN CELL CAMERAS				
5.038	TOP	Plug in spark box power				
5.039	TOP	All personel EXIT test cell				
5.040	TOP	Secure cell door				
5.041	TOP	Hang do not cross chains to cell				
5.042	DSO	Open PV-VAC-21				
5.043	DSO	LOAD ER-GOX to _____ psi				
5.044	DSO	Open PV-GOX-48				
5.045	DSO	Close PV-ST-20				
5.046	DSO	Open PV-Ox-12				
5.047	DSO	Close PV-Ox-12				
5.048	DSO	Open PV-ST-20				
5.049	DSO	Close PV-ST-20				
5.050	DSO	Close PV-VAC-21				
5.051	DSO	Turn all warning lights to RED				
5.052	DSO	IF NEEDED Start Streak Camera				
5.053	DSO	NOTIFY surrounding lab groups of impending test				
5.054	TOP	VERIFY no persons outside				

		SECTION 6: OX AND FUEL LOADING AND FIRING				
6.000	DSO	VERIFY autosequence				
6.001	DSO	Open PV-OX-12				
6.002	DSO	Wait until PT-ST-22 reaches design pressure				
6.003	DSO	Close PV-OX-12				
6.004	DSO	VERIFY all personel in control room have hearing protection				
6.005	DSO	Open PV-H2-67				
6.006	DSO	Open PV-FU-02				
6.007	DSO	Close PV-FU-02 as quickly as possible after PT-ST-22 reaches equalibrium pressure				
6.008	DSO	Start timer				
6.009	DSO	Close PV-GOX-48				
6.010	DSO	Close PV-H2-67				
6.011	DSO	Open PV-VAC-21				
6.012	DSO	IF NEEDED Capture camera				
6.013	DSO	**ARM AUTO**				
6.014	DSO	**RUN AUTO**				
6.015	DSO	Verify integrity of stand and DACs functionality				
6.016	DSO	Stop and Start data recording				
		SECTION 7: SHOCK TUBE Safing				
7.000		**If detonation:**				
7.001	DSO	Close PV-ST-20				
7.002	DSO	Close PV-VAC-21				
7.003	DSO	After 30 seconds, Close PV-N2-03 and after 03 is closed, CLOSE PV-N2-13				
7.004		**If NO detonation:**				
7.005	DSO	Close PV-N2-03 and after 03 is closed, CLOSE PV-N2-13				
7.006	DSO	Cycle PV-N2-13 multiple times to dilute shock tube to a safe mixture				
7.007	DSO	Close PV-N2-13				
7.008	DSO	Close PV-ST-20				
7.009	DSO	Close PV-VAC-21				
		SECTION 8: H2 and GOX unloading				
8.000	TOP	**REENTER test cell**				
8.001	TOP	Unplug spark box				
8.002	TOP	Stop cameras				
8.003	TOP	Close MV-H2-58				
8.004	DSO	Close PV-GOX-44				
8.005	TOP	Leave Cell				
8.006	TOP	Close Door				
8.007	TOP	Put up warning chain				
8.008	DSO	Open PV-VAC-21				

8.009	DSO	Open PV-ST-20
8.010	DSO	Open PV-OX-12
8.011	DSO	Open PV-N2-13
8.012	DSO	Close PV-N2-13
8.013	DSO	Repeat steps 8.011 and 8.012 three times
8.014	DSO	Close PV-OX-12
8.015	DSO	Open PV-N2-13
8.016	DSO	Open PV-FU-02 (pulsing)
8.017	DSO	Close PV-N2-13
8.018	DSO	Open PV-N2-03
8.019	DSO	Close PV-N2-03
8.020	DSO	Repeat steps 8.016 and 8.017 three times
8.021	DSO	Close PV-FU-02
8.022	DSO	Close PV-ST-20
8.023	DSO	Open PV-FU-22
8.024	DSO	Close PV-FU-22
8.025	DSO	Open PV-N2-13
8.026	DSO	Open PV-N2-03
8.027	DSO	Close PV-N2-03
8.028	DSO	Close PV-N2-13
8.029	DSO	Close PV-VAC-21
8.030		If testing again
8.031	TOP	Attach new burst disk
8.032	DSO	Return to section 5
8.033		If Finished proceed to section 9
		SECTION 9: WRAP UP TESTING
9.000	DSO	Open PV-GOX-44
9.001	TOP	Open PV-H2-58
9.002	TOP	Close GOX Cylinder
9.003	TOP	Close H2 Supply
9.004	TOP	Unload MR-H2-00
9.005	TOP	Reload MR-H2-00 to minimum cracking pressure
9.006	TOP	Return to control room
9.007	DSO	Open PV-H2-59
9.008	DSO	Close PV-H2-59
9.009	DSO	Open PV-GOX-83
9.010	DSO	Close PV-GOX-83

9.011	DSO	Close PV-GOX-44				
9.012	DSO	Unload ER-GOX-45				
9.013	TOP	Unload MR-H2-00				
9.014	TOP	Unload MR-H2-64				
9.015	TOP	Close MV-H2-58				
9.016	TOP	Close MV-N2-00				
9.017	TOP	Exit test cell				
9.018	DSO	Open PV-VAC-21 until PT-N2-01 ~ 0 psi				
9.019	DSO	Close PV-VAC-21				
9.020	TOP	Reenter test cell				
9.021	TOP	Unload MR-N2-02				
9.022	TOP	Unload MR-N2-04				
9.023	TOP	Unload MR-N2-85				
9.024	TOP	Unload MR-N2-05				
9.025	TOP	Unload MR-N2-80				
9.026	TOP	Unload MR-N2-03				
9.027	TOP	Close outside doors				
9.028	DSO	Turn off test cell warning light				
9.029	TOP	Take down do not cross chains				
9.030	TOP	Close test cell exterior door				
9.031	TOP	Unplug Optics				
9.032	DSO	Turn off PT power				
9.033	DSO	Turn off HFPT Power				
9.034	DSO	Turn off Valve Power				
9.035	DSO	Turn off Chassis				
		SECTION 10: EMERGENCY PROCEDURES				
	IN CASE OF LEAK, FIRE, OR OTHER INCIDENT					
8	TOP	Test conductors will use their best judgment to determine the severity of the situation				
8	TOP	Click the Abort/SAFE button				
8	TOP	Regardless of the incident severity, the appropriate personnel will be notified by phone of the incident and will provide guidance for further action. Timothée Pourpoint: 765-463-1615 Scott Meyer: 765-426-8095				
		MEDICAL CARE INFORMATION				
		Purdue University Student Health Center				
		Phone: 765-494-1724				
		Location: Corner of University St. and Stadium Ave. (near ARMS/CIVIL/WTHR)				
		Hours: M-F 0800-2000 / Sa-Su 1000-1800 / Summer 0800-1700 M-F				
		Clarian Arnett Hospital				
		Phone: 765-448-8000				
		Location: 5164 McCarty Lane, Lafayette, IN 47905				

APPENDIX B: MACHINE DRAWINGS OF ALL PARTS

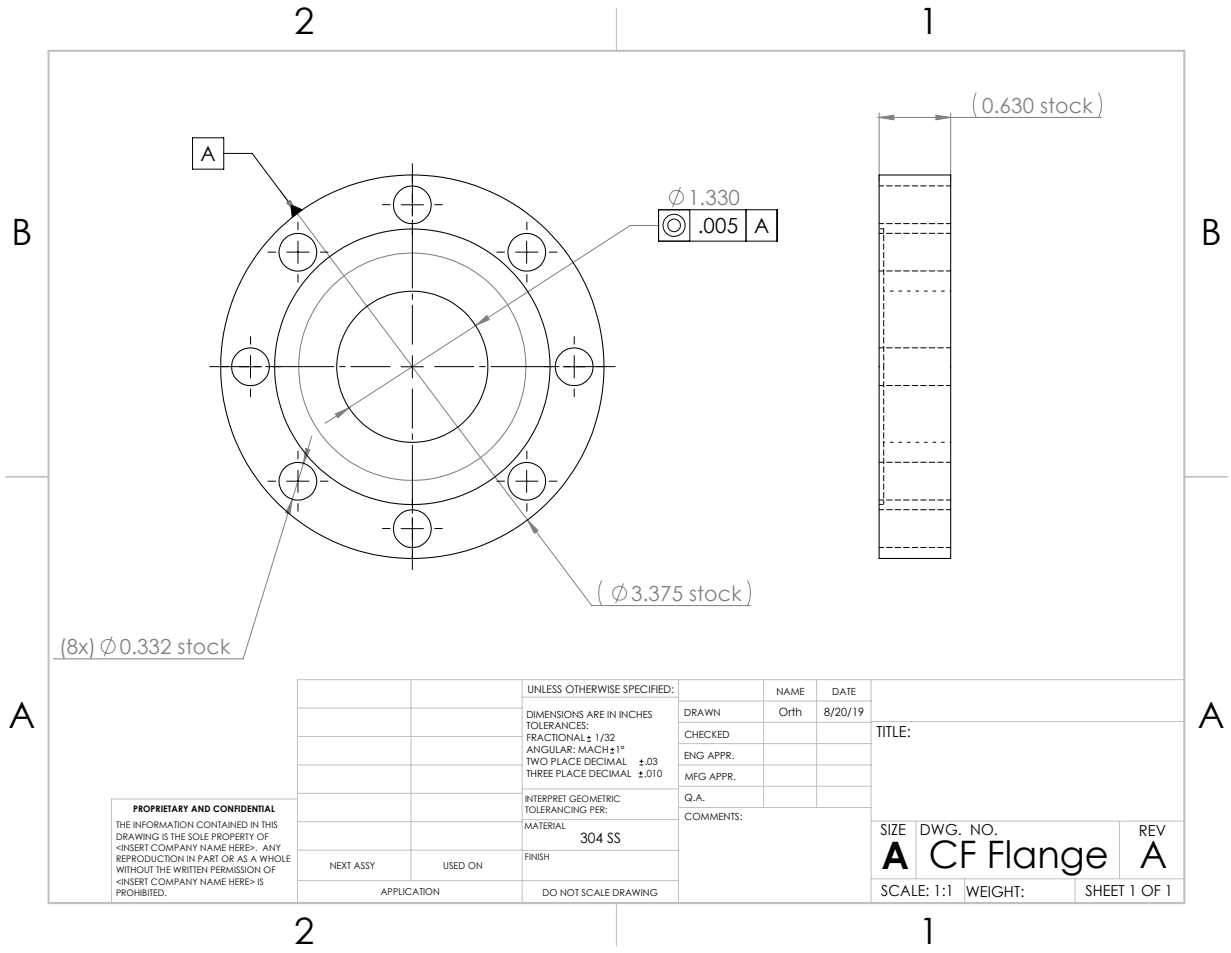

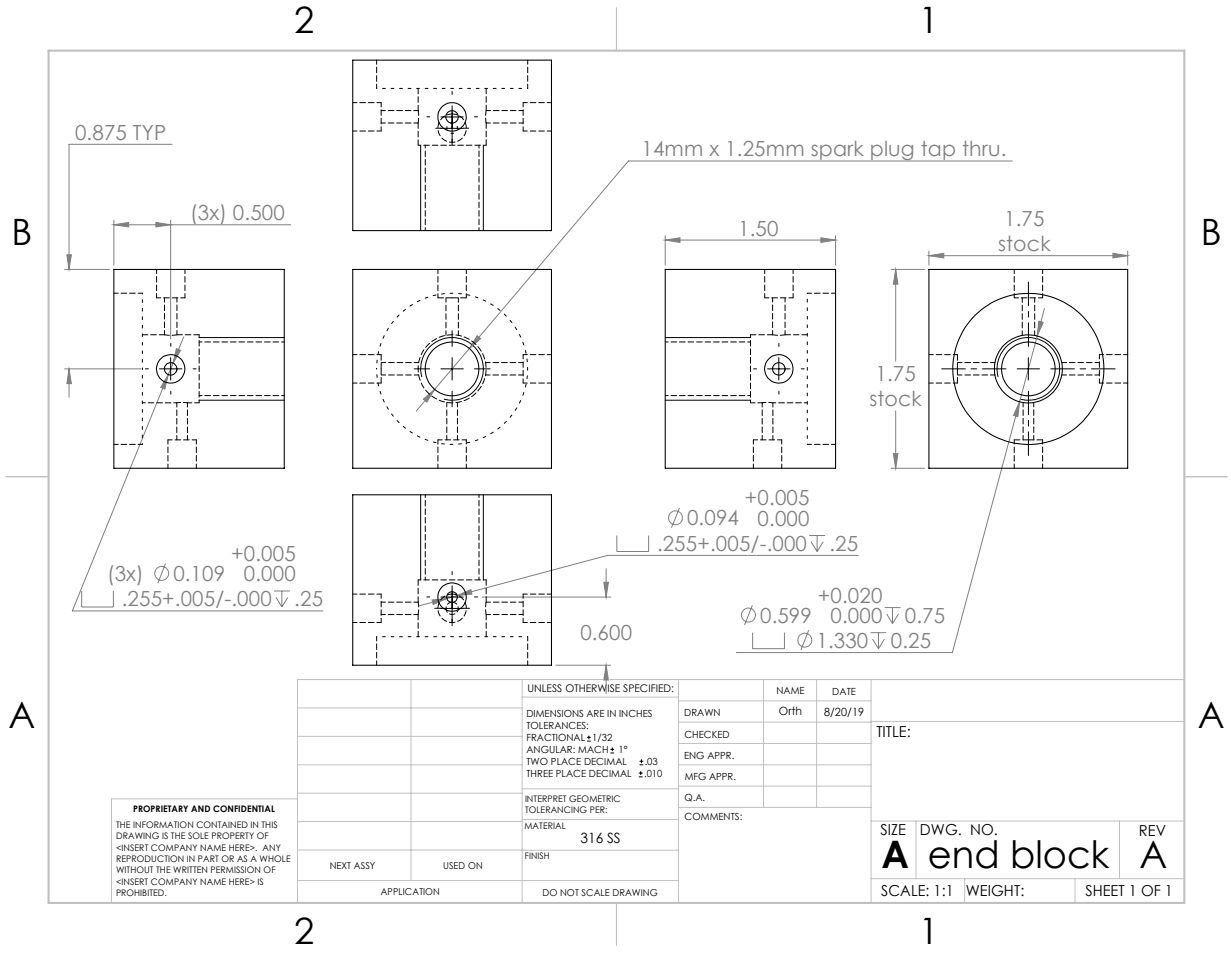
2
1
B
A
0.875 TYP
(3x) 0.500
14mm x 1.25mm spark plug tap thru.
1.50
1.75
stock
1.75
stock
+0.005
(3x) ∅0.109 0.000
.255+.005/-.000↧.25
+0.005
∅0.094 0.000
.255+.005/-.000↧.25
+0.020
∅0.599 0.000↧0.75
∅1.330↧0.25
0.600
PROPRIETARY AND CONFIDENTIAL
THE INFORMATION CONTAINED IN THIS DRAWING IS THE SOLE PROPERTY OF <INSERT COMPANY NAME HERE>. ANY REPRODUCTION IN PART OR AS A WHOLE WITHOUT THE WRITTEN PERMISSION OF <INSERT COMPANY NAME HERE> IS PROHIBITED.
NEXT ASSY
USED ON
APPLICATION
UNLESS OTHERWISE SPECIFIED:
DIMENSIONS ARE IN INCHES
TOLERANCES:
FRACTIONAL ±1/32
ANGULAR: MACH ± 1°
TWO PLACE DECIMAL ±.03
THREE PLACE DECIMAL ±.010
INTERPRET GEOMETRIC TOLERANCING PER:
MATERIAL
316 SS
FINISH
DO NOT SCALE DRAWING
NAME
DATE
DRAWN
Orth
8/20/19
CHECKED
ENG APPR.
MFG APPR.
Q.A.
COMMENTS:
TITLE:
SIZE
A
DWG. NO.
end block
REV
A
SCALE: 1:1
WEIGHT:
SHEET 1 OF 1

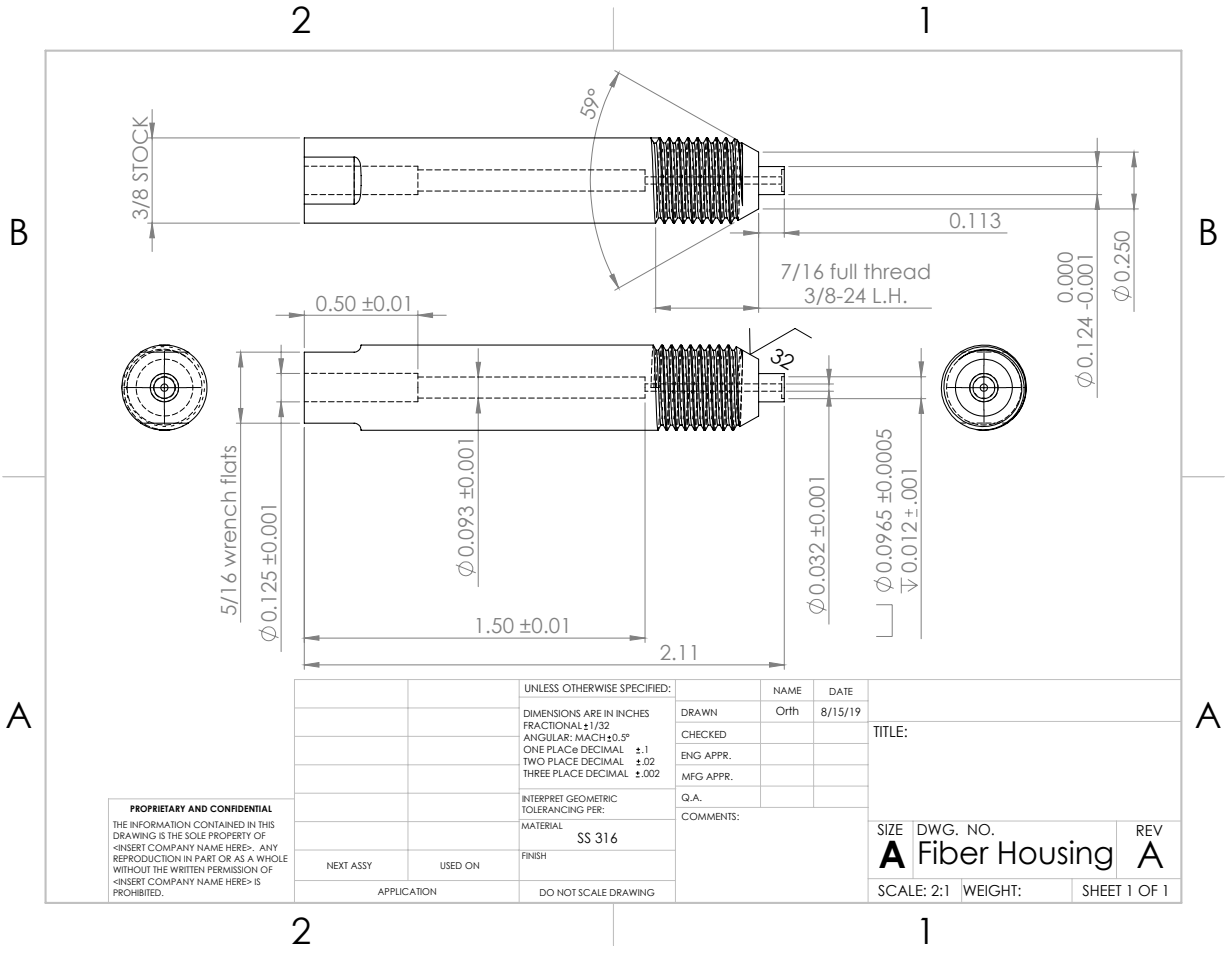
2
1
B
A
3/8 STOCK
59°
0.113
7/16 full thread
3/8-24 L.H.
0.000
-0.001
⌀0.250
⌀0.124
0.50 ±0.01
32
5/16 wrench flats
⌀0.125 ±0.001
⌀0.093 ±0.001
⌀0.032 ±0.001
⌀0.0965 ±0.0005
0.012 ±.001
1.50 ±0.01
2.11
UNLESS OTHERWISE SPECIFIED:
DIMENSIONS ARE IN INCHES
FRACTIONAL ±1/32
ANGULAR: MACH ±0.5°
ONE PLACE DECIMAL ±.1
TWO PLACE DECIMAL ±.02
THREE PLACE DECIMAL ±.002
INTERPRET GEOMETRIC TOLERANCING PER:
MATERIAL
SS 316
FINISH
NAME
DATE
DRAWN
Orth
8/15/19
CHECKED
ENG APPR.
MFG APPR.
Q.A.
COMMENTS:
TITLE:
SIZE
A
DWG. NO.
Fiber Housing
REV
A
SCALE: 2:1
WEIGHT:
SHEET 1 OF 1
NEXT ASSY
USED ON
APPLICATION
DO NOT SCALE DRAWING
PROPRIETARY AND CONFIDENTIAL
THE INFORMATION CONTAINED IN THIS DRAWING IS THE SOLE PROPERTY OF <INSERT COMPANY NAME HERE>. ANY REPRODUCTION IN PART OR AS A WHOLE WITHOUT THE WRITTEN PERMISSION OF <INSERT COMPANY NAME HERE> IS PROHIBITED.

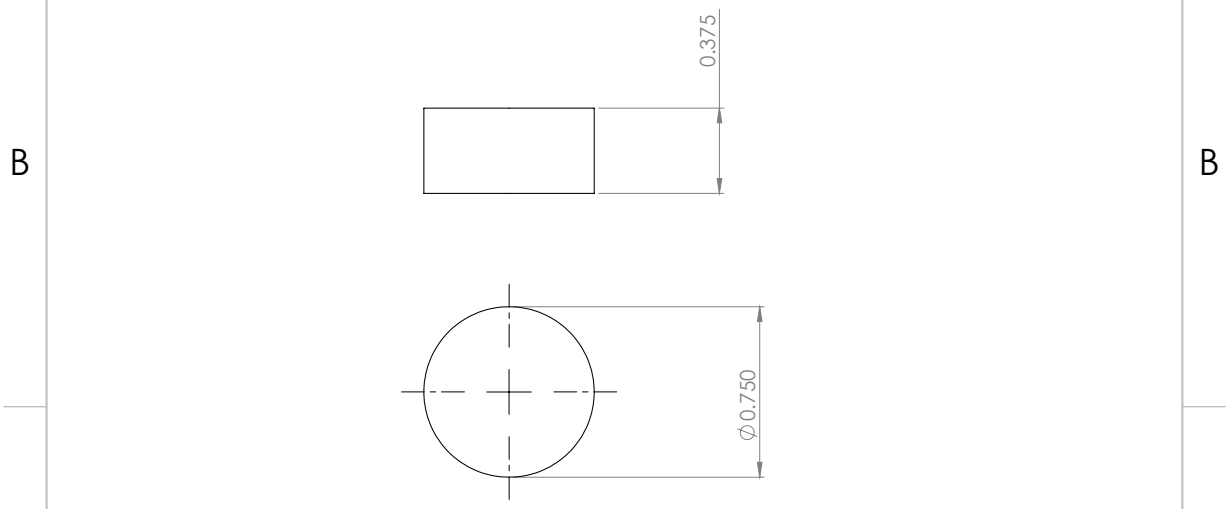

		UNLESS OTHERWISE SPECIFIED:		NAME	DATE
		DIMENSIONS ARE IN INCHES TOLERANCES: FRACTIONAL ± 1/32 ANGULAR: MACH ± 1° TWO PLACE DECIMAL ±.03 THREE PLACE DECIMAL ±.010	DRAWN	Orth	8/20/19
			CHECKED		
			ENG APPR.		
			MFG APPR.		
		INTERPRET GEOMETRIC TOLERANCING PER:	Q.A.		
		MATERIAL 316 SS	COMMENTS:		
NEXT ASSY	USED ON	FINISH			
APPLICATION		DO NOT SCALE DRAWING			

PROPRIETARY AND CONFIDENTIAL

THE INFORMATION CONTAINED IN THIS DRAWING IS THE SOLE PROPERTY OF <INSERT COMPANY NAME HERE>. ANY REPRODUCTION IN PART OR AS A WHOLE WITHOUT THE WRITTEN PERMISSION OF <INSERT COMPANY NAME HERE> IS PROHIBITED.

TITLE:

SIZE	DWG. NO.	REV
A	Kulite mount	A
SCALE: 2:1	WEIGHT:	SHEET 1 OF 1

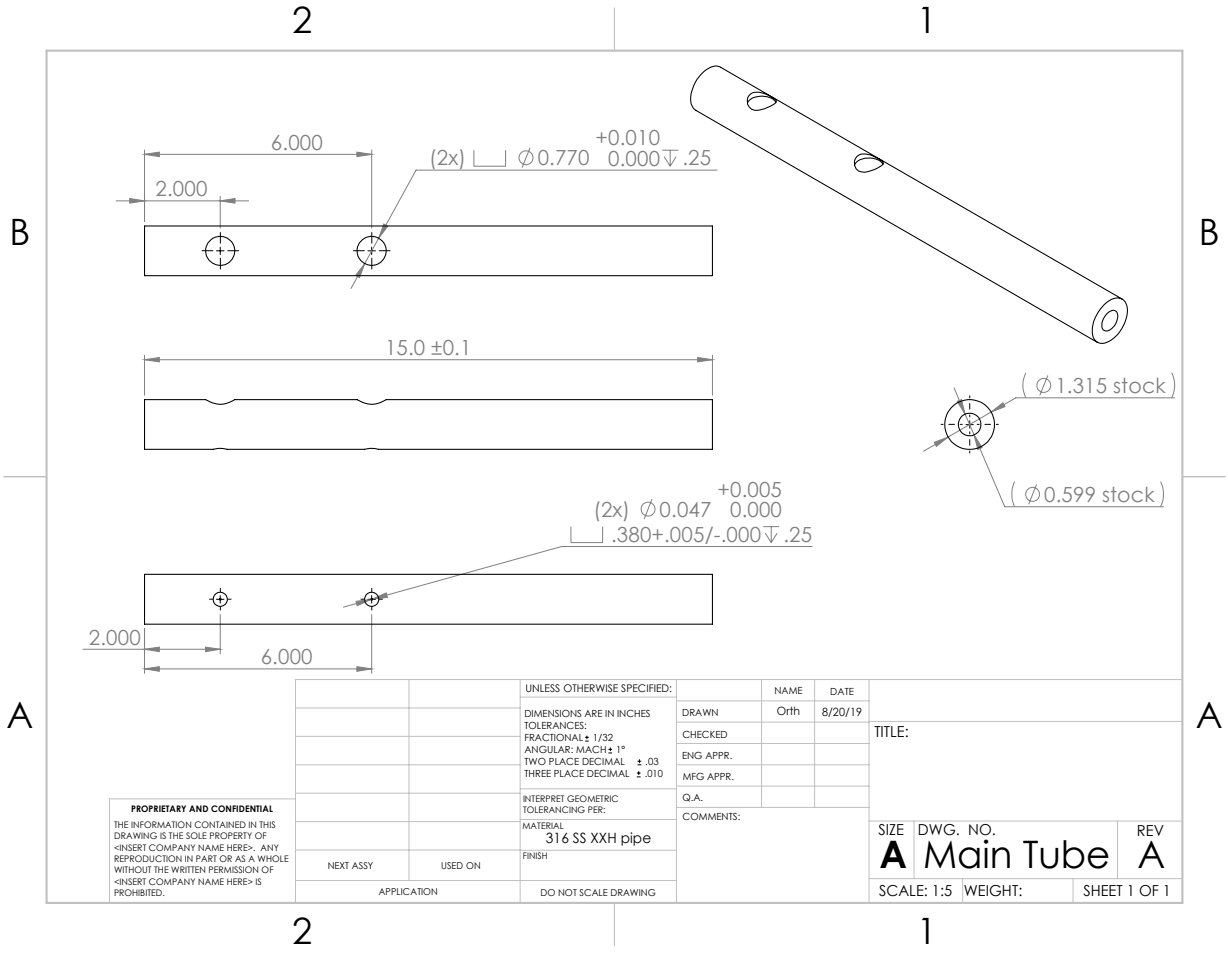
2
1
B
A
6.000
2.000
+0.010
(2x) ⌴ ∅0.770 0.000↧.25
15.0 ±0.1
(∅1.315 stock)
(∅0.599 stock)
+0.005
(2x) ∅0.047 0.000
⌴ .380+.005/-.000↧.25
2.000
6.000
UNLESS OTHERWISE SPECIFIED:
DIMENSIONS ARE IN INCHES
TOLERANCES:
FRACTIONAL ± 1/32
ANGULAR: MACH ± 1°
TWO PLACE DECIMAL ± .03
THREE PLACE DECIMAL ± .010
INTERPRET GEOMETRIC TOLERANCING PER:
MATERIAL
316 SS XXH pipe
FINISH
NEXT ASSY
USED ON
APPLICATION
DO NOT SCALE DRAWING
NAME
DATE
DRAWN
Orth
8/20/19
CHECKED
ENG APPR.
MFG APPR.
Q.A.
COMMENTS:
TITLE:
SIZE
A
DWG. NO.
Main Tube
REV
A
SCALE: 1:5
WEIGHT:
SHEET 1 OF 1
PROPRIETARY AND CONFIDENTIAL
THE INFORMATION CONTAINED IN THIS DRAWING IS THE SOLE PROPERTY OF <INSERT COMPANY NAME HERE>. ANY REPRODUCTION IN PART OR AS A WHOLE WITHOUT THE WRITTEN PERMISSION OF <INSERT COMPANY NAME HERE> IS PROHIBITED.

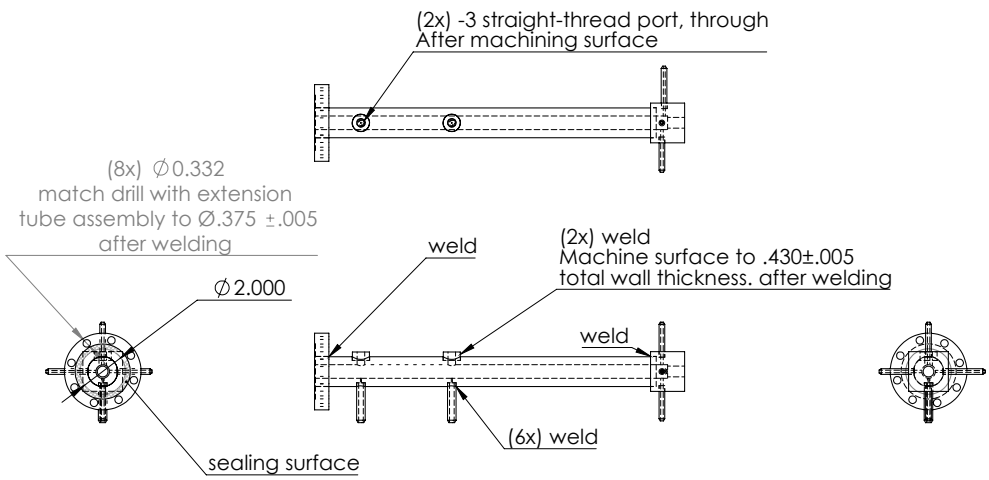

		UNLESS OTHERWISE SPECIFIED:		NAME	DATE	
		DIMENSIONS ARE IN INCHES TOLERANCES: FRACTIONAL ± 1/32 ANGULAR: MACH ± 1° TWO PLACE DECIMAL ± .03 THREE PLACE DECIMAL ± .010	DRAWN	Orth	8/27/19	TITLE:
			CHECKED			
			ENG APPR.			
			MFG APPR.			
		INTERPRET GEOMETRIC TOLERANCING PER:	Q.A.			
		MATERIAL	COMMENTS:			SIZE DWG. NO. REV
NEXT ASSY	USED ON	FINISH				A Main Tube Assy A
APPLICATION		DO NOT SCALE DRAWING				SCALE: 1:5 WEIGHT: SHEET 1 OF 2

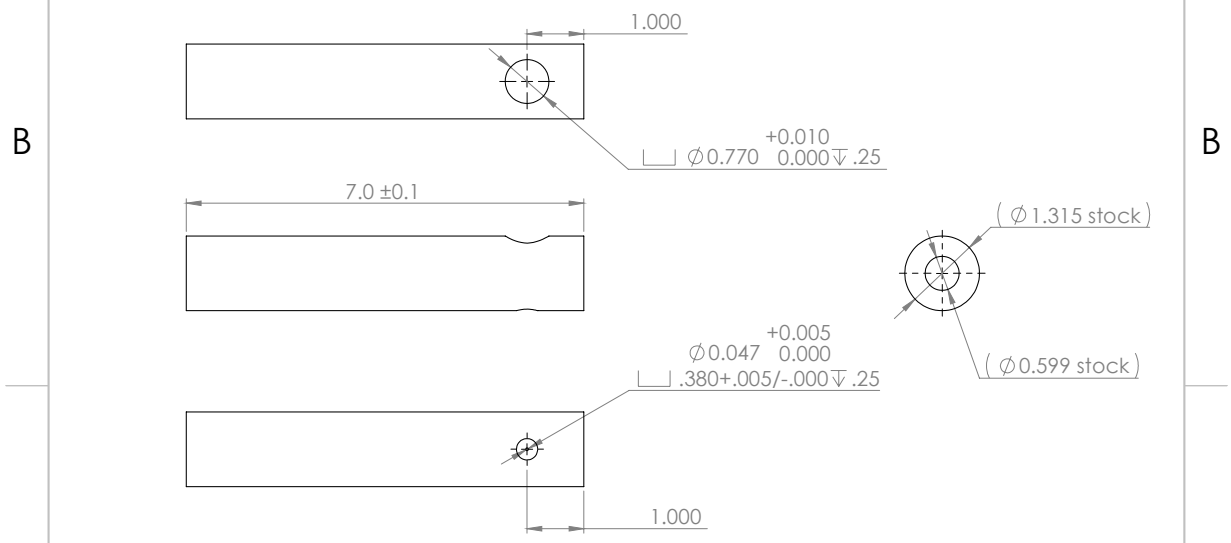

		UNLESS OTHERWISE SPECIFIED:		NAME	DATE
		DIMENSIONS ARE IN INCHES TOLERANCES: FRACTIONAL ± 1/32 ANGULAR: MACH ± 1° TWO PLACE DECIMAL ± .03 THREE PLACE DECIMAL ± .010	DRAWN	Orth	8/27/19
			CHECKED		
			ENG APPR.		
			MFG APPR.		
		INTERPRET GEOMETRIC TOLERANCING PER:	Q.A.		
		MATERIAL 316 SS XXH pipe	COMMENTS:		
NEXT ASSY	USED ON	FINISH			
APPLICATION		DO NOT SCALE DRAWING			

TITLE:

SIZE	DWG. NO.	REV
A	Extension Tube	A
SCALE: 1:2	WEIGHT:	SHEET 1 OF 1

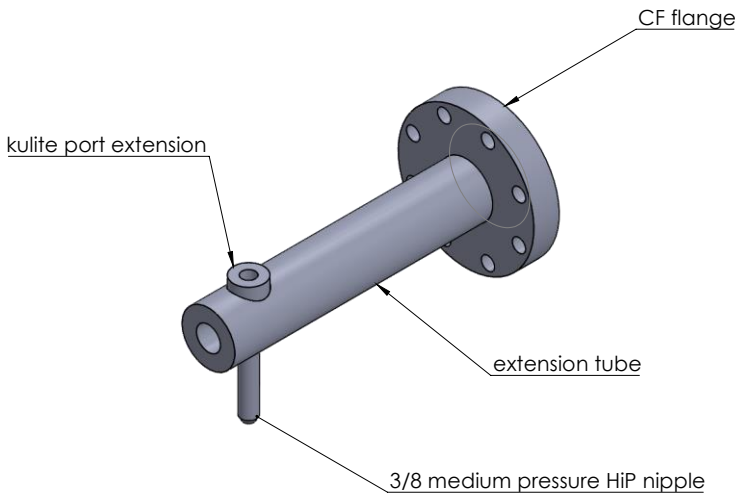

		UNLESS OTHERWISE SPECIFIED:		NAME	DATE
		DIMENSIONS ARE IN INCHES TOLERANCES: FRACTIONAL ± ANGULAR: MACH ± BEND ± TWO PLACE DECIMAL ± THREE PLACE DECIMAL ±	DRAWN	Orth	8/27/19
			CHECKED		
			ENG APPR.		
			MFG APPR.		
		INTERPRET GEOMETRIC TOLERANCING PER:	Q.A.		
		MATERIAL	COMMENTS:		
NEXT ASSY	USED ON	FINISH			
APPLICATION		DO NOT SCALE DRAWING			

TITLE:

SIZE	DWG. NO.	REV
A	Extension Tube Assy	
SCALE: 1:5	WEIGHT:	SHEET 1 OF 2

APPENDIX C: DATA SHEETS

Princeton Instruments

SPECTROSCOPY GROUP

Acton Series Monochromators and Spectrographs

The Acton Series of imaging spectrographs and monochromators from Princeton Instruments are the industry standard for researchers who demand the highest quality data. Acton monochromators and spectrographs feature a rugged yet flexible design that can be configured for a wide range of applications.

FEATURE	BENEFITS
Positrak™ grating stabilization	Quickly change gratings to accurately center on your desired wavelength
Image corrected optics	Offers the best spatial resolution for multi-stripe spectroscopy. Toroidal mirrors provide excellent imaging quality and enhanced spatial and spectral resolution.
High efficiency optical coatings	Acton #1900 Al + MgF_2 coating delivers the highest throughput in the industry, guaranteeing 85% reflectance from 200 - 700 nm. Optional protected silver, gold or dielectric coatings are available. See page 4.
Multiple entrance and exit ports	Can accommodate multiple detectors and experiments
Accessories	Including fiber adapters, filter wheels, sample chambers, shutters and light sources
Available in four focal lengths	150 mm, 300 mm, 500 mm and 750 mm to meet a variety of resolution requirements
Optional WinSpec, SpectraSense or LightField software	Complete data acquisition software for both CCD and single point detectors
Optional Scientific Toolkit (SITK)™ for LabVIEW®	Expert tool kit for programming Labview to control Acton Series spectrometers

Exit Configurations - Acton Series

SP 2X55 - SP2X60 Models	Exit Configurations
SP 2X55	Front exit slit
SP 2X56	Front exit camera port
SP 2X57 *	Front and side exit slits
SP 2X58 *	Front exit camera port and side exit slit
SP 2X60 * †	Front and side exit camera ports

LightField

Powered by LightField®

* These models not available in 150 mm focal length.

† SP 2X60 side exit slit focal plane width is limited to 19 mm.

Applications:
Raman, LIBS, Transmission, Reflectance, Luminescence, Absorption

Princeton Instruments
SPECTROSCOPY GROUP

Acton Series Specifications

	SP2150	SP2300	SP2500	SP2750
Focal length	150 mm	300 mm	500 mm	750 mm
Aperture ratio	f/4.0	f/3.9	f/6.5	f/9.7
Scan range (with 1200 G/mm grating)	0 - 1400 nm mechanical range	0 - 1400 nm mechanical range	0 - 1400 nm mechanical range	0 - 1400 nm mechanical range
Linear dispersion * (@ 435.833 nm)	4.17 nm/mm	2.38 nm/mm	1.52 nm/mm	1.03 nm/mm
CCD resolution ** (20 µm pixel, 20 µm slit width)	0.4 nm	0.14 nm	0.09 nm	0.06 nm
PMT resolution * (10 µm slit width)	0.4 nm	0.1 nm	0.05 nm	0.03 nm
Wavelength coverage (across 26.8 mm CCD)	111 nm	64 nm	41 nm	27 nm
Grating size	32 x 32 mm	68 x 68 mm 68 x 84 (optional)	68 x 68 mm 68 x 84 (optional)	68 x 68 mm
Grating mount	Interchangeable dual grating turret	Interchangeable triple grating turret	Interchangeable triple grating turret	Interchangeable triple grating turret
Focal plane size (front exit port)	25 mm wide x 10 mm high	27 mm wide x 14 mm high	27 mm wide x 14 mm high	25 mm wide x 14mm high
Astigmatism (at focal plane edges)	690 µm	720 µm	250 - 300 µm	150 - 175 µm
Standard Series manual slits (micrometer adjustable)	10 µm to 3mm manual	10 µm to 3mm manual	10 µm to 3mm manual	10 µm to 3mm manual
Wavelength accuracy	± 0.25 nm	± 0.2 nm	± 0.2 nm	± 0.1 nm
Repeatability	± 0.05 nm	± 0.05 nm	± 0.05 nm	± 0.05 nm
Drive step size	0.005 nm	0.005 nm	0.005 nm	0.005 nm
Size	7 in (178 mm) long 7 in (178 mm) wide 6.5 in (165 mm) high	13.2 in (337 mm) long 10 in (254 mm) wide 8 in (203 mm) high	21 in (534 mm) long 11 in (280 mm) wide 8 in (203 mm) high	30 in (762 mm) long 11 in (280 mm) wide 8 in (203 mm) high
Optical axis height	4 in (102 mm)	4.875 in (124 mm)	4.875 in (124 mm)	4.875 in (124 mm)
Weight	10 lbs (4.5 kg)	35 lbs (15.9 kg)	40 lbs (18 kg)	45 lbs (20.5 kg)
Computer interface	USB and RS232	USB and RS232	USB and RS232	USB and RS232

* Linear dispersion measured with a 1200 g/mm grating @ 435.8 nm.
PMT resolution measured with a 1200 g/mm grating @ 435.8 nm,10 µm slit width and 4 mm slit height.

** CCD resolution measured with a 1200 g/mm grating @ 435.8 nm, 20 µm slit width and 20 µm pixel.

Princeton Instruments
SPECTROSCOPY GROUP

Grating Curves

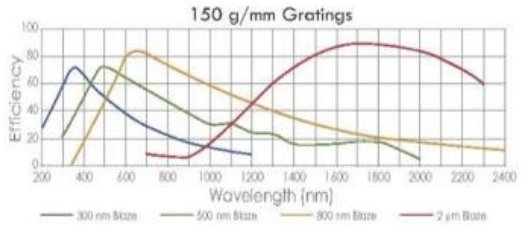

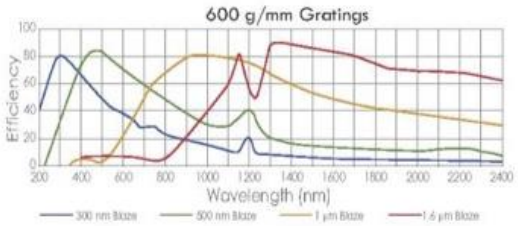

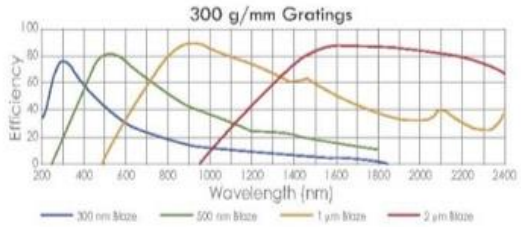

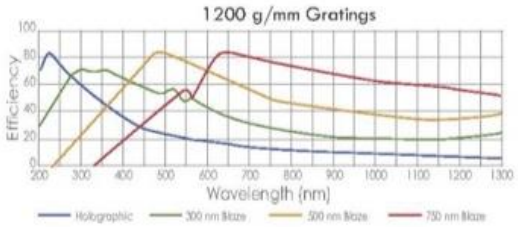

Dispersion and Wavelength Coverage (26.8 mm focal plane)

Model	150 g/mm	300 g/mm	600 g/mm	1200 g/mm	1800 g/mm	2400 g/mm	3600 g/mm*
SP-2150i	39.7 nm/mm 1064 nm	19.5 nm/mm 522 nm	9.33 nm/mm 250 nm	4.17 nm/mm 111 nm	2.37 nm/mm 63 nm	1.4 nm/mm 37 nm	1.07 nm/mm 28.6 nm
SP-2300i	21.2 nm/mm 569 nm	10.5 nm/mm 281 nm	5.12 nm/mm 137 nm	2.38 nm/mm 64 nm	1.44 nm/mm 38 nm	0.93 nm/mm 25 nm	0.67 nm/mm 18 nm
SP-2500i	13.1 nm/mm 351 nm	6.5 nm/mm 174 nm	3.2 nm/mm 85 nm	1.52 nm/mm 41 nm	0.94 nm/mm 25 nm	0.63 nm/mm 17 nm	0.45 nm/mm 12 nm
SP-2750	8.8 nm/mm 235 nm	4.37 nm/mm 117 nm	2.16 nm/mm 57 nm	1.03 nm/mm 27 nm	0.64 nm/mm 17 nm	0.44 nm/mm 11.7 nm	0.31 nm/mm 8.2 nm

* Center wavelength of 253.65 nm used with 3600 g/mm grating. Center wavelength of 435.8 nm used with all other gratings.

Princeton Instruments
SPECTROSCOPY GROUP

Grating Curves

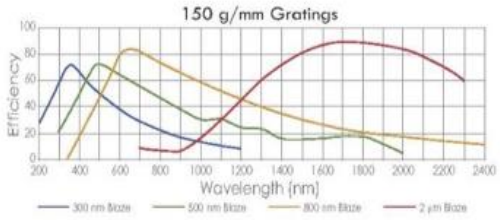

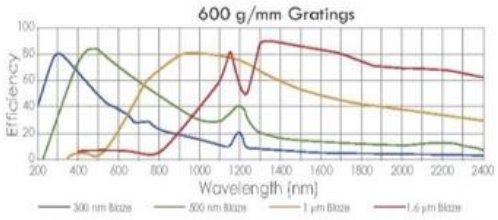

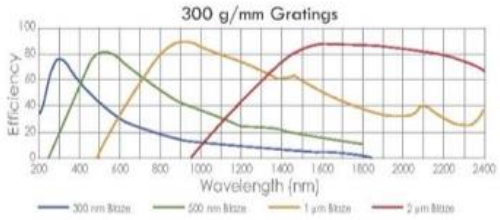

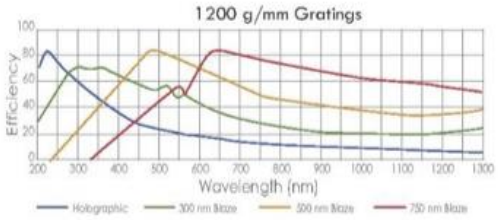

Dispersion and Wavelength Coverage (26.8 mm focal plane)

Model	150 g/mm	300 g/mm	600 g/mm	1200 g/mm	1800 g/mm	2400 g/mm	3600 g/mm*
SP-2150i	39.7 nm/mm 1064 nm	19.5 nm/mm 522 nm	9.33 nm/mm 250 nm	4.17 nm/mm 111 nm	2.37 nm/mm 63 nm	1.4 nm/mm 37 nm	1.07 nm/mm 28.6 nm
SP-2300i	21.2 nm/mm 569 nm	10.5 nm/mm 281 nm	5.12 nm/mm 137 nm	2.38 nm/mm 64 nm	1.44 nm/mm 38 nm	0.93 nm/mm 25 nm	0.67 nm/mm 18 nm
SP-2500i	13.1 nm/mm 351 nm	6.5 nm/mm 174 nm	3.2 nm/mm 85 nm	1.52 nm/mm 41 nm	0.94 nm/mm 25 nm	0.63 nm/mm 17 nm	0.45 nm/mm 12 nm
SP-2750	8.8 nm/mm 235 nm	4.37 nm/mm 117 nm	2.16 nm/mm 57 nm	1.03 nm/mm 27 nm	0.64 nm/mm 17 nm	0.44 nm/mm 11.7 nm	0.31 nm/mm 8.2 nm

* Center wavelength of 253.65 nm used with 3600 g/mm grating. Center wavelength of 435.8 nm used with all other gratings.

Princeton Instruments
SPECTROSCOPY GROUP

2300i Models (300 mm focal length)

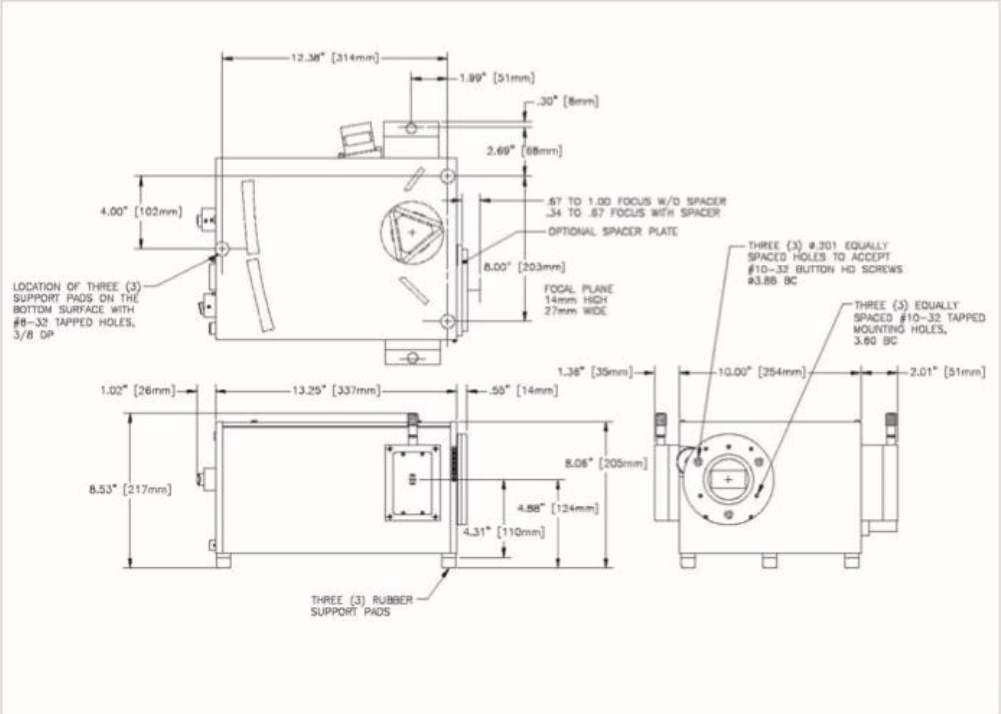

Model	Function	Port Configuration	Optical Path
SP 2355	Monochromator	Side Entrance Slit/Front Exit Slit	90°
SP 2356	Spectrograph	Side Entrance Slit/Front CCD Port	90°
SP 2357	Monochromator	Side Entrance Slit/Front Exit Slit/Side Exit Slit	90° and 180°
SP 2358	Spectrograph	Side Entrance Slit/Front CCD Port/Side Exit Slit	90° and 180°
SP 2360	Spectrograph	Side Entrance Slit/Front CCD Port/Side CCD Port	90° and 180°

Optional motorized slits are available. Contact your sales rep for more information.

Princeton Instruments
SPECTROSCOPY GROUP

Acton Series Specifications

	SP2150	SP2300	SP2500	SP2750
Focal length	150 mm	300 mm	500 mm	750 mm
Aperture ratio	f/4.0	f/3.9	f/6.5	f/9.7
Scan range (with 1200 G/mm grating)	0 - 1400 nm mechanical range	0 - 1400 nm mechanical range	0 - 1400 nm mechanical range	0 - 1400 nm mechanical range
Linear dispersion * (@ 435.833 nm)	4.17 nm/mm	2.38 nm/mm	1.52 nm/mm	1.03 nm/mm
CCD resolution ** (20 µm pixel, 20 µm slit width)	0.4 nm	0.14 nm	0.09 nm	0.06 nm
PMT resolution * (10 µm slit width)	0.4 nm	0.1 nm	0.05 nm	0.03 nm
Wavelength coverage (across 26.8 mm CCD)	111 nm	64 nm	41 nm	27 nm
Grating size	32 x 32 mm	68 x 68 mm 68 x 84 (optional)	68 x 68 mm 68 x 84 (optional)	68 x 68 mm
Grating mount	Interchangeable dual grating turret	Interchangeable triple grating turret	Interchangeable triple grating turret	Interchangeable triple grating turret
Focal plane size (front exit port)	25 mm wide x 10 mm high	27 mm wide x 14 mm high	27 mm wide x 14 mm high	25 mm wide x 14mm high
Astigmatism (at focal plane edges)	690 µm	720 µm	250 - 300 µm	150 - 175 µm
Standard Series manual slits (micrometer adjustable)	10 µm to 3mm manual	10 µm to 3mm manual	10 µm to 3mm manual	10 µm to 3mm manual
Wavelength accuracy	± 0.25 nm	± 0.2 nm	± 0.2 nm	± 0.1 nm
Repeatability	± 0.05 nm	± 0.05 nm	± 0.05 nm	± 0.05 nm
Drive step size	0.005 nm	0.005 nm	0.005 nm	0.005 nm
Size	7 in (178 mm) long 7 in (178 mm) wide 6.5 in (165 mm) high	13.2 in (337 mm) long 10 in (254 mm) wide 8 in (203 mm) high	21 in (534 mm) long 11 in (280 mm) wide 8 in (203 mm) high	30 in (762 mm) long 11 in (280 mm) wide 8 in (203 mm) high
Optical axis height	4 in (102 mm)	4.875 in (124 mm)	4.875 in (124 mm)	4.875 in (124 mm)
Weight	10 lbs (4.5 kg)	35 lbs (15.9 kg)	40 lbs (18 kg)	45 lbs (20.5 kg)
Computer interface	USB and RS232	USB and RS232	USB and RS232	USB and RS232

* Linear dispersion measured with a 1200 g/mm grating @ 435.8 nm.
PMT resolution measured with a 1200 g/mm grating @ 435.8 nm,10 µm slit width and 4 mm slit height.
** CCD resolution measured with a 1200 g/mm grating @ 435.8 nm, 20 µm slit width and 20 µm pixel.

SYDOR INSTRUMENTS, LLC

Product Specifications

ROSS 2000 Streak Camera

The ROSS 2000 Streak Camera is Sydor Instruments' versatile large format photocathode streak camera system. The architecture of the ROSS 2000 is modular allowing users to change modules to meet changing experimental requirements. When coupled to a spectrograph it is ideally suited for recording spectroscopic data of time-resolved experiments. Examples include time-resolved absorption emission spectroscopy of atomic shock emissions as well as detontics. All ROSS Streak Cameras come bundled with Sydor's ROSS Remote Application and Analysis Software which provides full control of streak camera, acquisition and display of streak image, image processing, file storage and file exportation.

ROSS 2000 BASE MODULE	KEY PERFORMANCE PARAMETERS
Temporal Resolution	36 ps
Photocathode Dimensions	20 mm
Photocathode Type	S20 (additional photocathode options available)
Input Window	Fused Silica
Screen Phosphor	P43
Spatial Magnification	0.7 – 1.5
Image Intensifier	Single stage 25 mm MCP, 1 - 1000 Adjustable Gain
Gating (MCP)	Extinction Ratio >10^6, 3 ns FWHM @ 200 kHz
Gating (Photocathode)	Extinction Ratio >10^4; Delay <100ns, Rise Tim: <10ns, Fall Time 30ns
Shutter	35 mm Electro Mechanical
Interface	Ethernet 10/100 BaseT
Software	ROSS Streak Camera Control and Analysis Software
Power	120/240 VAC 50-60 Hz

Specifications subject to change

The ROSS 2000 utilizes an achromatic all reflective Offner relay imaging system to support the user's direct imaging needs. Based upon the user's experimental needs, the ROSS 2000 can be directly coupled to a spectrometer.

INPUT OPTICS	KEY PERFORMANCE PARAMETERS
UV/VIS/IR Input Optics	Aluminum w. MgF_2 broadband coating
	250 nm – 1150 nm, F/4.0, 1:1 Magnification
	Continuously variable slit width 50µm to 1mm
	35 mm field of view
Spectrograph	150 or 300 mm Focal Length, Multiple Grating Turret, Fiber Input Custom spectrometer integration available

Specifications subject to change

FOR MORE INFORMATION PLEASE CONTACT US AT: (585) 278-1168
291 MILLSTEAD WAY · ROCHESTER · NEW YORK · 14624 · SYDOR INSTRUMENTS.COM · INFO@SYDORINSTRUMENTS.COM

The **Triggered Sweep Module** provides for up to 12 sweep speeds ranging from 500 picoseconds to one millisecond. This enables users to configure their system with the speeds most appropriate for their experimental needs within one module. Additional sweep module can be purchased to accommodate multiple users in more dynamic environments. Sweep modules can be easily swapped out by the user.

TRIGGERED SWEEP MODULE	KEY PERFORMANCE PARAMETERS
Temporal Resolution	<36 ps Single Shot (Tube Limited)
Sweep Window	500 ps – 1 ms (extended range on request
Sweep Speeds	12 user selectable speeds
Trigger Jitter	<25 ps
Sweep Repetition Frequency	10 Hz
Monitor Out	TTL
Trigger Input Signal	±5 V 50Ω

Specifications subject to change

The ROSS 2000 supports several **Recording Systems** allowing the user to select the best configuration for their research and experimental needs. Each comes with the output optics and mechanical structure for coupling the recording system to the Base Module.

RECORDING SYSTEMS	KEY PERFORMANCE PARAMETERS
Standard Camera	1360 x 1040 Resolution Interline CCD
	Lens Coupled
	12 bit A/D
	10 e- Read Noise
	30 frames per second max
	IEEE 802.3 1000baseT interface
High Resolution Camera	2452 x 2056 Resolution Interline CCD
	Lens Coupled
	14 bit A/D
	5 e- Read Noise
	9 frames per second max
	IEEE 802.3 1000baseT interface
Cooled Camera	1392 x 1040 Resolution Interline CCD
	Lens Coupled
	16/14 bit A/D
	TE cooling to -55°C with fan
	11.6 frames per second max
	USB 2.0 PC interface

Specifications subject to change

FOR MORE INFORMATION PLEASE CONTACT US AT: (585) 278-1168
291 MILLSTEAD WAY · ROCHESTER · NEW YORK · 14624 · SYDOR INSTRUMENTS.COM · INFO@SYDORINSTRUMENTS.COM

Accessories / Options

ACCESSORIES	PERFORMANCE FEATURE
CCD Trigger Combiner Box	Enables External CCD Trigger
Serial to Fiber Adapter	Optical Isolation of camera controls
Optical Trigger Module	Optical to electrical trigger
SRS DG645	Digital Delay / Pulse Generator / Gate Trigger
CFD Trigger Module	Constant Fraction Discriminator reduces jitter in variable amplitude triggers
Passive Delay Generator	Jitter free, drift free, adjustable, high-bandwidth signal delay
Liquid Chiller	Air-cooled liquid thermoelectric chiller w/ PID temperature controller
PC and Monitor	Tower w/ Flat Screen -or- Laptop
Multi-channel Fiber Input	20 total fiber input channels
Fiberized Laser Pulser	DC to 10MHz, 665 nm
Fiberized Laser Pulse Generator	Fiber coupled 40 ps, 650 nm laser pulse, DC to 300 kHz rep rate
2 GHz Comb Generator	2 GHz, 500 MHz Timing Reference
Spectrometer Interface Module	Light tight coupling between ROSS 2000 and spectrometer for ease of alignment, with fine focus adjustment

Specifications subject to change

Optional products & services offered:

- Instrument & accessory storage cases
- Service, installation, & technical support
- Extended warranty programs
- Analytical software packages and development
- Accessories for interfacing with other instrumentation
- Electrical and fiber optic cables made to your specifications

FOR MORE INFORMATION PLEASE CONTACT US AT: (585) 278-1168
291 MILLSTEAD WAY · ROCHESTER · NEW YORK · 14624 · SYDOR INSTRUMENTS.COM · INFO@SYDORINSTRUMENTS.COM

APPENDIX D: BACKGROUND ORIENTED SCHLIEREN CODE

Main Routine

```
% Background Oriented Schlieren
% By Catriona White
% email: white444@purdue.edu
% In cooperation with Purdue University, Zucrow Labs, and Sandia National
Labs
% Created: March 21st 2020
% Updated: May 21th 2020
%
% References: JoshTheEngineer, OpenPIV-bos, Cozzi(2017), (Cite these better)
%
%
% Description: This code takes in two schlieren images, one background
%              and one of an event. It compares the images to determine
%              how the pixels shift, in order to calculate the density
%
% Required Inputs: Background Image, Event Image, cm per pixel, distance
%                  between event and background, fluid medium, preferred
%                  image segmentation size
%
% Provided Outputs: Velocity Plot, Displacement Plot, Density plot
%
% Assumptions: Gladstone-Dale assumptions hold

clear
clc

fprintf('Welcome! Please see readme for code details and running process!\n')

%% General Setup

addpath('Analysis Functions');

%% Background Image Processing

fprintf('\nSelect Background Image\n\n')
[base_name, base_path, c] = uigetfile({'*.jpg; *.png; *.tif; *.tiff',...
    'Image Files (*.jpg; *.png; *.tif; *.tiff)'});

% Read Background image
B_img = imread([base_path base_name]);
B = B_img(:, :, 1);

%% Main Image Processing

fprintf('Select Schlieren Image to be Analyzed\n\n')
```

```
[img_name, img_path, c] = uigetfile({'*.jpg; *.png; *.tif; *.tiff',...
    'Image Files (*.jpg; *.png; *.tif; *.tiff)'});

% Read Background image
M_img = imread([img_path img_name]);
M = M_img(:, :, 1);

%% Take Inputs

% Ideal Image Segmentation Size
P_L = input('Please input ideal segmentation size (recommeded starting value
12): ');
fprintf('\n')
P_L_half = round(P_L/2);

% Pixels per cm based on image size
Im_size = input('Please input cm/pixel of images: ');
fprintf('\n')

% Maximum pixel shift
fprintf('Any extreme changes in density may not be due to density variation
\n');
fprintf('but rather something solid between the background in the event.
\n');
fprintf('The maximum shift filters out any extreme changes due to external
factors.\n');
fprintf('Recommended starting value of 7, although this may not apply to all
cases.\n\n');
max_shift = input('Please input the maximum desired pixel shift: ');
fprintf('\n\n')

%% Prepare for Combined Image Processing

% Determine centers for analysis
R_L = (P_L: P_L: (size(M, 1) - P_L_half))';
C_L = (P_L: P_L: (size(M, 2) - P_L_half))';

% Create grid of X and Y analysis locations
[R_grid, C_grid] = meshgrid(R_L, C_L);
X_q = C_grid'.*Im_size;
Y_q = R_grid'.*Im_size;
X_disp = (X_q - min(min(X_q)));
Y_disp = (Y_q - min(min(Y_q)));

%% Compare both images to determine pixel offset

% Loop parameter setup
Iteration_number = 0;
Internal_count = 0;
i = 1;
j = 1;

% Array Preallocation
X_peak(1:R_L, 1:C_L) = 0;
Y_peak(1:R_L, 1:C_L) = 0;
```

```
X_change(1:R_L, 1:C_L) = 0;
Y_change(1:R_L, 1:C_L) = 0;

% Loop to compare images
while i < length(R_L) + 1

    % Determine what row this is for diagnostic purposes
    Iteration_number = Iteration_number + 1;
    % Report Loop progress
    fprintf('Run number %.0f\n', Iteration_number)
    % Reset Column Count
    Internal_count = 0;

    while j < length(C_L)+1
        % Record which column this is for diagnostic purposes
        Internal_count = Internal_count + 1;

        % Truncate images
        B_trunc = [C_L(j) - P_L_half, R_L(i) - P_L_half, P_L, P_L];
        M_trunc = [C_L(j) - P_L, R_L(i) - P_L, 3*P_L, 3*P_L];
        % Crop Images
        B_cropped = imcrop(B, B_trunc);
        M_cropped = imcrop(M, M_trunc);

        % Check if truncated image sections are the same
        if all(B_cropped == B_cropped(1, 1))
            %Do nothing
            X_peak(i,j) = 0;
            X_change(i,j) = 0;
            Y_peak(i,j) = 0;
            Y_change(i,j) = 0;

        % If the truncated image sections are different:
        else
            % Compute the normalized cross-correlation of the image sections
            [CC_mat, peak_row, peak_col, CC_row, CC_col]=
img_cross_correlate(B_cropped, M_cropped);

            % Run corrective three point Gaussian
            [x_correction, y_correction] = Gaussian_correction(CC_mat,
peak_row, peak_col, CC_row, CC_col);

            % Find peak relative to X axis
            X_peak(i,j) = real(peak_col + y_correction);
            % Find X axis shift
            X_change(i,j) = X_peak(i,j) - P_L_half - P_L - 1;
            % Find peak relative to Y axis
            Y_peak(i,j) = real(peak_row + x_correction);
            % Find Y axis shift
            Y_change(i,j) = Y_peak(i,j) - P_L_half - P_L - 1;
        end
        j = j + 1;
    end
    j = 1;
    i = i + 1;
```

```
end

% Record X displacement relative to X pixel location
U_disp = X_change;
U_disp(1,:) = U_disp(2,:);
U_disp(:,1) = U_disp(:,2);
U_disp(end,:) = U_disp(end-1,:);
U_disp(:,end) = U_disp(:,end-1);
U_raw = U_disp;

% Record Y displacement relative to Y pixel location
V_disp = Y_change;
V_disp(1,:) = V_disp(2,:);
V_disp(:,1) = V_disp(:,2);
V_disp(end,:) = V_disp(end-1,:);
V_disp(:,end) = V_disp(:,end-1);
V_raw = V_disp;

% Record total displacment relative to grid
Tot_disp = sqrt(U_disp.^2 + V_disp.^2);
raw_tot = sqrt(U_disp.^2 + V_disp.^2);

% Make sure the same pixels are being analyzed
% Kind of sketch but it works
U_size = size(U_disp);

U_disp(abs(U_disp) > max_shift) = nan;
V_disp(abs(V_disp) > max_shift) = nan;
Tot_disp(abs(Tot_disp) > max_shift) = nan;

fprintf('\n\nImage Analysis Complete\n')
fprintf('Entering Post Processing\n\n')

%% Pixel Movement Plot
% Show where each pixel appeared to move

figure(1)
hold on
% Show analyzed zones
plot(X_q, Y_q, 'k.')
% Show Change
quiver(X_q, Y_q, flip(U_disp), flip(V_disp), 'Color', 'b', 'Linewidth', 3)
title('Change in Pixel Location')
xlabel('X Location [cm]')
ylabel('Y Location [cm]')
axis('equal')

% Display how each pixel moved with a colormap
figure(2)
hold on
surf(X_disp, Y_disp, Tot_disp, 'EdgeColor', 'none')
colormap('winter')
% If needed - 'winter' is also a solid colormap
colorbar
title('Density Gradient Estimation')
```

```
xlabel('X Location [cm]')
ylabel('Y Location [cm]')
caxis([min(min(Tot_disp)) max(max(Tot_disp))])
axis('equal')

fprintf('\nAnalysis Completed\n')
```

Gaussian Correction Subfunction

```
function [dx, dy] = Gaussian_correction(mat, r, c, row_max, col_max)

if (r == 1)
    r = r + 1;
end
if (r == row_max)
    r = r - 1;
end
if (c == 1)
    c = c + 1;
end
if (c == col_max)
    c = c - 1;
end

% X correction factor
numX = log(mat(r - 1, c)) - log(mat(r + 1, c));
denX = 2*log(mat(r - 1, c)) - 4*log(mat(r, c)) + 2*log(mat(r + 1, c));
dx   = numX/denX;

% Y correction factor
numY = log(mat(r, c - 1)) - log(mat(r, c + 1));
denY = 2*log(mat(r, c - 1)) - 4*log(mat(r, c)) + 2*log(mat(r, c + 1));
dy   = numY/denY;
```

Image Cross Correlation Subfunction

```
function [mat, row, col, mat_row, mat_col] = img_cross_correlate(img1, img_2)

mat = normxcorr2(img1, img_2);

% Check cross-correlation matrix size
[mat_row, mat_col] = size(mat);

% Find the peak indices of the cross-correlation map
[r_peak, col_peak] = find(mat == max(mat(:)));

% Record max peak values
row = max(r_peak);
col = max(col_peak);
```

REFERENCES

1. Gaydon, A. G., and Hurle, I. R. (1963). The shock tube in high-temperature chemical physics. Chapman & Hall, NY: London.
2. Meier, G. E. (1998). New optical tools for fluid mechanics. Sadhana, 23(5-6), 557-567.
3. Richard, H., and Raffel, M. (2001). Principle and applications of background oriented schlieren (BOS) method. Measurement Science and Technology, 12(9), 1576-1585.
4. Tranter, R. S., Brezinsky, K., and Fulle, D. (2001). Design of a high-pressure single pulse shock tube for chemical kinetic investigations. Review of Scientific Instruments, 72(7), 3046–3054.
5. Sommersel, O. K., Bjerketvedt, D., Christensen, S. O., Krest, O., and Vaagsaether, K. (2008). Application of background oriented schlieren for quantitative measurements of shock waves from explosions. Shock Waves, 18(4), 291-297.
6. Verso, L., and Liberzon, A. (2015). "Background Oriented Schlieren in a Density Stratifield Fluid." Rev. Sci. Instrum. 86, 103705.
7. Richard, H., Raffel, M., Rein, M., Kompenhans, J., and Meier, G. E. (2002). Demonstration of the applicability of a background oriented schlieren (BOS) method. Laser techniques for fluid mechanics, 145-156.
8. Santos, L., and Stryczniewicz, W. (2018). Application of Background Oriented Schlieren for quantitative measurement of transonic flows. Journal of Physics: Conference Series, 1101, 012030.
9. Nicolas, F., Todoroff, V., Plyer, A., Besnerais, G. L., Donjat, D., Micheli, F., and Sant, Y. L. (2015). A direct approach for instantaneous 3D density field reconstruction from background-oriented schlieren (BOS) measurements. Experiments in Fluids, 57(1).
10. Cozzi, F., Göttlich, E., Angelucci, L., Dossena, V., and Guardone, A. (2017). Development of a background- oriented schlieren technique with telecentric lenses for supersonic flow. Journal of Physics: Conference Series, 778, 012006.
11. Fiala, T., and Sattelmayer, T. (2013). 5th European conference for aeronautics and space sciences (EUCASS) DOI: 10.13140/2.1.1852.0966

12. Orth, M., Orth, R., Gabl, J., Satija, A., Hayashi, J., Akamatsu, F., Lucht, R., and Pourpoint, T. (2018). Time Resolved Flame Temperature Measurements Using a Streak Camera Spectrometer. Western States Section of the Combustion Institute – Spring 2018 Meeting.
13. Satija, A., Ruesch, M., Powell, M., Son, S., Lucht, R. (2018). Optics Letters 43 (3), 443-446
14. Luque, J., Smith, G., Jeffries, J., and Crosley, D. (2001). 39th Aerospace Sciences Meeting and Exhibit AIAA 2001-0626.
15. (2008). Hamamatsu, Guide to Streak Cameras, Hamamatsu Photonics K.K. Systems Division.
16. Black, A. (2017). Liquid and Gas Phase Chemistry of Hypergolic Reactions Between MMH and NTO or RFNA.
17. Kurucz, R. & Bell, B. 1995, Atomic Line Data (R.L. Kurucz and B. Bell) Kurucz CD-ROM No. 23. Cambridge, Mass.: Smithsonian Astrophysical Observatory
18. Spalding, M., Krier, H., & Burton, R. (2000). Boron Suboxides Measured During Ignition and Combustion of Boron in Shocked Ar/F/O2 and Ar/N2/O2 Mixtures. Journal of Combustion and Flame. Volume 120. Issue number 1-2. Pages 200-210.
19. Ao, W., Wang, Y, & Yang, W. (2014). Ignition, combustion, and oxidation of mixtures of amorphous and crystalline boron powders. Combustion Explosions and Shock Waves.

PUBLICATION

1. White, C., Orth, M., Gabl, G., and Pouropint, T. (2020). High Speed Shock Tube Diagnostics using Background Oriented Schlieren. AIAA Propulsion and Energy Forum 2020.